COMBUSTION BEHAVIOUR OF MULTICOMPONENT POOL FIRES

by

Aaron Yip

Submitted in partial fulfillment of the requirements
for the degree of Master of Applied Science

at

Dalhousie University
Halifax, Nova Scotia
March 2020

Dedicated to Dad, Mom, and Brian

Table of Contents

List of Tables

List of Figures

Abstract

This work examined combustion behaviour in multicomponent pool fires through experimentation and application of empirical, global energy balance, and computational fluid dynamics (CFD) modelling approaches. Transient pool fire experiments were conducted to measure the rate of distillation in ethanol-water mixtures. The pool composition over time was predicted adequately by a batch distillation model. Steady-state pool fire experiments were conducted to evaluate the effects of mixture ratios on maximum burning rate, flame height, and flame temperature in ethanol-water, ethanol-isopropanol, and ethanol-hexane mixtures. Combustion behaviour in these fires was strongly dependent on the vapour phase composition of the fuel. Standard correlations for estimating flame heights and temperatures showed good agreement with the experiments. The open-source CFD package Fire Dynamics Simulator (FDS) was modified to enable pyrolysis modelling for multicomponent fuels. With the new modifications, FDS was able to reproduce combustion behaviours observed in transient ethanol-heptane pool fire experiments conducted by other researchers.

List of Abbreviations and Symbols Used

Abbreviations

CFD	Computational fluid dynamics
EDC	Eddy Dissipation Concept
EG	Ethanol-gasoline
FDS	Fire Dynamics Simulator
HRR	Heat release rate
ID	Inner diameter
LES	Large eddy simulation
PMMA	Polymethyl methacrylate
VLE	Ethanol-diesel
VLE	Vapour-liquid equilibrium

Greek Letters

α	Relative volatility	–
χ_a	Combustion efficiency	–
χ_r	Radiative fraction	–
Δ	LES filter width	m
γ	Activity coefficient	–
κ	Absorption coefficient	m^{-1}
λ	Blowing factor	–

μ	Dynamic viscosity	$\mathrm{Pa\,s}$
ν	Stoichiometric coefficient	–
ω	Vorticity	$\mathrm{s^{-1}}$
Φ	Dimensionless parameter used by Yokoi	–
ρ	Density	$\mathrm{kg\,m^{-3}}$
ρ	Reflectivity	–
σ	Stefan-Boltzmann constant	$\mathrm{W\,m^{-2}\,K^{-4}}$
τ	Viscous stress tensor	Pa
τ_{chem}	Chemical mixing time scale	s
τ_d	Diffusion mixing time scale	s
τ_{flame}	Limiting time scale based on flame height	s
τ_g	Buoyant acceleration time scale	s
τ_{mix}	Mixing time scale	s
τ_u	Advective time scale	s
ε	Emissivity	–

Latin Letters

$\bar{P}$	Background pressure	Pa
ΔH_c	Heat of combustion	$\mathrm{J\,kg^{-1}}$
ΔH_g	Heat of gasification	$\mathrm{J\,kg^{-1}}$
ΔH_v	Heat of vaporization	$\mathrm{J\,kg^{-1}}$
$\dot{\mathbf{Q}}''$	Sum of conductive, diffusive, and radiative heat fluxes	$\mathrm{W\,m^{-2}}$

$\dot{m}$	Mass burning rate	$\mathrm{kg\,s^{-1}}$
$\dot{m}''$	Mass flux	$\mathrm{kg\,m^{-2}\,s^{-1}}$
$\dot{m}'''$	Volumetric mass generation rate	$\mathrm{kg\,m^{-3}\,s^{-1}}$
$\dot{m}''_\infty$	Mass flux for an infinite diameter pool fire	$\mathrm{kg\,m^{-2}\,s^{-1}}$
$\dot{Q}$	Heat release rate	W
$\dot{Q}''$	Heat flux	$\mathrm{W\,m^{-2}}$
$\dot{Q}'''$	Volumetric heat generation	$\mathrm{W\,m^{-3}}$
$\dot{Q}^*$	Dimensionless heat release rate	–
$\hat{n}$	Molar flow rate per unit mass of fuel	$\mathrm{mol\,kg^{-1}}$
$\mathbf{S}$	Direction vector	–
$\mathbf{u}$	Velocity vector	$\mathrm{m\,s^{-1}}$
$\mathbf{x}$	Location vector	m
$\tilde{P}$	Perturbation pressure	Pa
A	Surface area	$\mathrm{m^2}$
$A_{i\beta}$	Pre-exponential factor	$\mathrm{s^{-1}}$
B	Spalding B number	–
C_1	Dimensionless effective soot parameter	–
C_2	Planck's second constant	$\mathrm{m\,K}$
c_p	Specific heat capacity	$\mathrm{J\,kg^{-1}\,K^{-1}}$
D	Diameter	m
D_g	Gas diffusion coefficient	$\mathrm{m^2\,s^{-1}}$

$E_{i\beta}$	Activation energy	$\mathrm{J\,mol^{-1}}$
f_v	Soot volume fraction	–
g	Gravitational acceleration	$\mathrm{m\,s^{-2}}$
Gr	Grashof number	–
H	Mean flame height	m
h	Convective heat transfer coefficient	$\mathrm{W\,m^{-2}\,K^{-1}}$
h_m	Convective mass transfer coefficient	$\mathrm{m\,s^{-1}}$
H_p	Hydrodynamic head	$\mathrm{m^2\,s^{-2}}$
H_r	Heat of reaction	$\mathrm{J\,m^{-3}}$
h_s	Specific enthalpy	$\mathrm{J\,kg^{-1}}$
I	Radiative intensity	$\mathrm{W\,sr^{-1}}$
k	Thermal conductivity	$\mathrm{W\,m^{-1}\,K^{-1}}$
$k\beta$	Empirical constant in Eq. (2.3)	$\mathrm{s^{-1}}$
k_{sgs}	Sub-grid scale kinetic energy	$\mathrm{m^2\,s^{-2}}$
L	Characteristic dimension	m
L	Path length	m
L_m	Mean beam length	m
m	Mass	kg
N	Number of species in the fuel	–
n	Infrared averaged soot optical constant	–
N_r	Number of reactions	–

$n_{i\beta}$	Reaction order	–
Nu	Nusselt number	–
P	Pressure	Pa
p	Partial pressure	Pa
Pr	Prandtl number	–
R	Radius	m
r	Stoichiometric air to fuel mass ratio	–
r_β	Rate of reaction β	$\mathrm{s^{-1}}$
R_g	Universal gas constant	$\mathrm{J\,mol^{-1}\,K^{-1}}$
Ra	Rayleigh number	–
Re	Reynolds number	–
S	Normalized mass generation rate from miscellaneous reactions	$\mathrm{s^{-1}}$
s	Infrared averaged soot optical constant	–
Sh	Sherwood number	–
T	Temperature	K
t	Time	s
U	Integrated radiative intensity	$\mathrm{W\,m^{-2}}$
V	Volume	$\mathrm{m^3}$
v	Surface regression rate	$\mathrm{m\,s^{-1}}$
W	Molecular weight	$\mathrm{kg\,mol^{-1}}$
X	Liquid phase mole fraction	–

x	Length in x-direction	m
x	Liquid phase mass fraction	–
Y	Vapour phase mole fraction	–
y	Vapour phase mass fraction	–
Y_s	Soot yield	–
$y_{f,\infty}$	Fuel vapour mass fraction in the bulk phase	–
$y_{f,s}$	Fuel vapour mass fraction in the first cell above pool surface	–
Z	Mixture fraction	–
z	Height	m
z_0	Virtual origin	m

Subscripts

β	Reaction β
∞	Ambient
a	Air
b	Bubble-point
c	Convection
$cell$	Computational cell
$cond$	Conduction
f	Flame
$feed$	Fuel fed to a pool fire
g	Gas

i	Species i in fuel
inc	Incident
j	Species j in reactants or products
l	Liquid
max	Maximum
net	Net quantity
$products$	Species remaining after combustion
r	Radiation
$reactants$	Reacting species in the flame
ref	Reference condition
rr	Re-radiation
s	Surface
sgs	Sub-grid scale
TC	Thermocouple
thr	Threshold
0	Initial

Acknowledgements

I am very grateful to all the people who helped me through my Master's journey. First and foremost, I want to thank my parents and brother for always supporting and believing in me. Their love has shaped me into the man I am today. I want to thank my supervisors Jan Haelssig and Michael Pegg for their guidance through both my B.Eng and this project. Jan's insights on physical modelling and experience with computational fluid dynamics software were invaluable for developing and validating the fire models. Mike's wisdom on experimental practices and many years of supervisory experience were important for guiding the overall direction of the project. I am grateful for Scott Mackinnon's help with using LabVIEW, fixing electronics, and transporting equipment and chemicals. Dean Grijm is acknowledged for assisting in constructing the experimental apparatus. Julie O'Grady's help with ordering materials and equipment and Paula Colicchio's help with coursework administration is greatly appreciated. I thank the Royal Canadian Navy's Damage Control School in Herring Cove, Nova Scotia, for accommodating the final sets of pool fire experiments and enabling me to complete the project in a safe space. Financial support from Killam Laureates and the Natural Sciences and Engineering Research Council (NSERC) is gratefully acknowledged.

Chapter 1

Introduction

Most transportation fuels and chemicals used in the chemical processing industry are flammable. With widespread transportation, storage, and manufacture of these flammable liquids comes the risk of a potential release and ignition of the fuel. This scenario is known as a pool fire, which is a class of fire that burns over a vaporizing fuel sourced by a stationary fuel body. The term can be more generally applied to any buoyant diffusion flame burning over a horizontal surface (Hamins, Kashiwagi, & Buch, 1996), meaning that the fuel can also be in gaseous and solid form. An example of a pool fire is shown in Figure 1.1.

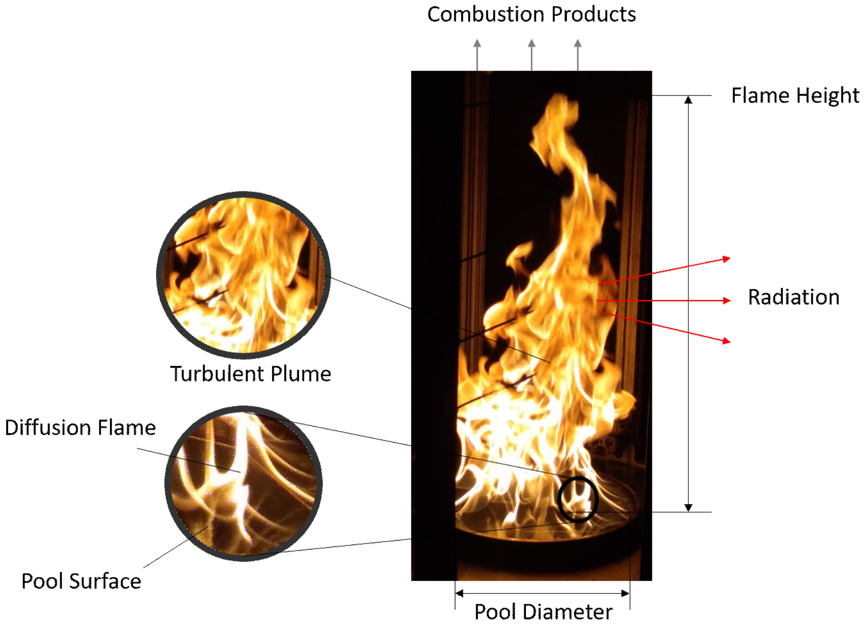

Figure 1.1: Liquid pool fire with labelled properties and components.

Pool fires are a problem of practical interest because they are the most common incident in the chemical processing industry that often lead to subsequent accidents (Vipin, Pandey, Tauseef, Abbasi, & Abbasi, 2018). Additionally, there are only two prerequisites for a pool fire to occur: release of fuel in an open atmosphere, and ignition. A notable pool fire incident in Canada was the derailment of a 72 car train carrying petroleum crude oil in Lac-Mégantic, Quebec, on July 6, 2013 (Johnston, 2013). Some of the oil was released and ignited, which resulted in a large pool fire that burned in the town for two days.

In addition to being a common incident in industry, pool fires are also common in domestic instances. They occur frequently in fires associated with cooking equipment, which made up 33% of residential fires in Canada in 2014 (Statistics Canada, 2017). Cooking oils are cited as a common ignition source for kitchen fires, which were responsible for 66% of kitchen fires in one and two family homes and 75% of fires in appartments in the province of Alberta, Canada (Wijayasinghe & Makey, 1997). The National Fire Protection Association also cites that 52% of cooking fires in the United States were caused by ignition of cooking oils, fats, and grease between 2013 and 2017 (Ahrens, 2019).

There are many hazards associated with a pool fire, such as the liquid pool spreading, fire spread to flammable surfaces, build-up of combustion products and flammable vapours inside a compartment. A major hazard associated with large pool fires is the thermal radiation given off to the surroundings. By knowing the radiative heat flux emitted from a fire, it is possible to estimate the degree of damages that will occur to nearby equipment, structures, and personnel (Assael & Kakosimos, 2010). Thus, an estimate of the thermal radiation emitted is generally required for consequence analysis involving large pool fire scenarios (Cozzani, Gubinelli, Antonioni, Spadoni, & Zanelli, 2005; Pula, Khan, Veitch, & Amyotte, 2005; da Cunha, 2016; Zhao et al., 2017). To estimate the thermal radiation emission rate, the size and shape of the flame, as well as total heat release rate (HRR) are required (Mudan, 1987). These quantities have been thoroughly investigated for common flammable liquids. A comprehensive review on the characteristics of pool fire flames is given by Joulain (1998).

HRR is an important parameter for hazard assessment of pool fires because it can be used to estimate the size of the fire (Heskestad, 1983). A typical HRR curve for a pool fire burning a pure fuel is characterized by a growth, steady-state, and decay period (Chatris et al., 2001). A simplified HRR curve describing this behaviour shown in Figure 1.2. For design or consequence analysis calculations, the area of interest is the steady-state period because it quantifies the maximum power output of the fire. This idealization of a pool fire is convenient and applicable to situations where simple, well-studied fuels are burned.

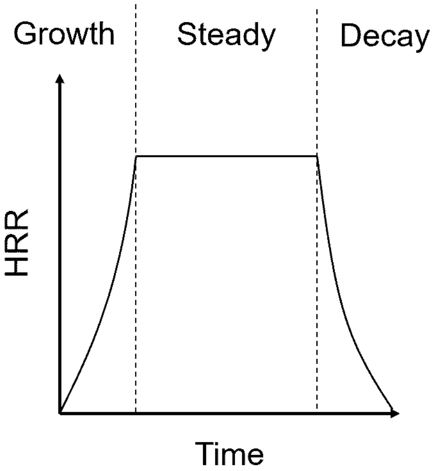

Figure 1.2: Typical HRR curve for a single-component pool fire.

In practice, flammable liquids generally do not consist of a single compound. For example, many starting materials in chemical processes are typically mixtures that need to be separated into their individual components (*e.g.* crude oil refining, distilling bio-ethanol, ether synthesis). Refined transportation fuels like gasoline, diesel, and kerosene are also composed of multiple components, like alkanes, cycloalkanes, and aromatics. Fuels may also be purposely blended to obtain more desirable combustion properties. A common example is the use of ethanol and diesel blends (E-diesel) in vehicles to reduce pollutant emissions. Another example is the use of organic peroxide and hydrocarbon blends as alternative fuels for industrial combustion processes (Mishra & Wehrstedt, 2015).

Fuel blends exhibit different combustion behaviour from pure fuels due to the difference in volatility between compounds, which causes the fuel to take on flammability and combustion properties that are similar to the more volatile compounds (Eddings, Yan, Ciro, & Sarofim, 2005; Waterland, Venkatesh, & Unnasch, 2003). Properties of common transportation fuels and their blends are summarized in Table 1.1 for comparison. In ethanol-diesel (ED) blends, presence of 10-15% ethanol is enough to make the flash point and flammability limits approximately the same as pure ethanol, which increases the risk of ignition. Meanwhile, the flammability properties of ethanol-gasoline (EG) blends are some kind of average of the pure fuel properties.

Table 1.1: Flammability Properties of E-diesel, E-gasoline, and Other Transportation Fuels. Adapted from Waterland et al. (2003) and Dillon et al. (2009)

Property	Diesel	Ethanol	Gasoline	ED 15-85%	EG 85-15%
Lower Flammability Limit (%vol)	0.6	3.3	1.4	3.3	1.1-1.4
Upper Flammability Limit (%vol)	5.6	19	7.6	19	19.0
Flash Point (°C)	64	13	-43	13	-20 to -4
Autoignition Temperature (°C)	230	366	300	230	257
Heat of Combustion ($\mathrm{MJ\,kg^{-1}}$)	46.5	29.8	46.7	44.2	27.9-29.4
Heat of Vaporization ($\mathrm{kJ\,kg^{-1}}$)	270	840	350	350	757-772

Volatility differences between compounds causes selective evaporation of more volatile compounds, meaning the fuel undergoes distillation as the fire progresses (Ditch et al., 2013; Eddings et al., 2005). Furthermore, depending on the type of fuel mixture, the radiative intensity of the fire may also be modified by lower soot emissions (Esarte, Millera, Bilbao, & Alzueta, 2009; Kinoshita & Lee, 1994) or additional chemical reactions (Mishra & Wehrstedt, 2015). Due to distillation in the pool, the thermodynamic and chemical properties of the fuel become transient, so the assumption of a constant peak HRR may be inaccurate for certain fuel mixtures.

The objective of this study was to improve predictability of fire dynamics in a multicomponent pool fire scenario. This involved developing a method for predicting distillation in the pool and validating established empirical models for mass burning rate, flame temperature, and flame height against data collected from lab-scale pool fire experiments. Additionally, the capabilities of computational fluid dynamics (CFD) software were expanded to simulate transient multicomponent pool fire scenarios and validated against data from literature.

In Chapter 2, a literature review on multicomponent combustion, multicomponent pool fires, and fire modelling is presented to identify current practices and gaps in understanding of each topic. Chapter 3 describes the methodology followed to select a representative range of fuel mixtures and explains the experimental methods employed. Chapter 4 describes the empirical and energy balance models and evaluates model performance in comparison to experimental results. Chapter 5 outlines the models present in the CFD software Fire Dynamics Simulator (FDS) and includes several case studies to evaluate the capabilities of FDS for modelling multicomponent pool fires. Main conclusions from the results, and recommendations for future work are then summarized in Chapter 6.

Chapter 2

Literature Review

This review serves to summarize available theories on multicomponent fuel combustion, review experimental works investigating combustion behaviour of multicomponent fuel pool fires, and identify current practices for predicting the combustion properties of the fire. Properties of interest are the burning rate ($\dot{m}$), mean flame height (H), and flame temperature (T_f), since these are the main factors governing radiant heat transfer to the surroundings of the fire. Other relevant parameters are the fuel composition during and/or after burning, soot emissions, liquid temperature distribution (T_l), radiant fraction (χ_r), and whether the fire was continuously fed with fresh fuel. A fire that was fed continuously with fuel for the duration of the experiment will be defined as a steady-state or continuous pool fire, while a fire that was not will be defined as a transient or batch pool fire. Table 2.1 provides a broad summary of all the aforementioned quantities of interest for characterizing combustion characteristics of multicomponent fuel pool fires.

The review is divided into sections on burning rate, mean flame height, and flame temperature. A separate section is reserved for current practices in computational fluid dynamics (CFD) modelling of pool fires and any relevant works with multicomponent fuels.

2.1 Theories for Multicomponent Fuel Combustion

The theoretical basis for multicomponent fuel combustion has been examined in the context of single droplet combustion in a quiescent atmosphere. Droplet vaporization is a well-studied topic (Williams, 1973) due to the importance of spray combustion in optimizing internal combustion engine performance and efficiency.

Several works on multicomponent fuel droplet vaporization and combustion have been reviewed by Law (1982). Prakash and Sirignano (1978) showed that in theory, the temperature profile in a droplet is never uniform even if internal circulation is

Table 2.1: Summary of Studies on Combustion Properties in Multicomponent Pool Fires

Author	Fuels	Pan Diameter (m)	Batch/Continuous	$\dot{m}$	H	T_f	T_l	χ_r	Soot	Distillation
Blinov and Khudyakov (1961)	Ethanol/Water Ethanol/Benzene Ethanol/Isoamyl alcohol Ethanol/1-Propanol Ethanol/*n*-butanol	0.0077	B/C	✓	-	-	-	-	-	✓
Grumer et al. (1961)	Mixed amine fuels	1.22	B	✓	✓	-	✓	✓	-	-
Apte (1998)	Ethanol/Water/BP-33	0.445,1	B	✓	✓	-	-	-	✓	-
Eddings et al. (2005)	Jet-A Hex-12	0.30	B/C	✓	-	-	-	-	✓	✓
Ditch et al. (2013)	Methanol/Toluene Ethanol/Toluene *n*-heptane/Toluene JP-8	0.1-2.0	C	✓	-	-	-	-	✓	-
Y. Ding et al. (2014)	Ethanol/*n*-heptane	0.30	B	✓	✓	✓	-	-	-	-
C. Wang et al. (2014)	Ethanol/Gasoline	0.30[a]	B	✓	✓	✓	-	-	-	-
Mishra and Wehrstedt (2015)	Peroxides/Isododecane	0.02-1.0	B	✓	✓	-	-	-	-	-
Y. Ding et al. (2017)	Ethanol/*n*-heptane	0.30	B	✓	✓	✓	✓	-	-	-
Kong et al. (2018)	Crude oil	0.06-0.08[b]	B	✓	-	-	✓	-	-	-
Liu et al. (2018)	Ethanol/1-Propanol	0.30	B	✓	✓	✓	✓	-	-	-
Tian et al. (2018)	Methanol/Gasoline	0.595×0.424	B	✓	✓	✓	-	-	-	-
X. Wang, Zhou, et al. (2018)	Ethanol/*n*-heptane	0.18	B	✓	-	-	✓	✓	-	-
X. Wang, He, et al. (2018)	DGM/Kerosene Ethanol/Kerosene	0.1[a]	B	✓	✓	✓	✓	✓	-	-
Chaudhary et al. (2019)	Diesel/JME	0.6	B	✓	✓	✓	-	✓	-	-
C. Ding et al. (2019)	Lithium ion electrolytes	0.1[a]	B	✓	-	-	✓	✓	-	-
X. Wang, Zhou, et al. (2019)	Ethanol/*n*-heptane *n*-heptane/DMG	0.18	B	✓	✓	✓	✓	✓	-	-
X. Wang, Chen, et al. (2019)	Ethanol/*n*-heptane	0.15	B	-	-	-	✓	-	-	✓
Zhu et al. (2019)	Ethanol/Gasoline	0.20	B	✓	-	✓	✓	-	-	-

[a] Square pan, side length given.

[b] Ice cavity, initial diameter given.

present. Assuming heat and mass transfer behave analogously, this means the species concentration profile will also never be uniform. Law (1982) pointed out that experimental data contradicts this theory, as well-mixed, batch distillation behaviour was observed even with modest amounts of internal circulation. Thus, treatment of the liquid as diffusion-limited or well-mixed define the bounds for the effects of liquid phase mixing on the evaporation process. These scenarios are illustrated in Figure 2.1.

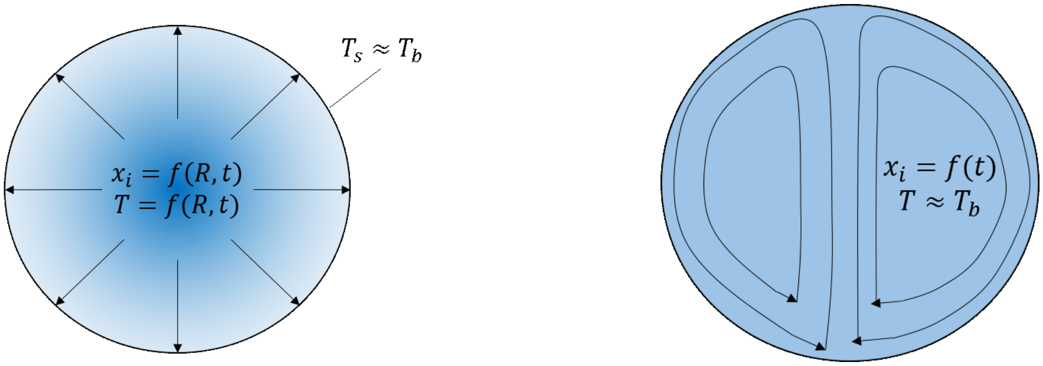

(a) Diffusion-limited (b) Well-mixed

Figure 2.1: Schematics for two limiting cases of liquid phase mixing used in evaporation modelling of multicomponent droplets.

The ideal mixture model (Law, 1976) is an algebraic model for multicomponent droplet combustion that assumes internal circulation is the rate-controlling process of fuel vaporization. The droplet is assumed to have uniform temperature and concentration. The mixture is assumed as ideal, which allows coupling of the liquid and gas phase transport equations through Raoult's law. The composition of the droplet is tracked over the course of burning through a mass balance. The evaporation rate is approximated using the stagnant layer solution of Spalding (1953):

$$\dot{m}'' \approx \ln(1 + B) \tag{2.1}$$

where $\dot{m}''$ is the burning rate per unit area ($\mathrm{kg\,m^{-2}\,s^{-1}}$) and B is the Spalding number, which expresses the ratio of energy released by combustion and energy required to vaporize the fuel per unit mass. A key finding was that the overall evaporation rate was almost independent of the fuel composition in hot atmospheres or during combustion. However, this does not imply that the heat released was constant over time since the composition of the droplet varied over time. If no internal circulation exists in the droplet, then the concentration and temperature profiles are given by the heat conduction and mass diffusion equations (Law, 1978, 1982).

Selection of a particular mixing model determines the composition at the liquid surface, which inevitably affects combustion properties of the vapour. In the well-mixed scenario, the composition will change over time in the same way that a well-mixed, boiling solution would. In the diffusion-limited scenario, a concentration gradient at the surface will form, and the composition of more volatile components near the center of the droplet will remain higher than at the surface (Law, 1982). These mixing models were compared by Bhattacharya, Ghosal, and Som (1996). They found that for mixtures containing species of widely varying volatility, the more volatile components would become fully depleted when using the well-mixed model, while in the diffusion-limited model, more volatile components would persist throughout the lifetime of the droplet. In general, the choice of mixing model would depend on the physical properties of the liquid mixture (*e.g.* viscosity, diffusivity) and the environment it is in (*e.g.* quiescent or turbulent).

2.2 Burning Rate

The mass burning rate of a pool fire characterizes the maximum HRR of the fire based on the following relationship:

$$\dot{Q} = \dot{m}\Delta H_c \tag{2.2}$$

where $\dot{Q}$ is the total HRR (W), $\dot{m}$ is the mass burning rate ($\mathrm{kg\,s^{-1}}$) and ΔH_c is the heat of combustion of the vapour ($\mathrm{J\,kg^{-1}}$). This part of the review covers advances on burning rate mechanisms in multicomponent pool fires and current practices for estimating burning rates in pool fires.

2.2.1 Experimental Works

There have been several studies confirming the occurrence of distillation within multicomponent pool fires. One of the earliest studies investingating distillation in multicomponent pool fires was by Blinov and Khudyakov (1961). Their experiment consisted of burning binary mixtures of ethanol with water, benzene, isoamyl alcohol, propyl alcohol, and *n*-butyl alcohol in a small vertical cylinder, and they measured density of the mixture after a prescribed amount of feed was burned. They observed that for a binary mixture of two combustible components, the liquid becomes enriched in the compound that is least present in the vapour, which is generally the component with the lowest vapour pressure in its pure state. They noted that azeotropic mixtures were an exception to this generality, where the liquid can become enriched in either component depending on how the initial composition compares to the azeotropic point. They also found that oil products like kerosene and sunflower oil followed this trend. Grumer et al. (1961) measured burning rates for mixed amine fuels (MAF-1 and MAF-3), which are primarily composed of components with widely varying volatilities. They observed that the initial and final burning rates approached that of the more and less volatile components, respectively.

Eddings et al. (2005) also confirmed the occurrence of distillation in a 0.30 m diameter jet-A fuel pool fire that was 0.1 m deep. Gas chromatography of the fuel before and after burning showed that the concentration of lighter and heavier hydrocarbons decreased and increased, respectively. An important finding from the study of Eddings et al. (2005) was that the effect of distillation in a multicomponent pool fire could be eliminated by continuously feeding the fire with fresh fuel. During steady-state burning, the bulk concentration was almost identical to the feed, and the top layer showed only a slight concentration increase in heavy components. This is useful because the burning rate of a multi-component fuel can be measured for a specific fuel concentration, which means a direct correlation between the fuel concentration and steady-state fire dynamics can be made. Their observation was only confirmed for jet fuel surrogates that contained only hydrocarbons, so it may not apply to other mixtures with components that have high relative volatilities.

An interesting result from the work of Eddings et al. (2005) is that more volatile components persisted longer in a pool fire than in a batch distillation. After 22%

volume loss in a batch Hex-11 (surrogate for jet fuel) pool fire, the decrease in *n*-octane was only 37% compared to the expected 57% that would have occurred in a batch distillation. The concentration of *n*-cetane was expected to increase by a factor of 6 after 90% volume loss, but it only increased by a factor of 4.3. They attributed these observations to a concentration gradient formed at the surface of the pool fire, where replenishment of lighter compounds to the surface becomes dependent on circulation within the entire pool. Work from Vali, Nobes, and Kostiuk (2015) supports the presence of a concentration gradient due to circulation in the pool. They showed that two distinct liquid regions form in a pool fire. The top layer is well-mixed and uniform in temperature and has a thickness on the order of millimeters, while the bottom layer has a temperature gradient and a small upward velocity to replenish the top layer. Based on the results of Vali et al. (2015), it is very likely that there would have been a lower layer with little mixing in the pool fire of Eddings et al. (2005), which was 0.1 m deep. Reasoning that the pool is divided into a well-mixed and unmixed layer, mixing in a pool fire scenario should fall somewhere between the diffusion limit and a batch distillation.

Y. Ding et al. (2014) observed four different stages of burning for ethanol and *n*-heptane mixtures: initial flame development, azeotropic burning, single-component burning, and decay. They noted that during the azeotropic stage, the burning rate of the blended fuel was actually higher than both the pure fuels. They attributed the higher burning rate to the lower boiling point of the mixture and reduced radiative losses due to lower production of soot. Other studies on azeotropic blends of ethanol and *n*-heptane (Y. Ding et al., 2017; X. Wang, Zhou, et al., 2019) showed that azeotropism can delay occurrence of a ghosting flame. A ghosting flame (Sugawa, Kawagoe, & Oka, 1991) occurs when burning is oxygen-limited (Y. Ding et al., 2017), which may cause unburned fuel vapours to travel up the plume and ignite away from the main fire. Presence of ethanol in the fuel mixture can eliminate the occurrence of ghosting flames by reducing the stoichiometric air-to-fuel ratio of the fuel, which reduces the amount of air required for complete combustion.

Mishra and Wehrstedt (2015) investigated burning rates of peroxide-hydrocarbon blends for pool diameters between 0.01 to 1.0 m. Combustion behaviour in peroxy-fuels differs from hydrocarbons because peroxides release additional heat from thermal decomposition. Furthermore, the O-O group supplies additional oxygen to the combustion reaction. Burning rates also do not scale with diameter the same way as in hydrocarbon pool fires (Mishra & Wehrstedt, 2013, 2015). Their results showed that the correlation between hydrocarbon content and maximum burning rate was nonlinear; a 25% addition of isododecane reduced the burning rate by over 10 times. Peroxide and hydrocarbon blends pose additional challenges to predicting burning rates in pool fires because the reaction kinetics for thermal decomposition must be taken into consideration (Schälike, Chun, Mishra, Wehrstedt, & Schönbucher, 2013).

Liu et al. (2018) measured combustion properties in pool fires burning propanol-water mixtures with various starting concentrations. They developed a linear correlation between the quasi-steady burning rate and initial alcohol mass fraction. The burning rate was lower for fuels with higher water concentrations, which is logical given that water is inflammable and replaces some of the flammable vapours during evaporation. Distillation effects did not appear to have a significant effect on the burning rate over time for lower alcohol concentrations. This can be attributed to little variation in vapour composition with respect to the liquid composition for lower concentrations of propanol.

Tian et al. (2018) demonstrated that distillation in a blended fuel can cause a pool fire to transition between oxygen-limited and fuel-limited burning in tunnels. This conclusion was made by observing that the mean flame heights of pure gasoline and gasoline-methanol blends were approximately equal. The transition from oxygen-limited to fuel-limited burning was also observed by X. Wang, Chen, et al. (2019), who measured burning rates at various ambient pressures. The concept of transitioning from oxygen-limited to fuel-limited is important for compartment and tunnel fire scenarios because it determines the method used to estimate the HRR of a fire within a confined space (Ingason, Li, & Lönnermark, 2015).

Apte (1998) measured the burning rate, heat release rate, total heat flux, smoke production, and CO/CO_2 yields of several blends of industrial methylated spirit (95% ethanol and 5% water by volume) with BP solvent 33 (C_6 and C_7 hydrocarbons and less than 0.1% aromatics by volume). The measurements were performed in both a ventilated tunnel and with cone calorimetry using batch pool fires. They found that increasing the concentration of BP-33 enhanced the HRR and smoke production of the fire. All properties except smoke production shown in the study were time-averaged, so the change in fuel properties over time could not be observed.

X. Wang, He, et al. (2018) measured burning rates and HRR in ethanol-kerosene and diethylene glycol dimethyl ether-kerosene blends using a cone calorimeter. It was shown that fuel blends with significantly different volatilites will produce two distinct peak burning rates. The more volatile component will evaporate at a similar rate to its pure burning rate until it is almost depleted of that fuel, after which burning behaviour transitions to that of the less volatile component. They measured burning rates of individual components from the total burning rate and HRR measurements. These measurements agree with the hypothesis of Grumer et al. (1961) that fuels blends with components of widely varying volatilities will burn with two distinct peak burning rates.

The growing usage of electric vehicles has prompted studies on pool fires fuelled by lithium ion battery electrolytes (C. Ding et al., 2019; Eshetu et al., 2014; Fu, Lu, Shi, Cheng, & Zhang, 2016), which contain carbonate-based solvent mixtures with dissolved lithium salt. According to the measurements of C. Ding et al. (2019), the presence of salt increases the luminosity of the flame in the early stages of the fire, but it does not have an appreciable effect on the burning rate and radiant flux to the surroundings. Although a sootier flame will tend to have a higher emissivity, the reduction in temperature associated with incomplete combustion may be significant enough to offset gains in radiant heat flux caused by the increase in the emissivity of the flame. Flame temperature and emissivity measurements in electrolyte solutions are required to confirm this hypothesis. As the fire progresses, more volatile components are depleted, and the concentration of salt increases up to a point where it starts undergoing pyrolysis. The decomposition of salt releases toxic gases and causes self-extinction to occur earlier because the salt has a higher heat of gasification than the solvents. Developments in multicomponent pool fire modelling are necessary to predict the highly transient behaviour of these fires.

2.2.2 Empirical Models

The typical method for estimating the burning rate of a pool fire is to use the model of Babrauskas (1983, 2016):

$$\dot{m}'' = \dot{m}''_{\infty}(1 - e^{-k\beta D}) \tag{2.3}$$

where $\dot{m}''_{\infty}$ is the burning rate per unit area for a pool of infinite diameter ($\mathrm{kg\,m^{-2}\,s^{-1}}$), D is the pool diameter (m), and $k\beta$ is an empirically fit constant ($\mathrm{m^{-1}}$). The model relies on availability of burning rate data for a specific fuel at several pan diameters. Data exists for several petroleum products like gasoline, kerosene, and crude oil, but there are no values available for more complex fuel blends.

The method for estimating the burning rate of multicomponent fuels in the SFPE Handbook (Gottuk & White, 2016) is based on the correlation proposed by Burgess, Strasser, and Grumer (1961) for single-component fuels. Grumer et al. (1961) proposed that the same correlation can be applied to multicomponent fuels by mole-averaging the liquid and gas mixtures:

$$v_{max} = 1.27 \times 10^{-6} \left[\frac{\sum_{i=1}^{N} Y_i \Delta H_c}{\sum_{i=1}^{N} Y_i \Delta H_v + \sum_{i=1}^{N} X_i \int_{T_0}^{T_b} c_p dT} \right] \tag{2.4}$$

where v_{max} is the maximum surface regression rate ($\mathrm{m\,s^{-1}}$), ΔH_c is the heat of combustion ($\mathrm{J\,mol^{-1}}$), ΔH_v is the latent heat of vaporization ($\mathrm{J\,mol^{-1}}$), c_p is the specific heat capacity of the liquid ($\mathrm{J\,mol^{-1}\,K^{-1}}$), T_0 and T_b are the initial and boiling temperature of the liquid (K), and Y_i and X_i are the mole fractions of the vapour and liquid phases, respectively. They then simplify the equation for fuels with similar heats of combustion and heats of vaporization, and approximately equal vapour and liquid compositions:

$$v_{max} = \sum_{i=1}^{N} Y_i v_i \tag{2.5}$$

A more recent correlation for predicting the steady-state burning rate of a generic fuel was proposed by Ditch et al. (2013). The correlation is based on the hypothesis that the steady-state burning rate of a pool fire is dependent only on the heat of gasification, the soot volume fraction of the fuel, and pool diameter:

$$\dot{Q}''_s = \dot{m}'' \Delta H_g = 12.5 + 68.3 Y_s^{1/4} \left\{ 1 - \exp\left[-\left(\frac{4}{3} \Delta H_g D \right)^{3/2} \right] \right\} \tag{2.6}$$

$$\Delta H_g = \Delta H_v + \int_{T_0}^{T_b} c_p dT \tag{2.7}$$

where $\dot{Q}''_s$ is the heat flux to the pool surface (kW), Y_s is the smoke yield, ΔH_g is the heat of gasification (kJ kg^{-1}), ΔH_v is the heat of vaporization (kJ kg^{-1}), c_p is the specific heat capacity of the liquid (J kg^{-1} K^{-1}), and T_0 and T_b are the initial and bubble-point temperature of the fuel (K). The correlation fit well with steady-state burning rate data for continuously fed methanol-toluene, ethanol-toluene, and heptane-toluene pool fires with pan diameters spanning 0.1-1.0 m. The advantage of Eq. (2.6) over Eq. (2.3) is that it depends only on the heat of gasification and soot yield of the fuel; it can be used so long as these properties are known. Since the soot yield is related to the laminar smokepoint (Tewarson, 1984), knowing how the laminar smoke point varies with fuel composition could enable prediction of the burning rate over the entire composition range of the fuel.

2.2.3 Global Models

An alternative method to empirical burning rate correlations is to use a global fire model. In this class of model, the burning rate is predicted by modelling the coupled interaction between the fire and pool surface. The basic framework for a global fire model is displayed in Figure 2.2. The temperature of the flame is used to estimate the heat feedback to the pool surface from radiation, convection, and conduction. Then, the temperature of the flame is re-calculated from the combustion of the vaporized fuel.

Orloff and de Ris (1982) first proposed an algorithm to compute the fuel pyrolysis rate. Heat feedback to the surface was found by computing convective and radiative components of heat transfer, followed by solving the energy balance at the fuel surface:

$$\dot{Q}''_r + \dot{Q}''_c = \dot{m}'' \Delta H_g + \dot{Q}''_{rr} \tag{2.8}$$

where $\dot{Q}''_r$ is radiative heat flux (W), $\dot{Q}''_c$ is convective heat flux (W), and $\dot{Q}''_{rr}$ (W) is heat flux re-radiated from the pool surface.

The flame is assumed to be homogeneous and isothermal such that the burning rate can be computed through an analytical expression. Their method requires prior

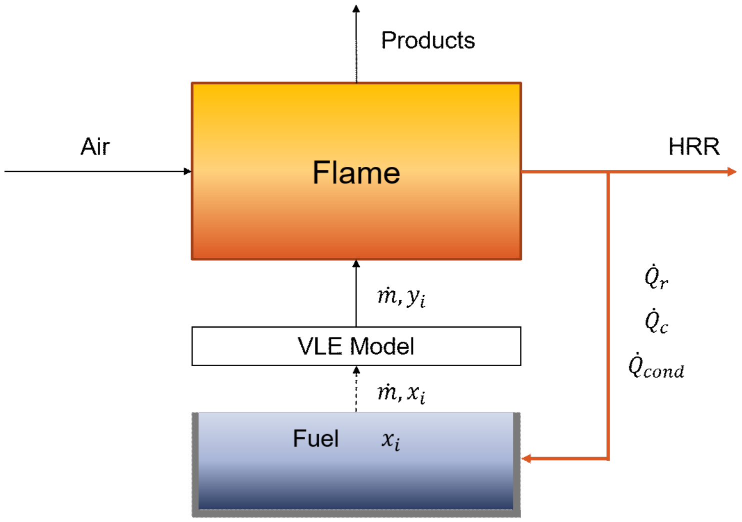

Figure 2.2: Schematic for the basic framework of a global fire model.

knowledge of the flame temperature, radiative fraction, and volumetric heat release rate of the flame. Although the model is convenient, the assumed flame temperature and volumetric heat release rate may not be applicable to all fuels and geometric scales. The homogeneous and isothermal assumptions also result in ignoring inhomogeneous effects like radiation blockage at the pool surface in larger fires (Brosmer & Tien, 1987).

The global model of Hamins, Yang, and Kashiwagi (1999) is a predictive model that only requires the fuel properties, pan size, and ambient conditions as inputs. The model is based on the same energy balance shown in Eq. (2.8). The flame is assumed as cylindrical, grey, and isothermal. The flame temperature is calculated using the same procedure that would be used to obtain the adiabatic flame temperature (Smith, Van Ness, & Abbott, 2005), except that heat losses due to radiation, combustion efficiency, liquid-to-vapour phase change, and dilution from entrained air are considered. The absorption-emission coefficient is calculated based on the soot volume fraction of the fuel. The flame height is calculated using Heskestad's flame height correlation (Heskestad, 1984). The air entrainment rate is calculated using correlations from Delichatsios (1987) modified by an empirical tuning constant.

The merit of using the global model of Hamins et al. (1999) is that it simplifies treatment of the flame and relies on well-known empirical correlations for air entrainment, convective heat transfer, and flame height, while remaining computationally efficient and rooted in physical mechanisms. This makes it a viable candidate for modelling multicomponent fuels, which have properties that vary due to distillation. If data for radiant fraction and combustion efficiency for any particular fuel is missing, it can be related to the laminar smoke point (Tewarson, 1984), which is obtainable through the ASTM smokepoint test (ASTM D1322-18, 2018). The challenge for using the global model with multicomponent fuels would be choosing how to average combustion property data, because it has been shown that averaging individual smoke points of pure fuels is not always applicable for certain fuel mixtures (Ditch et al., 2013).

2.3 Flame Height

The flame height is an important parameter for estimating air entrainment (Heskestad, 2016), radiative heat transfer (Mudan, 1987), and the general size of the fire. The mean flame height is defined by Zukoski, Cetegen, and Kubota (1985) as the height at which the visible flame is present 50% of the time (Heskestad, 2016). The visible flame is defined as a zone made visible by radiation from soot (Zukoski et al., 1985).

Historically, one of the most commonly used correlations for estimating flame heights in a quiescent environment is from Thomas (1963). The expression was derived from data on crib fires:

$$\frac{H}{D} = 42\left(\frac{\dot{m}''}{\rho_\infty\sqrt{gD}}\right)^{0.61} \tag{2.9}$$

where H is the mean flame height (m), ρ_∞ is the ambient air density ($\mathrm{kg\,m^{-3}}$), and g is gravitational acceleration ($\mathrm{m\,s^{-2}}$). Presently, the recommended approach given in the SFPE Handbook (Heskestad, 2016) for estimating flame heights for is to use Heskestad's correlation (Heskestad, 1983) in the form given by McCaffrey (1995):

$$\frac{H}{D} = -1.02 + 3.7\dot{Q}^{*2/5} \tag{2.10}$$

where $\dot{Q}^*$ is the dimensionless heat release rate (also known as a modified Froude number):

$$\dot{Q}^* = \frac{\dot{Q}}{\rho_\infty c_{p\infty} T_\infty \sqrt{gD} D^2} \tag{2.11}$$

$c_{p\infty}$ is specific heat capacity of the ambient air ($\mathrm{J\,kg^{-1}\,K^{-1}}$), T_∞ is ambient temperature (K), and $\dot{Q}$ is heat release rate (W). Another equivalent form of Eq. (2.10) is expressed as follows (Heskestad, 2016):

$$H = -1.02D + 0.235\dot{Q}^{2/5} \tag{2.12}$$

where $\dot{Q}$ is in units of kW. The original correlation given by Heskestad (1983) was fit to a wide variety of fuels and burner diameters. Fuels included methane, propane, gasoline, acetone, methanol, heptane, and transformer fluid, and diameters ranged from 0.1 to 23 m (Heskestad, 2016). For clarity, Eq. (2.10) will be referred to as Heskestad's flame height correlation for the remainder of the document.

Studies measuring flame heights in multicomponent pool fires have only been conducted in batch pool fires. In these studies, the burning rate rather than the HRR was measured. The fuel composition throughout the experiments was generally not measured, which means the composition of the vapour and average heat of combustion were unknown. Since Heskestad's flame height correlation is dependent on HRR, it is difficult to assess the validity of conclusions drawn on whether or not it is applicable to blended fuels.

Liu et al. (2018) cited that for binary mixtures of water and propanol burning in a 0.30 m pan, the average flame heights followed a similar trend to Eq. (2.12). However, the result is inconclusive since an incorrect heat of combustion for pure propanol was used. Even if the correct heat of combustion for pure propanol were used, the average HRR would still be uncertain due to distillation within the pool.

Y. Ding et al. (2014) were able to confirm that Heskestad's flame height correlation predicted similar values to their experiments with ethanol and n-heptane at the azeotropic concentration. X. Wang, Zhou, et al. (2019) also claimed that a non-azeotropic blend of n-heptane and DGM followed Heskestad's correlation, but it is unclear how the heat of combustion of the mixture was averaged. The composition of the vapour phase changed from 82% n-heptane to pure DGM over the course of burning, and the difference in heat of combustion between the two components was

42%. The theoretical maximum HRR will vary by approximately the same amount over the course of burning, so omitting how the heat of combustion was calculated leads to greater uncertainty in whether the fuel blend follows Heskestad's flame height correlation. More flame height data where the HRR is measured is required to verify the applicability of Heskestad's correlation to multicomponent fuels. Simultaneous measurements of burning rate and fuel composition would also be appropriate for estimating the HRR.

2.4 Flame Temperature

Yokoi's experiments with burning wooden cribs of various sizes showed that the temperature distribution of hot gases above a fire source could be categorized into three domains: the continuous, intermittent, and plume regions (1963). Yokoi found relationships between the dimensionless parameters Φ and z/R for each of these regions. Φ is defined as follows:

$$\Phi = \frac{(T - T_\infty)R^{5/3}}{\sqrt[3]{\frac{\dot{Q}_c^2 T_\infty}{c_p^2 \rho_\infty^2 g}}} \tag{2.13}$$

where T is the plume temperature (K), R is the radius of the base (m), and $\dot{Q}_c$ is the convective HRR (W). In the continuous region, the temperature is approximately constant:

$$\Phi = 1.6 \tag{2.14}$$

In the intermittent region, the temperature distribution behaves as though it was from a line source:

$$\Phi = 1.764\left(\frac{z}{R}\right)^{-1} \tag{2.15}$$

where z is the height above the base of the fire (m). In the plume region, the temperature distribution behaves as though it came from a point source:

$$\Phi = 9.115\left(\frac{z}{R}\right)^{-5/3} \tag{2.16}$$

The present approach for estimating fire plume temperatures is to use the following relation that is based on an integral plume model and empirical fitting to experimental data (Heskestad, 1984, 2016):

$$T - T_\infty = 9.1\left(\frac{T_\infty}{c_{p\infty}\rho_\infty g}\right)^{1/3} \dot{Q}_c^{2/3}(z - z_0)^{-5/3} \tag{2.17}$$

where $\dot{Q}_c$ is in kW, $c_{p\infty}$ is in $\mathrm{kJ\,kg^{-1}\,K^{-1}}$, and z_0 is the location of the virtual origin above or below the fire source (m). It should be noted that Eq. (2.17) is only valid at and above the mean flame height. Within the flame, it is estimated that $T - T_\infty$ is approximately 900 K based on data from large pool fire experiments with methanol, heptane, and transformer fluid (Heskestad, 2016; Kung & Stavrianidis, 1982). Combing Eqs. (2.13) and (2.16), and comparing this to Eq. (2.17), it becomes evident that Yokoi's and Heskestad's plume temperature correlations are analogous to one another aside from the difference in empirical constants.

Another technique to estimate temperatures at and below the mean flame height is to use an energy balance approach. The classic example is the adiabatic flame temperature (Smith et al., 2005), where it is assumed that all energy released from combustion goes towards heating the combustion products. In a pool fire scenario, the flame evidently transfers heat to its surroundings, so corrections for radiation losses and heat feedback to the pool surface are required. Other heat losses can be included by considering incomplete combustion and dilution from air entrainment.

Regarding multicomponent pool fires, Y. Ding et al. (2014) observed that the centerline flame temperature of an azeotropic ethanol and *n*-heptane mixture was greater than the flame temperatures measured for both pure fuels. The cause of this phenomenon is inferred to come from lower soot concentrations in the flame. Ethanol is an oxygenating fuel, which leads to nonlinear effects of fuel composition on soot formation (Ditch et al., 2013; Esarte et al., 2009). Lower soot concentrations reduce the luminosity and therefore radiation losses from the flame. Additionally, less soot production implies that there is less incomplete combustion and therefore less heat losses. Consequently, the convective heat release rate increases, and based on Eq. (2.17), this should cause an increase in flame temperature.

Liu et al. (2018) found that centerline plume temperatures in propanol-water pool fires decreased as the alcohol was diluted. The presence of water has multiple ways of reducing the flame temperature. First, there will be less fuel available in the vapour phase, which reduces the HRR, and second, the water vapour requires more energy to heat than the ambient air. Additionally, water vapour is less dense than air, which will result in more air entrainment into the plume and increase the concentration of inert gases in the flame.

2.5 Computational Fluid Dynamics

Many CFD software packages are available for modelling fires and smoke movement, such as Fire Dynamics Simulator (FDS) (McGrattan, McDermott, Hostikka, Floyd, & Vanella, 2019), OpenFOAM (OpenFOAM Foundation, 2019), ISIS (Institut de Radioprotection et de Sûreté Nucléaire, 2019), SIERRA/Fuego (Sandia National Laboratories, 2017), and ANSYS FLUENT (ANSYS, 2009). The ability of CFD to quickly resolve gas-phase dynamics with an acceptable level of detail for complex flows and geometries makes it a useful tool for both researchers and fire safety engineers. In fire safety engineering applications like predicting smoke movement in compartment fires (Hu et al., 2007) and accident consequence analysis (Tavelli, Derudi, Cuoci, & Frassoldati, 2013; Miao, Wenhua, Ji, & Zhen, 2014), pool fires are typically specified as a heat source with a constant heat release rate per unit area, where estimates for HRR are obtained from empirical correlations like Eqs. (2.3), (2.5), and (2.6). Meanwhile, in research-related applications where the objective is to model the pool fire itself, the heat feedback from the flame to the pool and the resulting evaporation is simulated (Hostikka, McGrattan, & Hamins, 2003; Prasad et al., 1999; Sikanen & Hostikka, 2016; Snegirev, 2004; Yao, Yin, Hu, Wang, & Zhang, 2013).

In batch multicomponent pool fires, the burning rate will vary with the changing fuel composition. Since the liquid and vapour properties will change as the pool is distilled, models that predict the burning rate through the heat feedback mechanism are required for predictive CFD modelling. A constant burning rate is only viable if a steady-state fuel composition is reached or if experimental data is available. C. Wang et al. (2014) took this approach to simulate a 0.30 × 0.30 m ethanol-gasoline pool fire using ExfireFoam. The burning rate was set using an experimental burning rate curve to validate the accuracy of the combustion, soot, and radiation models for predicting flame height and axial flame temperature. The the fuel was assumed to remain at its starting composition, but the experimental burning rate data showed the presence of two distinct peak burning rates, which highlights the effects of either distillation (X. Wang, He, et al., 2018) or bulk boiling (Chen, Lu, Li, Kang, & Lecoustre, 2011).

2.5.1 Pyrolysis Models

Obtaining a predictive simulation for a batch multicomponent pool fire requires modelling of distillation in the fuel. This implies tracking the composition of the pool and evaporation rates of individual species. Based on these requirements, predicting the burning rate through pyrolysis modelling is appropriate. Several pyrolysis models used in predictive CFD pool fire simulations are discussed below.

Pyrolysis models can be either heat transfer or mass transfer based. Heat transfer based models correlate the evaporation rate directly with the net heat flux to the fuel surface.

$$\dot{m}'' = \frac{\dot{Q}''_s}{\Delta H_g} \tag{2.18}$$

This type of model can be used if mass transfer resistance is neglected and the surface temperature of the fuel is known. In these cases, the surface and bulk temperature are assumed to be the bubble-point of the fuel. The predicted burning rate is dependent on the accuracy of the radiative, convective, and conductive heat transfer mechanisms to the surface (Hostikka et al., 2003; Snegirev, 2004; Yao et al., 2013). For pool fires with a diameter approaching 0.5 m, radiation becomes the dominant heat transfer mechanism due to diminishing lip effects and the increase in size of the flames (Hottel, 1959; Blinov & Khudyakov, 1961; Gottuk & White, 2016), so accurate estimates of radiation emission and absorption from the gas phase are necessary to obtain reasonable burning rates from heat transfer based pyrolysis models.

Mass transfer based pyrolysis models use the difference of partial pressures at the pool surface and in the bulk gas phase as the driving force for evaporation. One of the earliest approaches was to iteratively change the burning rate until the partial pressure of fuel in the computational cells above the pool was equal to the equilibrium partial pressure of the fuel (Prasad et al., 1999). Novozhilov and Koseki (2004) coupled the mass transfer rate to the energy balance around the pool surface to resolve the surface temperature of the fuel:

$$\dot{m}'' = h_m \frac{PW}{R_g T_g} (y_{f,s} - y_{f,\infty}) \tag{2.19}$$

where h_m is the mass transfer coefficient ($\mathrm{m\,s^{-1}}$), P is pressure (Pa), R_g is the universal gas constant ($\mathrm{J\,mol^{-1}}$), W is the molecular weight of the fuel ($\mathrm{kg\,mol^{-1}}$), T_g is the gas temperature (K) in the cell adjacent to the fuel surface, $y_{f,s}$ is the fuel vapour fraction in the first cell above the fuel surface, and $y_{f,\infty}$ is the fuel vapour fraction in the bulk gas phase.

The present version of FDS (McGrattan, McDermott, et al., 2019) assumes that mass transfer at the fuel surface is governed by Stefan diffusion:

$$\dot{m}'' = h_m \frac{PW}{R_g T_g} \ln\left(\frac{y_{f,s} - 1}{y_{sat} - 1}\right); \quad h_m = \frac{Sh D_g}{L} \tag{2.20}$$

where y_{sat} is the equilibrium fraction of fuel vapour above the pool surface, D_g is the gas diffusion coefficient ($\mathrm{m^2\,s^{-1}}$) in the cell adjacent to the fuel surface, Sh is the Sherwood number, and L is the characteristic dimension (m) of the fuel base. The upper limit to the evaporation rate was assigned to be the same as in Eq. (2.18). This pyrolysis model was used to model pool fires in open, quiescent environments (Sikanen & Hostikka, 2016) and in mechanically ventilated environments (Sikanen & Hostikka, 2017). Segovia, Beji, and Merci (2018) used the same pyrolysis model described in Eq. (2.20) but calculated a local mass transfer coefficient using the distance of the cell from the edge of the pan as L, which caused the mass transfer coefficient to increase by 15 times near the edge of the pan.

The current evaporation model in FDS is unsuitable for multicomponent fuels because Eq. (2.20) was derived for binary diffusion (single-component fuel into air). In multicomponent diffusion, evaporation flux of a species depends on concentrations of other species, and estimation of the diffusion coefficients requires a matrix solution involving diffusion coefficients of all binary pairs (Krishna & Standart, 1979; Taylor & Krishna, 1993). Thus, it would be incorrect to apply Eq. (2.20) to estimate individual mass fluxes of each component. For initial studies on multicomponent fuels, it is simpler and more computationally efficient to use a heat transfer based pyrolysis model. This approach ignores conduction and diffusion resistance in the liquid phase, so it cannot model the initial growth phase of a fire. Thus, a heat transfer based pyrolysis model is most suitable for large-scale pool fire scenarios burning for longer periods of time.

2.5.2 Limitations of Fire Dynamics Simulator

FDS was chosen as the CFD framework to implement a pyrolysis model for multicomponent liquids. This is because FDS is one of the more popular fire modelling tools due to being open source, its modelling flexibility, ease of use, and thorough documentation, making it an attractive option for researchers and fire protection engineers. Additionally, its solid pyrolysis framework makes it an ideal starting point for implementing a multicomponent liquid pyrolysis model.

Presently in FDS, the best way to model a multicomponent liquid pool fire is to specify the mass flux of each species at the pool surface. This requires prior knowledge of the burning rate for each species, which must be obtained either from experimental data or an empirical correlation. Condensed phase pyrolysis models for multicomponent fuels are available in FDS, but the framework is designed to deal with solid fuels, where each species independently pyrolyses from others:

$$\frac{d}{dt}\left(\frac{m_i}{m_0}\right) = -\sum_{\beta=1}^{N_{r,i}} r_{i\beta} + S_i \tag{2.21}$$

$$\dot{Q}''' = -\sum_{i=1}^{N_m} \sum_{\beta=1}^{N_{r,i}} r_{i\beta} H_{r,i\beta} \tag{2.22}$$

where t is time (s), m_i is the mass of species i (kg), m_0 is the initial mass of the solid (kg), $N_{r,i}$ is the number of reactions for the particular species, N_m is the number of materials the solid is made of, $r_{i\beta}$ is the rate of reaction β for species i ($\mathrm{s^{-1}}$), S_i is the generation rate of species i from other reactions ($\mathrm{s^{-1}}$), $\dot{Q}'''$ is the heat generation within the solid ($\mathrm{W\,m^{-3}}$), and $H_{r,i\beta}$ is the heat of reaction generated from reaction β for species i ($\mathrm{W\,m^{-3}}$). The reaction rates are given by an Arrhenius function:

$$r_{i\beta} = \underbrace{\left(\frac{m_i}{m_0}\right)^{n_{r,i\beta}}}_{\text{Reactant concentration}} \underbrace{A_{i\beta}\exp\left(-\frac{E_{i\beta}}{R_g T_s}\right)}_{\text{Arrhenius function}} \times$$
$$\underbrace{[x_{O_2}(z)]^{n_{O_2,i\beta}}}_{\text{Oxidation function}} \underbrace{\max[0, S_{thr,i\beta}(T_s - T_{thr,i\beta})]^{n_{t,i\beta}}}_{\text{Power function}} \tag{2.23}$$

The first term describes the concentration of species i, where $n_{i\beta}$ is the reaction order. The second term is the Arrhenius expression, where $A_{i\beta}$ is the pre-exponential factor (s^{-1}), and $E_{i\beta}$ is the activation energy ($\mathrm{J\,mol^{-1}}$). The third term describes the variation of local oxygen concentration as a function of depth z (m), and the last term sets the threshold temperature for which the reaction will start occurring. With this framework, a phase change reaction for an evaporating multicomponent fuel would be implemented by setting $A_{i\beta} = c_{p,i}$, $E_{i\beta} = 0$, $n_{O_2,i\beta} = 0$, and $T_{thr,i\beta}$ to the bubble-point (T_b) of the mixture. Equation (2.23) would then be divided by $H_{r,i\beta}\Delta t$ to yield the total mass evaporated per time step:

$$m_i \Delta t = \frac{m_i c_{p,i}(T_s - T_{b,i})}{H_{r,i\beta}} \tag{2.24}$$

where the boiling-points of each pure species are used for $T_{b,i}$.

What is currently missing from FDS's pyrolysis framework is the inclusion of vapour-liquid equilibrium (VLE). With the current framework, it is not possible to correct for the vapour phase composition of each component during the simulation. Furthermore, the bubble-point of the mixture will change as more volatile components are distilled, but the bubble-point is a user-specified constant. Finally, FDS treats the liquid the same as a solid, which causes the local mass and properties of the fuel to spatially vary, which is not physically representative of how liquids behave since they are able to flow and mix.

Chapter 3

Experimental Methods

Pool fire experiments can be conducted in either a batch or a continuous mode. In batch mode, the fuel in the pan is ignited and allowed to burn until the fuel is self-extinguished. This method has been commonly used to observe general combustion behaviour in multicomponent pool fires (Eddings et al., 2005; Y. Ding et al., 2014, 2017; Liu et al., 2018; X. Wang, He, et al., 2018). In continuous mode, the pool is constantly replenished at a rate greater than or equal to the burning rate. The continuous method has been used in both single-component pool fire studies (Dlugogorski & Wilson, 2000; Hamins & Lock, 2016; Hu, Liu, & Wu, 2013; Sahu, Kumar, Jain, & Gupta, 2016) and multicomponent pool fire studies (Blinov & Khudyakov, 1961; Eddings et al., 2005; Ditch et al., 2013). The advantage of this method over the batch method is that it keeps a constant lip height, thereby removing any transient lip height effects (Dlugogorski & Wilson, 2000) that would be otherwise present in a batch fire. It also allows the fire to maintain a steady-state burning rate, which is generally the period of interest. Additionally, it enables the pool to reach a steady-state composition. However, real pool fires are generally transient, so it remains important to study batch pool fires.

3.1 Fuel Selection

Experimenting with binary mixtures simplifies analysis on relating combustion behaviour to fuel composition. Vapour-liquid equilibria (VLE) for binary mixtures has also been well-characterized, enabling usage of common thermodynamic models like the Wilson model (Wilson, 1964) to obtain accurate conversions from liquid to vapour compositions above the pool. Additionally, the methods developed for analysing binary mixtures form the foundation for analysing fuels with more than two components. For these reasons, binary mixtures were used in all sets of experiments.

All fuel mixtures selected needed to be flammable at room temperature and consist of completely miscible components. Two other criteria were also specified. The first was if the solution was thermodynamically ideal or nonideal. The second was if the liquid phase contained an inert species. For the context of this work, an inert component is defined as a chemical that is non-combustible and not an oxidizer. This resulted in the following combinations: ethanol-water, ethanol-isopropanol, and ethanol-hexane. A binary ideal mixture that is flammable, has two completely miscible species, and contains only one flammable component was not identified. The pairs are presented in Table 3.1. $x-y$ diagrams for all mixtures tested are provided in Appendix A.

Table 3.1: Fuel Mixtures Used in Experiments

Solution Ideality	Two Flammable Components	One Flammable Component
Ideal	Ethanol-Isopropanol	-
Nonideal	Ethanol-Hexane	Ethanol-Water

The chemicals selected are representative of what may be encountered in a multicomponent pool fire scenario. Ethanol-water should be representative of what may be encountered at any chemical plant producing alcohol products (*e.g.* rubbing alcohol, hand sanitizer, bio-ethanol). Water is naturally abundant, so ethanol-water mixtures can also represent a situation where spilled chemicals mix with a body of water. Ethanol-isopropanol was chosen because it represents an ideal multicomponent fuel where all species are chemically similar and have similar volatilities. This would be seen it transportation fuels like gasoline, diesel, and kerosene. Alcohols were chosen over hydrocarbons to minimize the size of the experimental apparatus. Ethanol-hexane should be representative of a mixture containing hydrocarbons and chemicals with an oxygenating functional group. A practical example is blending ethanol or methanol with transportation fuels.

3.2 Transient Experiments

Experiments with ethanol-water mixtures were conducted at Dalhousie University. The size of the room was 6.3 × 10.6 × 2.4 m. Ambient temperatures ranged between 19 and 22 °C. Combustion products were exhausted into a fume hood via a 150 mm diameter duct located 1.3 m above the pan.

Anhydrous ethanol and de-ionized water were used to make ethanol-water mixtures. The combined volume of pure components for each mixture was 1 L. Concentrations tested were 51-49, 66-34, and 81-19% w/w ethanol-water. The mixtures were burned in an aluminum pan that was 0.30 m in inner diameter (ID), 75 mm deep, and 1.2 mm thick. Burning rates were determined by measuring the mass of the pool with a 4.2 kg analytical balance with an accuracy of 0.01 g. A 20 mm thick slab of high-temperature insulation board was placed between the pan and balance to avoid damaging the balance.

Flame temperature was recorded using K-type thermocouples with a 1.0 mm bead diameter and exposed junction. Four thermocouples were vertically spaced at 70 mm intervals starting 200 mm from the bottom of the pan. The temperature of the liquid was measured using three K-type thermocouples with a bead diameter of 1 mm and a grounded junction. They were placed near the pan rim, approximately 3 mm above the bottom of the pan.

Liquid samples were drawn at 1 minute intervals using a 10 mL syringe. The draw tube was located close to the rim of the pan, about 3 mm above the base of the pan. The volume of each sample was 2-5 mL, and they were stored in a sealed 10 mL vial at room temperature prior to composition measurement. Sample sizes decreased as the fuel approached its bubble-point due to the vapours filling the head space of the syringe. Ethanol concentrations were measured using Fourier-transform infrared spectroscopy (FTIR). The maximum difference between the concentration of ethanol-water calibration standards and the concentration predicted by the fitted calibration curve was ±0.5% w/w.

3.3 Steady-State Experiments

Experiments with ethanol-water mixtures were conducted at Dalhousie University, while ethanol-isopropanol and ethanol-hexane mixtures were burned at the Royal Canadian Navy's Damage Control School in Herring Cove, Nova Scotia. The same room described in Section 3.2 was used at Dalhousie University. The room at the Damage Control School was 6.3 × 10.6 × 2.4 m and 7.6 × 6.1 × 3.2 m. Combustion products were exhausted through a vent in the ceiling.

Ethanol-water experiments were conducted in a 0.30 m ID, 30 mm deep, and 1.2 mm thick aluminum pan. Combustion products were exhausted through an exhaust duct 1.3 m above the pan. The pan was placed at the center of a 610 × 610 × 3 mm aluminum plate with a 200 × 200 mm hole cut out in the center to allow access to the bottom of the pan. At the Royal Canadian Navy's Damage Control School, ethanol-isopropanol and ethanol-hexane mixtures were burned in a 0.30 m ID carbon steel pan with a 7.3 mm thick rim. The rim was 30 mm tall and was welded onto a 6.3 mm thick carbon steel sheet. Each pan contained a 4.5 mm ID, 0.7 m long stainless steel coil that was fixed 15 mm above the base of the pan from which the feed could enter. The carbon steel pan is shown Figure 3.1.

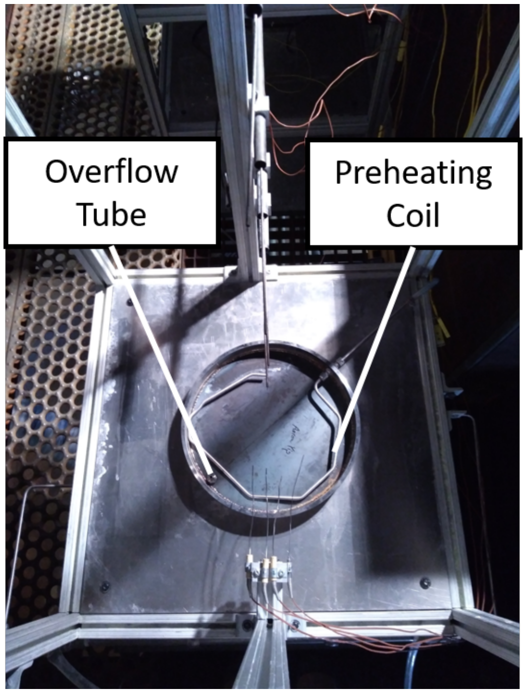

Figure 3.1: Carbon steel pan used for steady-state experiments.

A constant-head tank was used to feed fuel to the pan. The tank was made of a 0.2 m ID PVC pipe and was 0.46 m tall. The flow rate was measured with a 20 kg top-loading balance (Radwag WLC 20/A2) that had an accuracy of 0.1 g. The flow rate was set *a priori* by adjusting the hydraulic head in the tank. The flow rate for each mixture was set such that the time to reach steady-state concentration was no more than 30 minutes. This was determined by performing a mass balance around the system using with an empirically estimated burning rate. The method is showcased in Appendix B. The feed was fed into a funnel connected to the pan to avoid any disturbances to the balance reading. A 0.6 × 0.6 m heat shield was placed between the feed tank and the fire as an added safety precaution. The feed was preheated by passing it through the coil inside the pan.

The fuel level in the pan was maintained constant through use of a 4.5 mm ID vertical stainless steel overflow tube, which was located 127 mm away from the center of the pan. The tip of the tube was 20 mm above the base of the pan, maintaining the fuel level 10 mm below the rim. The tube passed through a water-cooled heat exchanger and then into a collection tank. The outlet of the tube was 127 mm below the underside of the pan to ensure there was enough hydrostatic head to prevent liquid accumulation in the pan. The flow rate into the tank was measured with the same type of top-loading balance as the feed. The burning rate was taken as the difference between the feed rate and overflow rate, and balance data was recorded every second.

The flame shape and height were recorded with a Logitech C920 camera, and data was processed every second. The flame height was measured by contouring the flame and measuring the vertical distance between the lowest and highest point of the contour. An intermittency plot of the flame height was created from these measurements, and the mean flame height was taken as the height where the intermittency of the flame was 50%. The image processing procedure is given in Appendix C.

Gas and liquid temperatures were measured using K-type thermocouples. Thermocouples with an exposed junction and bead diameter of 1.0 mm were positioned at heights of 0.2, 0.3, 0.4, 0.6, 0.8, and 1.0 m above the rim of the pan. Another thermocouple was placed behind the feed tank to measure the ambient temperature. Thermocouples with a grounded junction and a bead diameter of 1.0 mm were positioned inside the pool at heights 5, 10, and 20 mm above the bottom of the pan. A K-type surface thermocouple was placed on the underside of the pan 75 mm away from the center of the pan. Thermocouple data was recorded every 0.5 s.

Each experiment was run for approximately 30 min to allow a steady-state to be reached. Before shutting off the feed at the end of an experiment, a fuel sample of 10 mL was taken to obtain the steady-state concentration of the fuel surface. The sample port was connected to the overflow tube and located after a water-cooled heat exchanger. For ethanol-water and ethanol-hexane mixtures, the composition was determined using a density meter (Anton Paar DMA 35) with an accuracy of 0.1 $\mathrm{kg\,m^{-3}}$ and 0.1 °C. A program within the density meter was used to convert the density to concentration for ethanol-mixtures. The composition of ethanol-hexane mixtures was interpolated from temperature and density data (Feitosa, Caetano, Cidade, & de Sant'Ana, 2009) with an accuracy of 0.2% w/w. For ethanol-isopropanol mixtures, the composition was determined using FTIR. The maximum difference between the concentration of ethanol-isopropanol calibration standards and the concentration predicted by the fitted calibration curve was ±0.5% w/w. A schematic and some photographs of the experimental setup are shown in Figures 3.2 and 3.3, respectively. The heat shield between the tank and main apparatus was removed in Figure 3.3c for viewing purposes.

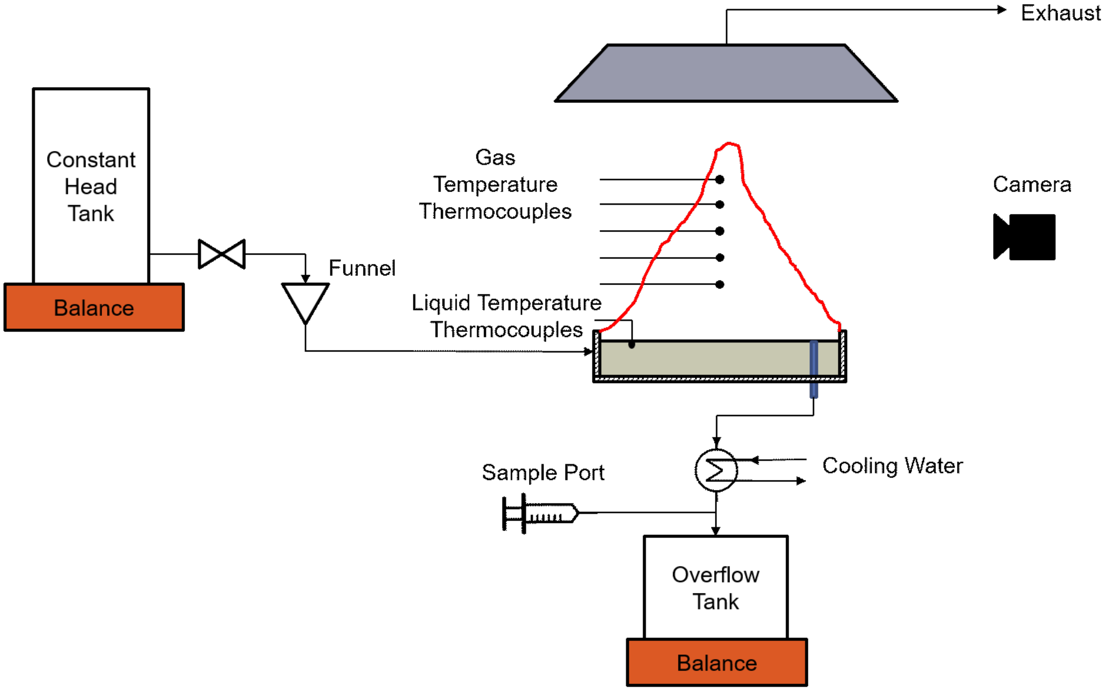

Figure 3.2: Schematic of the experimental layout.

Steady-state burning rates, temperatures, and flame heights were time-averaged using the last 15 minutes of each experiment before the fuel was shut off. Fuel feed rates, initial and steady-state liquid compositions, and ambient temperatures are given in Table 3.2. The times listed are relative to the start of data collection. Ignition times relative to the start of data collection can be found in Appendix D.

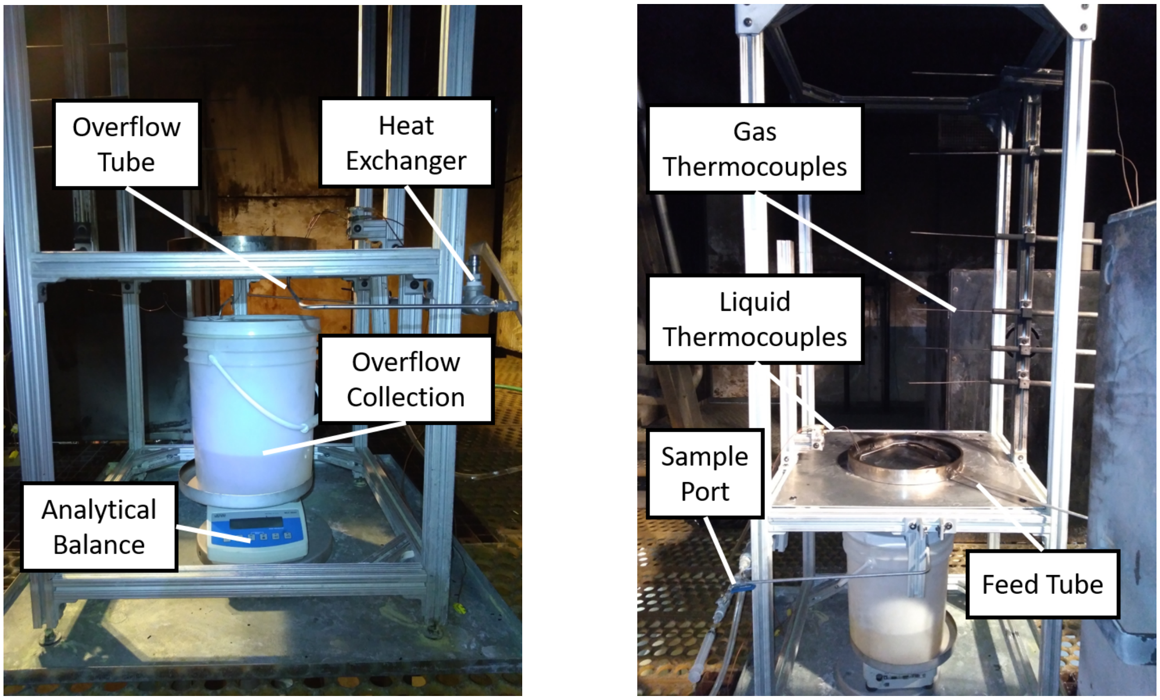

(a) Front view (b) Rear view

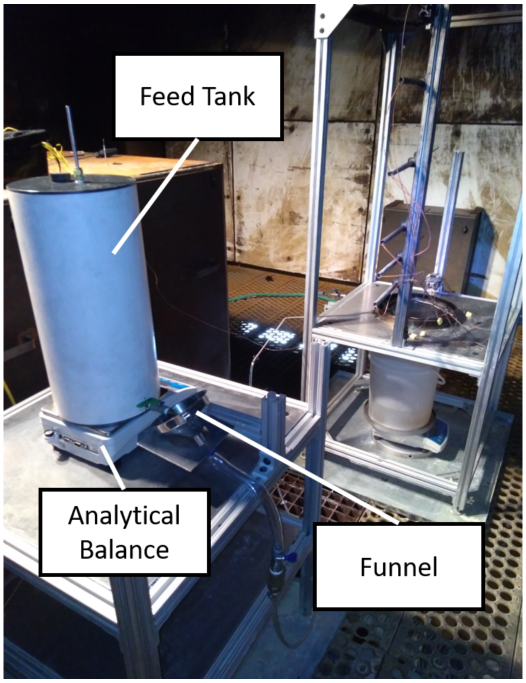

(c) Side view

Figure 3.3: Photographs of the experimental setup at the Damage Control School.

Table 3.2: Feed Composition ($x_{0,EtOH}$), Steady-State Surface Composition (x_{EtOH}), Feed Rate, and Other Conditions in Steady-State Experiments

$x_{0,EtOH}$ (% w/w)	x_{EtOH} (% w/w)	Feed Rate ($\mathrm{g\,s^{-1}}$)	Ambient Temperature (°C)	Time-Averaging Period (s)
Ethanol-Water				
100.0	100.0	3.12 ± 0.04	26.9	1500-2400
84.9	83.3	3.09 ± 0.02	26.0	2100-3000
68.5	63.8	2.78 ± 0.08	25.4	2000-2900
50.0	43.1	3.18 ± 0.02	23.8	1600-2500
35.0	27.8	2.92 ± 0.00	23.8	3000-3900
Ethanol-Isopropanol				
100.0	100.0	1.86 ± 0.02	14.9	1300-2200
84.3	81.7	1.93 ± 0.02	22.4	2100-3000
70.7	66.8	1.92 ± 0.02	23.4	1700-2600
52.0	50.7	1.93 ± 0.02	25.8	1600-2500
32.2	33.2	2.13 ± 0.02	26.7	2000-2900
15.3	15.8	2.01 ± 0.02	15.7	1100-2000
0.0	0.0	2.12 ± 0.01	13.9	2600-3500
Ethanol-Hexane				
100.0	100.0	1.86 ± 0.02	14.9	1300-2200
89.7	95.8	2.68 ± 0.05	26.3	2100-3000
79.1	93.6	2.83 ± 0.06	12.5	1600-2500
66.2	87.8	2.92 ± 0.06	26.3	1500-2400
50.9	70.1	3.12 ± 0.07	14.0	1400-2300

3.4 Thermocouple Radiation Correction

A thermocouple within a flame will not record the true gas temperature because of radiation losses to the cooler surroundings. Thus, final recorded temperatures were radiation corrected using a calibration curve that gave the difference between measured temperature and true gas temperature. The calibration curve was created by measuring temperatures along the centerline of a butane bunsen burner with a 1.0 mm and 0.5 mm diameter exposed junction K-type thermocouple suspended perpendicular to the direction of flow. A bunsen burner was chosen as the calibration system because it provides a more stable flame compared to a pool fire.

There are some characteristics that differ between the flames of a bunsen burner and pool fire. These may result in different temperature readings between systems for the same true gas temperature. The bunsen burner is a pre-mixed flame that has a higher gas velocity and blue flame (no soot deposition). Meanwhile, the pool fires produce a buoyant plume with a luminous flame (soot present). Since the bunsen burner has a higher gas velocity, the thermocouple will read closer to the true gas temperature due to higher rates of convective heat transfer. However, in pool fire flames, soot deposition on the thermocouples may lower the emissivity of the thermocouple bead (De Falco et al., 2017), thereby reducing radiation losses. The extent to which these differences influence the temperature readings is difficult to quantify, so the present methodology can only provide a rough estimate of the temperature correction in the pool fire experiments.

Each trial was conducted separately to avoid radiative heat exchange between the thermocouples. For all trials, the valve on the bunsen burner was fully opened and the air vent was kept in the same position. Each trial was conducted for at least three minutes, and the average temperature of the last two minutes was taken. A picture of one of the trials is shown in Figure 3.4. The temperature readings at each height are provided in Table 3.3.

The true gas temperature was estimated from the assumption that a zero-diameter thermocouple will undergo no radiation losses (Daniels, 1968; Walker & Stocks, 1968). This extrapolation method was chosen because it is simple to implement and yields errors of only 3-5% in comparison to the more accurate techniques at temperature

Figure 3.4: A 0.5 mm thermocouple suspended 52 mm above a butane bunsen burner.

Table 3.3: Time-averaged Thermocouple Readings for a 0.5 mm ($T_{TC_{0.5}}$) and 1.0 mm ($T_{TC_{1.0}}$) K-type Thermocouple at Various Heights Above a Bunsen Burner Rim

Height (mm)	$T_{TC_{0.5}}$(°C)	$T_{TC_{1.0}}$(°C)
20	960 ± 36	818 ± 11
52	1351 ± 8	1132 ± 2
111	1342 ± 51	1088 ± 22
160	575 ± 95	523 ± 69
200	324 ± 44	310 ± 29

ranges of 600-1500 K (Lemaire & Menanteau, 2017). The following equation represents the calibration curve displayed in Figure 3.5:

$$T_g - T_{TC_{1.0}} = 0.571 T_{TC_{1.0}} - 169.9 \tag{3.1}$$

where T_g is the estimated true gas temperature (°C) and $T_{TC_{1.0}}$ is the temperature reading from the 1.0 mm thermocouple (°C). Standard error on the slope and intercept were 0.063 and 52.9, respectively. The large error on some of the points were due to the instability of the flame at higher locations in the plume. Non-corrected thermocouple readings from the pool fire experiments are provided in Appendix D.

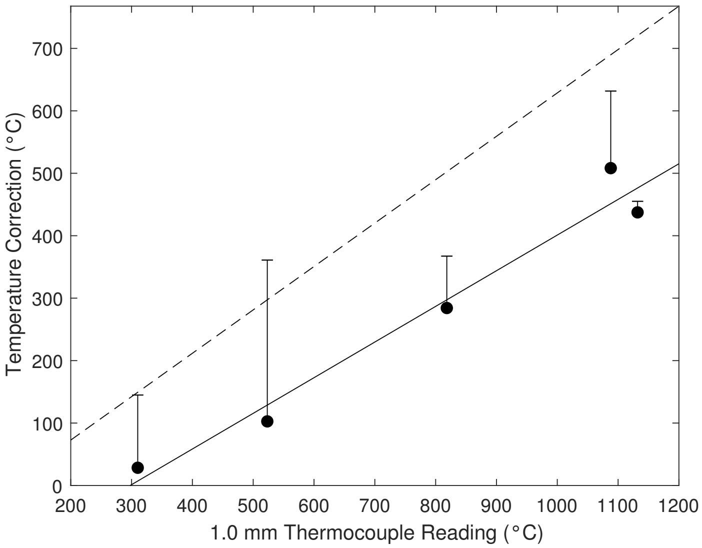

Figure 3.5: Temperature correction calibration curve for a 1.0 mm K-type thermocouple. The solid line represents Eq. (3.5). The dashed line represents upper bound of the 95% confidence interval. Error bars represent one standard deviation.

Chapter 4

Empirical and Global Models

This chapter presents empirical and global modelling methodologies for predicting fire dynamics in multicomponent pool fires. First, a method for predicting distillation in batch pool fires was proposed and validated against results from the batch pool fire experiments described in Section 3.2. Then, predictions from empirical and global models were compared to steady-state data from the experiments described in Section 3.3. General trends in combustion behaviour were identified for several types of binary mixtures.

Heats of combustion (ΔH_c) were obtained from Drysdale (1998), combustion efficiencies (χ_a), radiant fractions (χ_r), and soot volume fractions (f_v) were obtained from Hamins et al. (1999), and laminar smoke points (l_s) were obtained from Tewarson (1984). These properties are listed in Table 4.1. Thermo-physical properties were calculated using correlations from Perry's Chemical Engineers' Handbook (Green & Perry, 2007). Property correlations are listed in Appendix E.

Table 4.1: Combustion Properties Used in Empirical and Global Models

Species	ΔH_c (kJ kg^{-1})	χ_a	χ_r	l_s (mm)	f_v
Ethanol	26800	0.92	0.23	227	0.07×10^{-6}
Isopropanol	33100	0.92[a]	0.30	220	0.07×10^{-6} [a]
Hexane	41500	0.93	0.30	154	0.29×10^{-6}
Water	0	0.00	0.00	N/A[b]	0.00

[a] Assumed to be the same as for ethanol due to absence of experimental data.

[b] Specified as 10^6 mm so that $Y_s \approx 0$ for water when using Eq. (4.5).

4.1 Distillation Model

Similar to the ideal mixture model of Law (1976), the pool was assumed to be well-mixed, meaning it would be uniform in composition and temperature. This mixing model was chosen because there is some degree of mixing driven by convection cells in the liquid, and when the bottom pan boundary is close to the bulk temperature of the liquid, the temperature distribution also appears fairly uniform (Vali et al., 2015). Treating the pool similarly to a batch distillation is a first step to estimating the liquid composition over time. Differences in surface composition predicted using different liquid mixing models is subject to future work.

Selective evaporation of more volatile components was modelled by coupling the liquid and vapour phase compositions and tracking evaporation rates of individual components. For an ideal gas phase and non-ideal liquid phase, the composition of the liquid and vapour phases are coupled by a modified Raoult's law:

$$Y_i P = X_i \gamma_i P_i^{sat}(T_b) \tag{4.1}$$

where P is atmospheric pressure (Pa), $P_i^{sat}(T_b)$ is the saturation pressure (Pa) of the i^{th} component at the bubble-point temperature (T_b) of the mixture (K), X is liquid mole fraction, Y is vapour mole fraction, and γ is the activity coefficient. For mixtures presented in this work, activity coefficients were determined using the Wilson activity model (Wilson, 1964). Binary interaction coefficients were obtained from Aspen HYSYS V10. $x{-}y$ diagrams created from Eq. (4.1) for all binary mixtures tested are provided in Appendix A.

The mass burning rate of the pool, $\dot{m}$ ($\mathrm{kg\,s^{-1}}$), was used to calculate the burning rate of individual components:

$$\dot{m}_i = y_i \dot{m} \tag{4.2}$$

where y_i is the vapour mass fraction of the i^{th} component. For transient pool fires, the mass of each component was monitored by integrating the individual burning rates:

$$\Delta m_i = \int_0^t \dot{m}_i dt \tag{4.3}$$

The composition of the liquid phase was then updated using m and m_i:

$$x_i = \frac{m_i}{m} \tag{4.4}$$

where x_i is the liquid mass fraction of component i.

4.2 Empirical Models

Two commonly known empirical models were adopted to find the burning rate of the pool. The model of Grumer et al. (1961) was not considered because it is only applicable to pools that have a diameter greater than one meter (Gottuk & White, 2016). The model of Babrauskas (1983) is given by the following expression:

$$\dot{m}_i'' = \dot{m}_\infty''(1 - e^{-k\beta D}) \tag{2.3}$$

where $\dot{m}_i''$ is the mass flux of pure component i ($\mathrm{kg\,m^{-2}\,s^{-1}}$), $\dot{m}_\infty''$ is the mass flux for a pool of infinite diameter ($\mathrm{kg\,m^{-2}\,s^{-1}}$), $k\beta$ ($\mathrm{s^{-1}}$) is an empirical constant, and D is the pool diameter (m). The model of Ditch et al. (2013) is given by the following expression:

$$\dot{Q}_s'' = \dot{m}''\Delta H_g = 12.5 + 68.3 Y_s^{1/4}\left\{1 - \exp\left[-\left(\frac{4}{3}\Delta H_g D\right)^{3/2}\right]\right\} \tag{2.6}$$

where $\dot{Q}_s''$ is the net heat flux to the pool surface ($\mathrm{kW\,m^{-2}}$). The other variables in Eq. (2.6) are given as follows:

$$\Delta H_g = \Delta H_v + \int_{T_0}^{T_b} c_p dT \tag{2.7}$$

$$Y_s = 0.0503 \ln\left(\frac{0.296}{l_s}\right) \tag{4.5}$$

$$\frac{1}{l_s} = \sum_{i=1}^{N} \frac{y_i}{l_{s,i}} \tag{4.6}$$

where ΔH_g is the heat of gasification ($\mathrm{kJ\,kg^{-1}}$), ΔH_v is the heat of vaporization ($\mathrm{kJ\,kg^{-1}}$), c_p is the specific heat capacity of the liquid ($\mathrm{kJ\,kg^{-1}\,K^{-1}}$), T_0 is the initial temperature of the mixture (K), Y_s is the soot yield of the fuel, and l_s (m) is the laminar smoke point of the fuel. Equation (4.5) was obtained from Tewarson (1984), who fit it to smoke point measurements from a variety of hydrocarbons and alcohols.

For Babrauskas's correlation, the burning rate was calculated from the vapour mass-averaged sum of pure component burning rates:

$$\dot{m}'' = \sum_{i=1}^{N} \dot{m}_i'' y_i \tag{4.7}$$

Heskestad's flame height and flame temperature models are as follows:

$$\frac{H}{D} = -1.02 + 3.7\dot{Q}^{*2/5} \tag{2.10}$$

$$\dot{Q}^* = \frac{\dot{Q}}{\rho_\infty c_{p\infty} T_\infty \sqrt{gD} D^2} \tag{4.8}$$

$$\dot{Q} = \dot{m} \sum_{i=1}^{N} y_i \Delta H_{c,i} \tag{4.9}$$

$$T - T_\infty = 9.1\left(\frac{T_\infty}{c_{p\infty}\rho_\infty g}\right)^{1/3} \dot{Q}_c^{2/3}(z - z_0)^{-5/3} \tag{2.17}$$

where H is the mean flame height (m), $\dot{Q}^*$ is the dimensionless heat release rate (HRR), $\dot{Q}$ is the total HRR (kW), $\dot{Q}_c$ is the convective HRR (kW), $c_{p\infty}$ and ρ_∞ are the specific heat capacity ($\mathrm{kJ\,kg^{-1}\,K^{-1}}$) and density ($\mathrm{kg\,m^{-3}}$) of air at the ambient temperature T_∞ (K), g is gravitational acceleration ($\mathrm{m\,s^{-2}}$), z is the height above the pool surface, and z_0 is the virtual origin of the plume assuming the fire behaves as a point source. For plotting gas temperature data against Heskestad's flame temperature correlation, the virtual origin was calculated using the following correlation recommended by Heskestad (2016):

$$\frac{z_0}{D} = -1.02 + 0.083\frac{\dot{Q}^{2/5}}{D} \tag{4.10}$$

where $\dot{Q}$ is in kW and D is in m. The convective HRR, $\dot{Q}_c$ (kW), was calculated by subtracting radiative heat losses from the total HRR:

$$\dot{Q}_c = \dot{Q}(1 - \chi_r) \tag{4.11}$$

where χ_r is the mass-averaged radiant fraction of the vapour.

4.3 Global Model

The global model of Hamins et al. (1999) was originally developed for use with single-component pool fires. In this work, it was adapted to predict burning rates for multicomponent fuels. In the global model, the total burning rate was calculated based on the heat feedback to the fuel surface. Assuming that the pool is well-mixed and that heat losses from the pan to the environment are negligible, the burning rate can be found from the energy balance around the pool:

$$\dot{m}\Delta H_g = \dot{Q}_{cond} + \dot{Q}_c + \dot{Q}_r - \dot{Q}_{rr} \tag{4.12}$$

where $\dot{Q}_{cond}$ and $\dot{Q}_c$ are the net rates of heat transfer to the pool (W) by conduction and convection, and $\dot{Q}_r$ and $\dot{Q}_{rr}$ are heat transfer rates (W) to the pool by radiation and reradiation. In this work, conduction was neglected because the pan was 0.30 m in diameter. For this pan size, the burning regime is in the transition zone between laminar and turbulent, where convection and radiation will be the dominant modes of heat transfer (Hottel, 1959; Blinov & Khudyakov, 1961).

Convective heat transfer from the flame to the pool surface was estimated based on the stagnant film theory developed by Spalding (1953). Although the theory was initially developed for purely convective heat transfer, it has been shown that including radiative heat transfer to the surface does not modify the form of the boundary condition at the pool surface (Quintiere, 2006), so the problem can treated the same way as the purely convective formulation. The convective heat transfer to the fuel surface is then given by the following expression:

$$\dot{Q}_c = A\frac{h}{c_{p\infty}}\left[\frac{\Delta H_c(\chi_a - \chi_r)}{\chi_a r} - c_{p\infty}(T_s - T_\infty)\right]\frac{\lambda}{e^{\lambda} - 1} \tag{4.13}$$

where $\lambda = \dot{m}c_{p\infty}/(hA)$, $c_{p\infty}$ is the heat capacity of air ($\mathrm{J\,kg^{-1}\,K^{-1}}$) at the film temperature $(T_f + T_s)/2$, h is the convective heat transfer coefficient ($\mathrm{W\,m^{-2}\,K^{-1}}$), ΔH_c is the heat of combustion ($\mathrm{J\,kg^{-1}}$), r is the stoichiometric air-to-fuel mass ratio of the fuel vapour, χ_a is combustion efficiency, and χ_r is radiative heat loss fraction. The assumptions required to derive Eq. (4.13) are as follows (Quintiere, 2006):

1. Steady burning
2. Chemical reaction time scale << diffusion time scale (flame sheet approximation)
3. Only laminar transport process in the direction normal to the pool surface are considered
4. Specific heat capacity is equal and constant for all species
5. Lewis number is unity
6. No concentration gradient in the liquid phase

All the above assumptions should hold for a multicomponent fuel as well as they do for a single-component system, except for the absence of a concentration gradient in the liquid phase because it has been shown that a concentration gradient forms near the surface of a multicomponent fuel (Eddings et al., 2005). Presence of the concentration gradient adds another mass transfer resistance in the liquid phase, which modifies the boundary condition at the fuel surface and therefore the entire solution. The presence of the concentration gradient also guarantees that the surface is at a different temperature than the rest of the pool. Therefore, heat transfer also occurs due to this effect. However, since the pool was assumed as well-mixed, the assumption that no concentration gradient exists holds. Average properties of the gas phase were used in Eq. (4.13).

The convective heat transfer coefficient was calculated using the following correlation for natural convection over a horizontal hot plate (Lloyd & Moran, 1974):

$$Nu = \begin{cases} 0.54 Ra^{1/4} & 10^4 < Ra < 10^7 \\ 0.15 Ra^{1/3} & 10^7 < Ra < 10^{11} \end{cases} \tag{4.14}$$

where $Nu = hD/k$ is the Nusselt number and Ra is the Rayleigh number, which is equal to the product of the Prandtl number (Pr) and the Grashof number (Gr):

$$Ra = PrGr \tag{4.15}$$

$$Pr = \frac{c_p \mu}{k} \tag{4.16}$$

$$Gr = \frac{1}{T}\frac{gD^3(Ts - T_\infty)}{(\mu/\rho)^2} \tag{4.17}$$

where μ is dynamic viscosity (Pa s) and k is thermal conductivity (W m^{-1} K^{-1}). Thermo-physical properties were evaluated at the film temperature, $(T_s + T_f)/2$. Using Eq. (4.14) requires assuming that the effect of the lip height on h is negligible. If flow over the pool is assumed to be similar to flow past a cavity, then the effect of the lip is small (Hamins et al., 1999; Yamamoto, Seki, & Fukusako, 1979).

Radiation to the fuel surface was calculated by treating the flame as a gray, homogeneous, and isothermal cylinder:

$$\dot{Q}_r = \sigma A(T_f^4 - T_s^4)(1-\rho)[1-(1-\varepsilon_{soot})(1-\varepsilon_{H_2O})(1-\varepsilon_{CO_2})] \tag{4.18}$$

$$\dot{Q}_{rr} = \sigma A(T_s^4 - T_\infty^4) \tag{4.19}$$

where σ is the Stefan-Boltzmann constant (W m^{-2} K^{-4}), T_f is the flame temperature (K), T_s is the surface temperature of the pool (K) and was assumed as the bubble-point, ρ is surface reflectivity of the pool, and ε is emissivity of the flame. Surface reflectivity was assumed to be constant ($\rho = 0.08$) as in Hamins et al. (1999). This value is representative of experimental data for incident angles between 20° and 55° (Hamins, Fischer, Kashiwagi, Klassen, & Gore, 1994). The emissivities for water and carbon dioxide gas were calculated using the algorithm of Leckner (1972), which is given in Appendix F. The emissivity of soot was calculated using the same method as Hamins et al. (1999):

$$\varepsilon_{soot} = 1 - e^{-\kappa L} \tag{4.20}$$

$$\kappa = \frac{3.6 C_1 T_f}{C_2} \tag{4.21}$$

$$C_1 = \frac{36\pi f_v n^2 s}{[n^2 - (ns)^2] + 4n^4 s^2} \tag{4.22}$$

$$L_m = \frac{3.6V_f}{A_f} \tag{4.23}$$

where κ is the effective soot emission parameter ($\mathrm{m^{-1}}$), L is the path length (m), L_m is the mean beam length (m), C_1 is the dimensionless effective soot concentration parameter, $C_2 = 0.014\,388\,\mathrm{m\,K}$ is Planck's second constant, f_v is the soot volume fraction of the fuel vapour, $n = 3.49$ and $s = 2.17$ are infrared averaged optical constants taken from Tien and Lee (1982), V_f is the flame volume ($\mathrm{m^3}$), and A_f is the flame surface area ($\mathrm{m^2}$). Since the flame geometry was assumed to be homogeneous and gray, the mean beam length was used as the characteristic path length in Eq. (4.20). For a cylindrical flame, the flame's volume and surface area are given by the following expressions:

$$V_f = \frac{\pi D^2}{4} H \tag{4.24}$$

$$A_f = 2\frac{\pi D^2}{4} + \pi D H \tag{4.25}$$

The flame height was calculated using Heskestad's flame height correlation (Eq. (2.10)).

Selection of the air entrainment model is important because the flame temperature is highly sensitive to it. An ideal air entrainment model would yield realistic flame temperatures and burning rates for all pool diameters. Empirical correlations from Delichatsios (1987), Heskestad (2016), and Palazzi, Caviglione, Reverberi, and Fabiano (2017) did not yield realistic flame temperatures and burning rates for pure fuels when used in the current model. Thus, the air entrainment rate was set proportional to the stoichiometric air-to-fuel ratio of the vapour mixture. The formulation is as follows:

$$\dot{m}_a = 1.55r \tag{4.26}$$

where $\dot{m}_a$ is the air entrainment rate ($\mathrm{kg\,s^{-1}}$). This method sets the flame temperature as constant for a particular fuel, regardless of diameter. In reality, the average flame temperature depends on the HRR (Heskestad, 2016), and therefore also on the burning rate, which is a function of the pool diameter (Ditch et al., 2013). Investigation into a more sophisticated entrainment model is recommended. The current method yielded acceptable burning rates for all pure fuels across a wide range of diameters. These results are provided in Appendix G.

The flame temperature was found through an energy balance around the flame volume, which is given by the following equation:

$$\underbrace{\sum \dot{m}_i \Delta H_{c,i}(\chi_{a,i} - \chi_{r,i})}_{\text{Enthalpy of combustion}} = \underbrace{\sum \dot{m}_i \int_{T_b}^{T_{ref}} c_{p,i}\, dT + \dot{m}_a \int_{T_\infty}^{T_{ref}} c_{p\infty}\, dT +}_{\text{Sensible enthalpy}}$$

$$\underbrace{\sum \dot{m}_{products,j} \int_{T_{ref}}^{T_f} c_{p,j}\, dT}_{\text{Sensible enthalpy}} + \underbrace{\sum \dot{m}_i \Delta H_{g,i}}_{\text{Enthalpy of vaporization}} \tag{4.27}$$

where $T_{ref} = 298\,\mathrm{K}$ is a reference temperature. For clarity, the subscript i has been used when referring to the evaporating fuel mixture, while subscript j has been used when referring to the reactant or product mixtures. The reactants are composed of the fuel vapour and air. The mass flow rate of products was found based on a mass balance and is given as follows:

$$\dot{m}_{products,j} = \begin{cases} \dot{m}_i(1 - \chi_{a,i}) & \text{species } i \text{ in fuel} \\ \dot{m}_a y_{O_2} - \nu_{O_2} M_{O_2} \sum \frac{1}{\nu_i M_i} \dot{m}_i \chi_{a,i} & \mathrm{O_2} \\ \dot{m}_a y_{N_2} & \mathrm{N_2} \\ \nu_{CO_2} M_{CO_2} \sum \frac{1}{\nu_i M_i} \dot{m}_i \chi_{a,i} & \mathrm{CO_2} \\ \nu_{H_2O} M_{H_2O} \sum \frac{1}{\nu_i M_i} \dot{m}_i \chi_{a,i} & \mathrm{H_2O} \end{cases} \tag{4.28}$$

where ν is the stoichiometric coefficient of the corresponding species in the complete combustion reaction of the fuel with air, and M is molecular weight ($\mathrm{kg\,mol^{-1}}$).

The burning rate and flame temperature were solved numerically using the *ode15s* differential algebraic equation solver in MATLAB. The solution algorithm used is as follows:

1. Define initial and ambient conditions (ambient, mixture properties)

2. Calculate mixture properties

3. Solve for the mixture bubble-point and vapour composition
4. Solve system of equations for burning rate and flame temperature
5. For a transient fire, include Eqs. (4.3) and (4.4) in the system of equations and repeat Steps 3 and 4 for the desired number of time steps

4.4 Results

4.4.1 Batch Pool Fires

Burning rates and pool compositions for each ethanol-water mixture are plotted over time in Figure 4.1. Each trial was performed in duplicate, but fuel samples were taken only from the first trial. Marginal differences in burning rates between trials were present. The sharp transitions in the burning rate curves indicate that the fire goes through a growth, transition, maximum burning, and decay phase. The fire reached its maximum burning rate when the fuel started boiling, which was around 300 s after ignition in each experiment. The transition in burning rate caused by distillation is not evident because the pool undergoes heating for the initial half of the experiment. Additionally, the x-y diagram for ethanol-water (see Appendix A) indicates that the change in vapour composition between ethanol concentrations of 30 and 80% w/w is on the order of 10%, so the heat released from combustion (and therefore the burning rate) should not change much while the pool is in this composition range.

The Babrauskas model gave reasonable predictions for the burning rate after the initial growth phase but underpredicted the maximum burning rate. This is because the model was fit to data from ethanol pool fires that were continuously fed with fresh fuel (Rasbash, Rogowski, & Stark, 1956; Corlett & Fu, 1966), so the bulk of the pool was always below the boiling point. As a result, sensible heating losses reduce the maximum burning rate. Contrarily, when bulk boiling occurs in a batch system, no more energy is required for sensible heating of the liquid, so the burning rate appears as enhances compared to a continuously fed system. The global model was also tuned to burning rates in continuously fed pool fires, so it underpredicts the maximum burning rate for the same reasons. A better temporal estimate of the maximum burning rate could be obtained by modelling the temperature rise in the

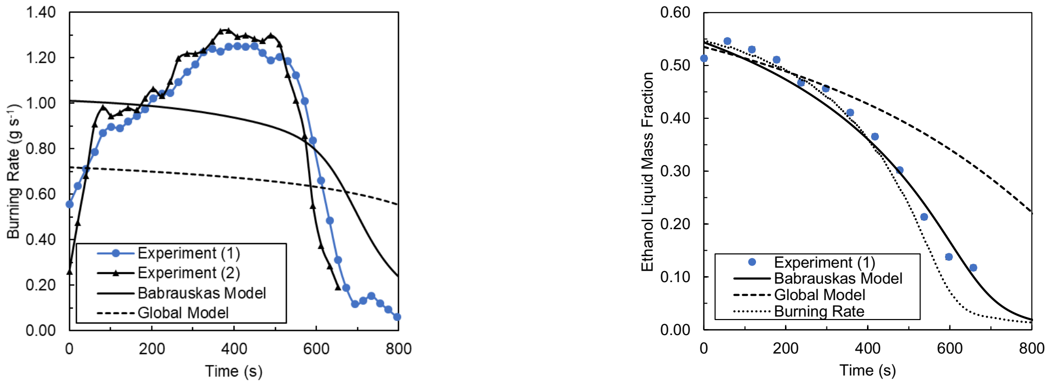

(a) 51-49% w/w Ethanol-Water (b) 51-49% w/w Ethanol-Water

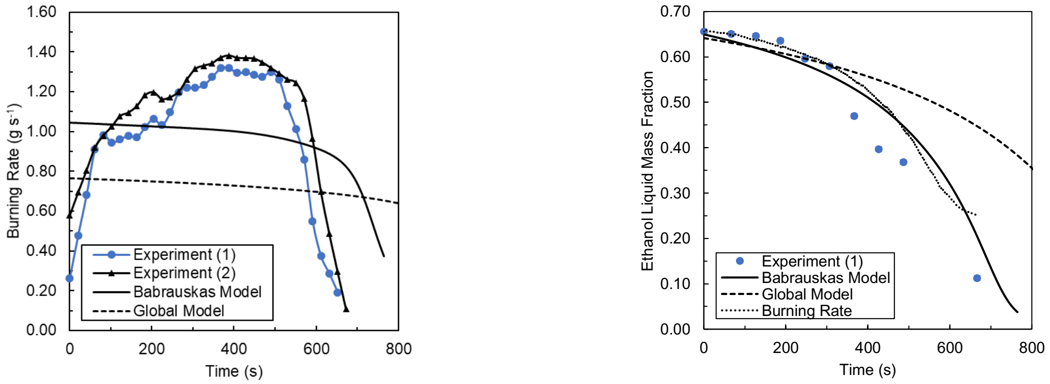

(c) 66-34% w/w Ethanol-Water (d) 66-34% w/w Ethanol-Water

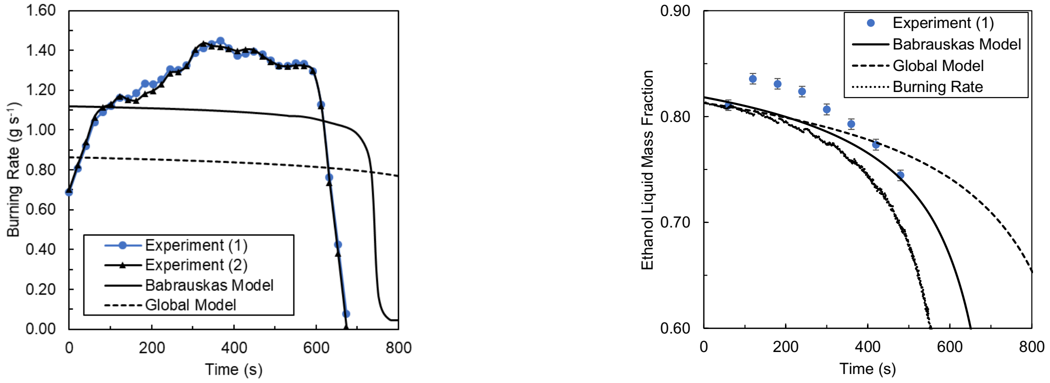

(e) 81-19% w/w Ethanol-Water (f) 81-19% w/w Ethanol-Water

Figure 4.1: Temporal variation of burning rates (left) and liquid composition (right) during batch ethanol-water pool fires. Balance accuracy is ±0.01 g. Error bars indicate measurement error from the FTIR spectrometer.

liquid phase over time. ΔH_g in Eq. (4.12) would be replaced by ΔH_v when the entire pool reaches the bubble-point. Bulk boiling is not unique to multicomponent fuels, so heuristics and model developments to account for this phenomena should be investigated first in single-component pool fires.

The comparison between experimental and modelled burning rates highlights the difficulty of validating a burning rate model using a batch pool fire. There are many transient effects present in a batch pool fire that the current models do not account for, such as fire growth, heating in the liquid, bulk boiling, rim effects, and extinction. Thus, the current methodology is mostly applicable to a pool that is near its boiling point and when the fire is fully grown. More meaningful comparisons are possible in a continuously fed pool fire, which are discussed in Section 4.4.2.

The fuel composition curves in Figure 4.1 serve to validate the distillation model proposed in Section 4.1. Predicted distillation from the experimental burning rate curves followed a similar trend to the concentration measurements, which supports the assumption of a well-mixed liquid phase for shallow pools. However, this may not be the case for deeper pools. Evaporation requires mass transport to the pool surface, which creates a concentration gradient if the entire pool is not well-mixed. It has been shown that only the upper layer of a deep pool has mixing from convection cells (Vali et al., 2015), so the assumption of a well-mixed liquid phase may only be adequate as an approximation for shallow pools. A detailed solution to the species profile within the pool would be necessary to predict the mass transfer resistance in the liquid. This would be an interesting theoretical exercise to determine the extent to which the condensed phase model influences the gas phase dynamics.

In Figures 4.1b and 4.1f, the measured ethanol concentration was higher than before ignition. The higher concentration measurements could be the result of local distillation within the draw tube. Partial immersion of the draw tube within the flame likely caused evaporation of liquid samples within the tube. The vapours have a higher ethanol concentration than the liquid, so vapour condensation within the tube would increase the ethanol concentration in the samples. In instances where the ethanol concentration measurements are below the predicted value (see Figure 4.1d), it is possible that part of the sample evaporated between the time the sample was taken and measuring the concentration. This argument is supported by observing that the samples taken in the latter half of the experiment time were generally boiling. The vials were also not completely filled and the sample size was particularly small at times when the liquid was boiling, which increases the size of the head space for the vapours to fill before reaching equilibrium.

Predicted trends in concentration appear to be more accurate than the predicted burning rate trends. This is because of the transport phenomena in the gas and liquid phase differ significantly. The composition in the liquid phase is governed by mass transfer, VLE, and mixing in the pool. Mass transport can be adequately described from first principles, and VLE and solution thermodynamics is a well-studied topic. Mixing in the pool requires a detailed fluid dynamics model, but the results in Figure 4.1 demonstrate that a well-mixed model gives reasonable predictions of distillation. Under the assumption of a well-mixed liquid phase, the general shape that the concentration curve takes is governed by VLE, and the burning rate merely determines how quickly the liquid is distilled. On the other hand, the burning rate is dependent on heat feedback from the flame to the pool surface, which is governed by complex processes like fluid dynamics, turbulent mixing, combustion chemistry, and radiation. The additional effect heat transfer in the liquid phase has on the burning rate further complicates burning behaviour.

4.4.2 Continuous Pool Fires

Steady-state burning rates for each mixture are presented in Figures 4.2 through 4.4. It should be noted that the steady-state composition of the fuel in Table 3.2 were used to obtain the corresponding vapour compositions in these plots, and they were also used to estimate heat release rates. This is an important detail in the methodology for treating multicomponent mixtures because the ethanol composition data in Table 3.2 shows that distillation still occurs even though the pool is continuously fed. Based on a mass balance around the pool, it is expected that distillation becomes more prevalent if the pool is fed at a slower rate. Higher amounts of distillation occurred in mixtures that had a large relative volatility (ethanol-hexane), while the least amount of distillation occurred in mixtures with a low relative volatility (ethanol-isopropanol). This finding is significant because based on the results of Eddings et al. (2005), it has generally been assumed that the composition of the fuel will not change if it is continuously supplied with fresh feed. However, this is only the case for mixtures that are mainly composed of species with similar volatilities.

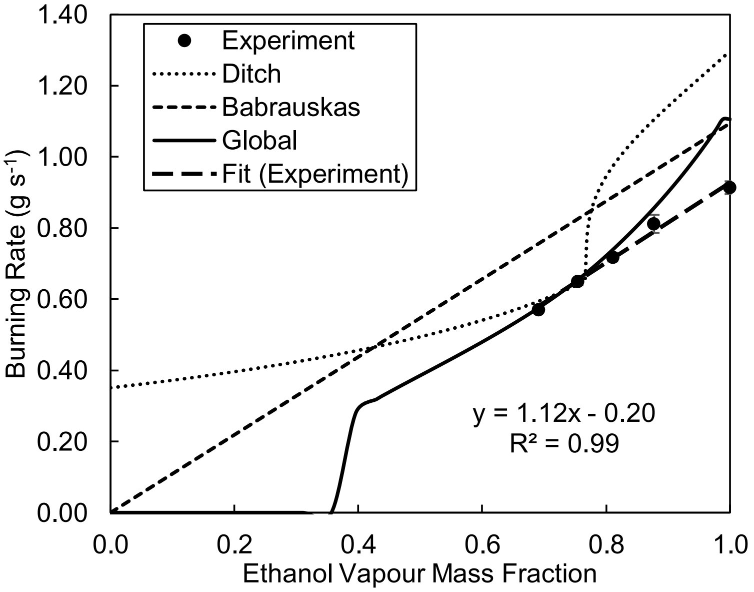

Figure 4.2: Maximum burning rate predictions for continuously fed ethanol-water pool fires in a 0.30 m diameter pan. Balance error accuracy is ±0.1 g. Error bars show one standard deviation of the time-averaged burning rate.

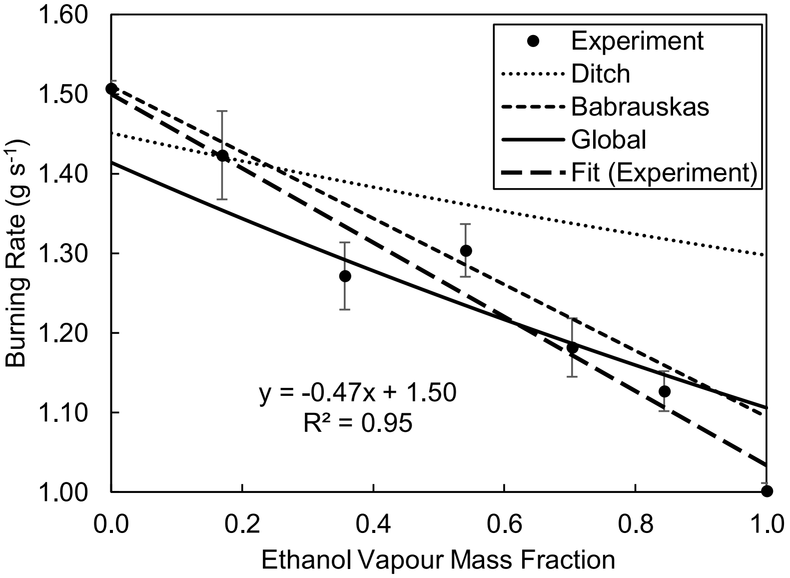

Figure 4.3: Maximum burning rate predictions for continuously fed ethanol-isopropanol pool fires in a 0.30 m diameter pan. Balance error accuracy is ±0.1 g. Error bars show one standard deviation of the time-averaged burning rate.

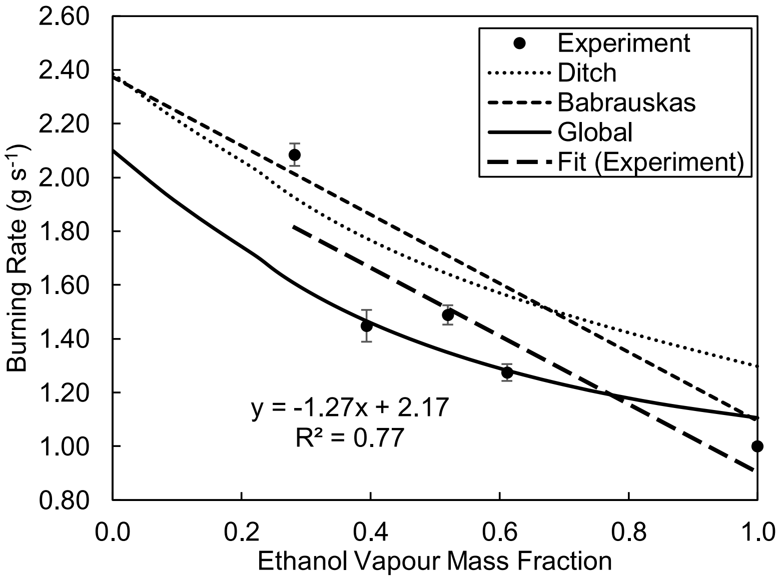

Figure 4.4: Maximum burning rate predictions for continuously fed ethanol-hexane pool fires in a 0.30 m diameter pan. Balance error accuracy is ±0.1 g. Error bars show one standard deviation of the time-averaged burning rate.

In general, the measured burning rates for all mixtures were consistently lower than predictions from Ditch et al.'s (2013) model, but this is expected because the pool was fed faster than the burning rate with room temperature fuel, which sub-cools the pool. Based on an energy balance around the pool, it is estimated that the sensible heat needed to heat the feed in the ethanol-water experiments reduces the burning rate by about 10-15%. This error could be minimized by feeding the pool at the same rate as it burns, but this would not allow for accurate sampling of the surface composition. In the experiments of Ditch et al. (2013), the pool was fed almost exactly at the burning rate, so their correlation was fit to pool fires with less sub-cooling from the feed and therefore higher burning rates.

The global model overpredicts the burning rate of pure ethanol because the burning rate was tuned to the global model predictions from Hamins et al. (1999), which were fit to experiments performed under different conditions compared to the present work (*e.g.* pan material, rim thickness, liquid level, feed rate, feed control). The correlation of Babrauskas (1983) gives an error of ±0.1 $\mathrm{g\,s^{-1}}$ for steady-state burning rates of pure ethanol in a 0.30 m diameter pan, and the burning rate for pure ethanol in Figures 4.3 and 4.4 fall within this range. If the pool were fed at a similar rate to the burning rate, the burning rate measurements for pure fuels would be closer to those predicted by the global model.

For all the mixtures that could be ignited at room temperature, burning rates for ethanol-water mixtures varied linearly with vapour composition. This suggests that the presence of water reduces the burning rate primarily by replacing combusting vapours with an inert gas. The rate of change between burning rate and vapour composition for ethanol-water was predicted well by all the models tested. However, the correlation of Ditch et al. (2013) predicted that presence of water should have a more pronounced effect near a 0.8 ethanol vapour mass fraction. Additionally, the correlation of Ditch et al. (2013) predicts unrealistic burning behaviour at low ethanol concentrations because it was not fit to fuels containing an inert component.

Since the relationship between liquid and vapour compositions in ethanol-water mixtures is approximately linear between $x_{EtOH} = 0.3$ to 1.0, the burning rate could also be correlated linearly with the liquid composition, which is useful for making quick engineering calculations. It is also important to note that the models in Figure 4.2 give the maximum burning rates assuming ignition has already occurred. Flammability of aqueous solutions can be predicted by estimating the vapour pressure of each component and determining whether the vapour mixture is within its flammability limits (Brooks & Crowl, 2007).

Burning rates for ethanol-isopropanol mixtures varied linearly with the vapour composition. This result agrees with Grumer et al. (1961), who reported that averaging pure component burning rates based on the vapour composition is appropriate for blended fuels containing species with similar chemical properties and vapour compositions close to the liquid composition. Ethanol-isopropanol is an example of an ideal mixture with a low relative volatility, which ranges from 1.16 to 1.20 over the entire composition range. It can be extrapolated from the burning rate data in Figure 4.3 that for ideal mixtures with low relative volatilities, the burning rate can be approximated as the vapour mass-average of pure component burning rates.

Burning behaviour for a non-ideal solution containing two flammable components is illustrated by the ethanol-hexane mixtures. For these mixtures, small changes in liquid composition at high ethanol concentrations had a great effect on the vapour composition. An 8% w/w change in the liquid composition (95.8% to 87.8% w/w ethanol) resulted in a 13% difference in burning rate and 32% difference in flame height (Figure 4.5). These effects caused by VLE are significant because small changes in the composition of hexane will have a larger impact on the fire dynamics. The data presented in Figure 4.4 shows that the variation in burning rate with vapour composition can be roughly approximated as linear. However, it is recommended to use empirical burning rate correlations that rely on the properties of the fuel to capture any potential nonlinear effects. Both Ditch et al.'s (2013) model and the global model predict similar variations in burning rate with vapour composition for ethanol-hexane mixtures. This is because $\dot{m} \propto \Delta H_c / \Delta H_g$, where heats of combustion and vaporization are mostly dependent on the vapour composition. The heat of gasification of each pure component varies with temperature, causing ΔH_g to vary nonlinearly with vapour composition.

For mixtures containing only flammable components, the global model and Ditch et al's (2013) model predict similar relationships between burning rate and vapour composition. The main difference between the models is their prediction of pure component burning rates. Since the global model couples evaporation with the heat feedback from the flame, it has the capability to estimate a limiting mass fraction for which a fire cannot be sustained. Based on the final ethanol concentrations in Figures 4.1b and 4.1d, the limiting concentration in a 0.30 m pan is around 11% ethanol by mass, which corresponds to approximately 53% w/w ethanol vapour. Meanwhile, the extinction limit predicted by the global model in Figure 4.2 is 40% w/w ethanol vapour. The model does not account for rim effects and heat losses from conduction, so it is likely that neglecting these factors enables sustained burning with a more dilute fuel. Since the global model has the capability of estimating extinction, it would be most appropriate in any scenario involving an aqueous flammable mixture.

Figure 4.5 shows a linear fit to the mean flame height measurements, which is given as follows:

$$\frac{H}{D} = -0.90 + 3.47\dot{Q}^{*2/5} \tag{4.29}$$

For the range of HRRs tested, the mean flame heights tend to be lower than those predicted by Heskestad's correlation. This may be caused by the flame regularly tilting due to uneven air entrainment into the fire. The fitted dependence on $\dot{Q}^{*2/5}$ is

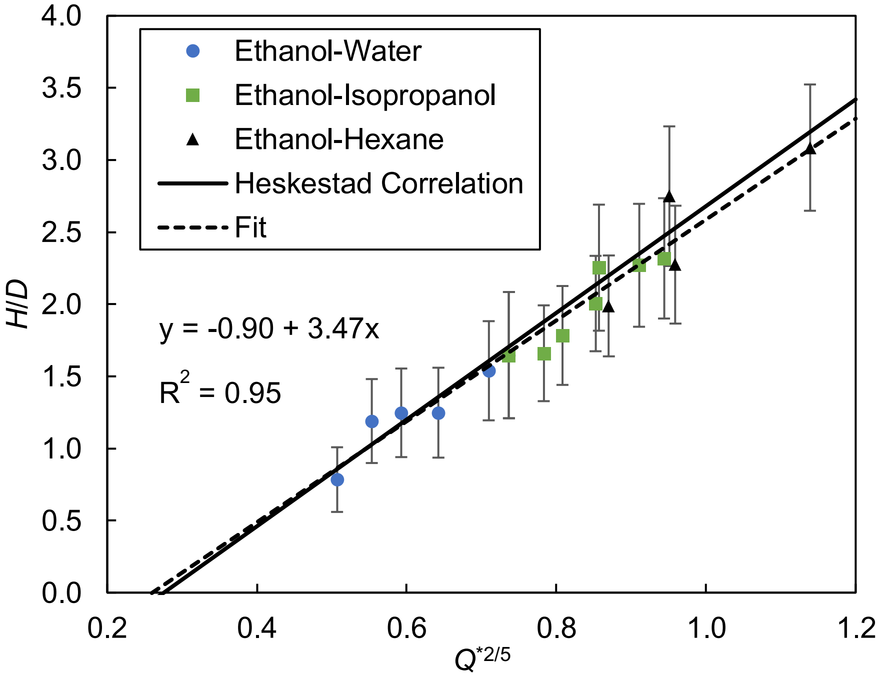

Figure 4.5: Mean flame heights from steady-state pool fire experiments. Error bars indicate one standard deviation of the instantaneous visible flame height over the time-averaging period.

not significantly different from the value given by Heskestad's correlation. The spread in the data set used to fit Heskestad's flame height correlation is reasonably large (see Appendix H), so it is likely that the difference between the fit obtained for the present measurements and Heskestad's flame height correlation is insignificant. Thus, it is concluded that Heskestad's flame height correlation gives adequate predictions for flame heights of the fuel blends tested. Since the steady-state composition of the fuel surface was used to estimate HRR, the only uncertainty about the present flame height measurements are the errors associated with video processing and the concentration measurement.

In Figure 4.6, the magnitude in temperature standard deviations shows that there are more temperature fluctuations near the base of the flame than further up in the plume. A higher degree of temperature fluctuation occurs near the base because the gases combust locally in "sheets". As a result, the thermocouples are not always immersed in the flame. The temperature loss to the surroundings is greater when the thermocouple is hotter, which causes the temperature reading to have larger fluctuations. All other flame temperature measurements that are not radiation-corrected

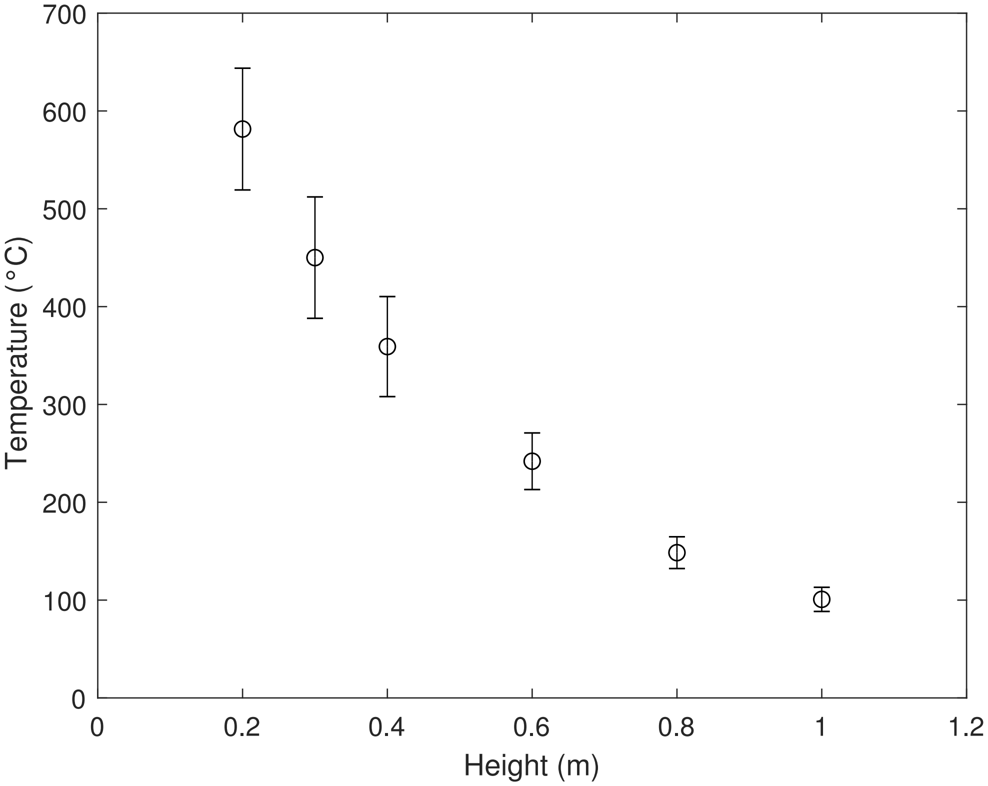

Figure 4.6: Time-averaged flame temperature measurements for a continuously fed 50-50% w/w ethanol-isopropanol pool fire. Temperatures are not radiation-corrected. Error bars indicate one standard deviation over the time-averaging interval.

are presented in Appendix D.

Figure 4.7 shows the fit to the flame temperature measurements, which is given as follows:

$$\Delta T = 14.21\dot{Q}_c^{0.62}(z - z_0)^{-1.56} \tag{4.30}$$

The dependence of temperature on height and convective HRR in Eq. (4.30) is very similar to the proportionality given by Heskestad's flame temperature correlation ($\Delta T \propto \dot{Q}_c^{2/3}(z - z_0)^{-5/3}$). However, the average temperature measurements are generally underestimated in comparison to Heskestad's correlation. This is due to forced ventilation in the room causing the flame to frequently wander outside of the centre of the apparatus. It was observed in the video recordings that pure ethanol and isopropanol flames did not frequently wander outside the centerline of the pan, while flames for the ethanol-isopropanol mixtures would tilt on a regular basis. The data

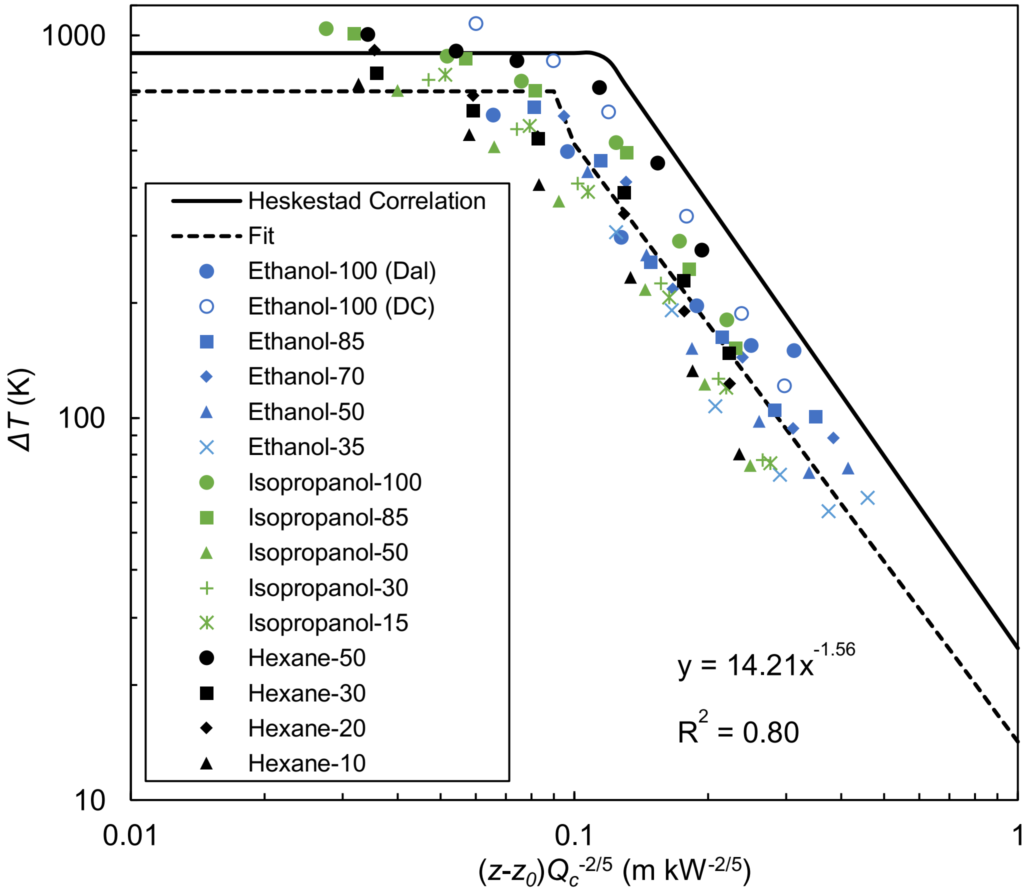

Figure 4.7: Radiation-corrected centerline flame temperature measurements from steady-state pool fire experiments for ethanol-water, ethanol-isopropanol, and ethanol-hexane blends.

may also be slightly skewed to the left because the HRR was extrapolated from the theoretical maximum HRR (Eq. (4.9)), which results in a slight overestimation of the actual HRR. It is recommended for future work on flame temperature measurements to put a mesh screen around the apparatus to reduce the effects of unsymmetrical air currents on tilting the flame if there is forced ventilation in the room.

Assuming the radiant fraction to be linearly proportional to the vapour composition could be causing the abscissa for ethanol-hexane mixtures to be over-shifted to the left. It is well-known that blending ethanol with hydrocarbons reduces soot emissions (Esarte et al., 2009), which consequentially reduces heat losses from radiation. Given that the radiant fraction is required to estimate radiative heat transfer to objects outside the flame, it is recommended in future work to determine the effect of fuel composition on radiant fraction. Since most of the flame temperature data follows the expected trend, it is reasonable to conclude that Heskestad's flame temperature correlation gives adequate estimates for flame temperatures of binary fuel blends.

4.5 General Discussion

The modelling approaches that were presented in this chapter underpredicted maximum burning rates in batch ethanol-water pool fires because they do not account for the burning rate enhancement that occurs with bulk boiling. This is not an issue that is unique to multicomponent pool fires. Bulk boiling occurs when the fire has achieved steady-state burning conditions (Chatris et al., 2001), which typically occurs when the fuel layer becomes thin for pools starting at room temperature (Chen, Lu, Li, Kang, & Yuan, 2012). Thus, the models will be most applicable to two batch fire scenarios. One is where the pool is too shallow to heat up to the boiling point. The other is when the pool is very deep and the bulk of the fuel will remain below the boiling point until the pool reaches a layer thickness on the order of a few cm. Heuristics to anticipate occurrence of bulk boiling are currently unavailable, so it may be of interest to perform deep, batch pool fire experiments with several types of fuels to relate fuel layer thickness with the occurrence of boiling. Hayasaka (1997) provides ratios of steady burning rates observed in boiling and non-boiling pool fires, which may be useful to incorporate as an empirical heuristic in burning rate models applied to batch pool fire scenarios.

Measurement of steady-state liquid composition enabled accurate determination of the effect of fuel composition on burning rates, flame heights, and flame temperatures in binary mixtures with varying degrees of thermodynamic ideality in solution. It was found that for an ideal mixture with a relative volatility close to one, a vapour mass-average of pure burning rates provided sufficient estimates of the steady-state burning rate. Validating this for ideal mixtures with higher relative volatilities (*e.g.* benzene-toluene, methanol-isopropanol) requires further experimental validation, but both Ditch et al.'s (2013) model and the global model can give preliminary results about the expected relationship between mixture ratio and burning rate.

In aqueous flammable mixtures, the presence of water simply reduced the amount of flammable vapours available, so the reduction in burning rate was linearly proportional to the vapour mass fraction of flammable vapours. The correlation of Ditch et al. (2013) should be used cautiously with aqueous flammable solutions because it was only fit to fuels containing no inert species. For solutions with a large range of relative volatilities (non-ideal) where all species are flammable, burning rate models dependent on the properties of each fuel are recommended since they are capable of predicting nonlinear relationships between vapour composition and burning rate.

Although this work investigated combustion behaviour only in binary fuels, the models may be applied in the same way to multicomponent fuels with more than two components. Furthermore, it is arguable that classifying combustion behaviour based on relative volatility is applicable to multicomponent mixtures in general. It was shown that burning rates in binary fuels were primarily dependent on the vapour composition, and flame heights and flame temperatures were only dependent on HRR, which is also a function of vapour composition (Eq. (4.9)). Assuming these observations apply to mixtures with more than two components, combustion behaviour in multicomponent pool fires will be predictable if the vapour composition is known. The recommended method to anticipate the progression of combustion behaviour caused by distillation in multicomponent fuels is using a batch distillation model.

It was demonstrated that the surface composition of a continuously fed multicomponent pool fire does not necessarily remain constant. For mixtures with a low relative volatility, the error associated with assuming the composition remains similar to the feed will be small. For mixtures with a high relative volatility, the error associated with this assumption increases, so it is recommended to check the sensitivity of the burning rate to the liquid composition.

Estimates of the steady-state composition can be made by solving a mass balance around the pool. Although results from the batch pool fires showed that assuming the liquid as well-mixed yielded reasonable predictions of the surface composition, mixing in liquid pool fires is known to fall somewhere between well-mixed and diffusion limited. Therefore, assumption of a well-mixed liquid phase will result in underestimating the concentration of less volatile components (Eddings et al., 2005). It is recommended to develop a mixing model that falls somewhere in between well-mixed and diffusion limited. An initial development could be to divide the liquid into an upper layer that is well-mixed, and a lower layer that is diffusion-limited. Methods for estimating these layer thicknesses have not been developed yet, but work from Vali et al. (2015) may be used as a guideline.

Heskestad's flame height and flame temperature correlations gave acceptable predictions when compared to the measurements. These correlations are appropriate for use with multicomponent fuels as long as the vapour composition is known. For a batch pool fire, the composition of the pool can be monitored using the distillation model presented in Section 4.1. If the pool is continuously fed, a rough estimate of the steady-state composition can be obtained by performing a mass balance around the pool as in Appendix B.

Methods for estimating properties like sooting propensity, radiation fraction, and combustion efficiency are lacking, and these properties are required for applying detailed burning rate models like the global model to multicomponent fuels. Mixing rules based on threshold sooting index exist for estimating smoke points in hydrocarbon mixtures (Gill & Olson, 1984), but linear blending rules for sooting propensity in hydrocarbon-oxygenate blends are known to not apply as the oxygenating chemical group reduces formation of soot (Armas, Gómez, Barrientos, & Boehman, 2011; Ditch et al., 2013; Esarte et al., 2009). Given that radiation losses are dependent on the sooting propensity of the flame and that combustion efficiency is determined by the extent to which complete combustion is achieved, it is unlikely that linear mixing rules for these properties in hydrocarbon-oxygenate blends will apply. Further investigation of how these properties vary with composition in multicomponent fuels is recommended.

Chapter 5

Fire Dynamics Simulator

Fire Dynamics Simulator (FDS) is an open-source, Fortran-based CFD code that solves fluid dynamics in fire-driven flows. As discussed in Section 2.5.2, FDS currently has limited capabilities for predictive modelling of multicomponent pool fires. The liquid pyrolysis model cannot account for multiple evaporating species, vapour-liquid equilibrium (VLE) models are unavailable, and each liquid cell is treated as its own separate control volume (no mixing in the liquid phase). In this work, models have been added to FDS version 6.7.1 to resolve the above issues. Predictions made using the new models have been validated against experimental data from the present work, Y. Ding et al. (2014), and well-known empirical correlations.

5.1 Numerical Models

This section outlines the governing equations and models used in FDS. A more detailed description of the models employed is provided the FDS Technical Reference Guide (McGrattan, McDermott, et al., 2019).

5.1.1 Gas Phase Equations

FDS solves the low Mach number formulation of the Navier-Stokes equations (Rehm & Baum, 1978) using the large eddy simulation technique to model turbulence. The low Mach number approximation defines pressure as a combination of background ($\bar{P}$) and perturbation ($\tilde{P}$) pressures (Pa). The background pressure is given by the ideal gas law:

$$\bar{P} = \frac{\rho R_g T}{W} \tag{5.1}$$

where ρ is density ($\mathrm{kg\,m^{-3}}$), R_g is the universal gas constant ($\mathrm{J\,mol^{-1}\,K^{-1}}$), T is temperature (K), and W is molecular weight ($\mathrm{kg\,mol^{-1}}$). The momentum equation is then expressed as follows (McGrattan, McDermott, et al., 2019):

$$\frac{\partial \mathbf{u}}{\partial t} - \underbrace{\mathbf{u} \times \omega - \frac{1}{\rho}\left[(\rho - \rho_\infty)\mathbf{g} + \nabla \cdot \tau\right]}_{\text{Advective}} + \nabla H_p - \underbrace{\tilde{P} \nabla \frac{1}{\rho}}_{\text{Baroclinic}} = 0 \tag{5.2}$$

$$H_p = \frac{|\mathbf{u}^2|}{2} + \frac{\tilde{P}}{\rho} \tag{5.3}$$

where $\mathbf{u}$ is velocity ($\mathrm{m\,s^{-1}}$), ω is vorticity ($\mathrm{s^{-1}}$), $\tilde{P}$ is the perturbation pressure (Pa), $\mathbf{g}$ is gravitational acceleration ($\mathrm{m\,s^{-2}}$), H_p is the total pressure divided by the fluid density ($\mathrm{m^2\,s^{-2}}$), and τ is the viscous stress tensor (Pa). The default turbulence model in FDS that is used to close the viscous stress tensor is the Deardorff turbulence model (Deardorff, 1980). Other turbulence models such as the constant coefficient Smagorinsky model (Smagorinsky, 1963) and the dynamic Smagorinsky model (Germano, Piomelli, Moin, & Cabot, 1991) are also available. The conservation equations for mass, species, and energy are as follows (McGrattan, McDermott, et al., 2019):

$$\frac{\partial \rho}{\partial t} + \nabla \cdot (\rho \mathbf{u}) = 0 \tag{5.4}$$

$$\frac{\partial (\rho y_i)}{\partial t} + \nabla \cdot \rho y_i \mathbf{u} = \nabla \cdot (\rho D_g)_i \nabla y_i + \dot{m}''' \tag{5.5}$$

$$\frac{\partial (\rho h_s)}{\partial t} + \nabla \cdot (\rho h_s \mathbf{u}) = \frac{\partial \bar{P}}{\partial t} + \mathbf{u} \cdot \nabla \bar{P} + \dot{Q}''' - \nabla \cdot \dot{\mathbf{Q}}'' \tag{5.6}$$

where $\dot{Q}'''$ is the volumetric heat generation rate from chemical reactions ($\mathrm{W\,m^{-3}}$), $\dot{m}'''$ is the volumetric mass generation rate ($\mathrm{kg\,m^{-3}\,s^{-1}}$), D_g is mass diffusivity ($\mathrm{m^2\,s^{-1}}$), h_s is specific enthalpy ($\mathrm{J\,kg^{-1}}$), and $\dot{\mathbf{Q}}''$ is the sum of conductive, diffusive, and radiative heat fluxes ($\mathrm{W\,m^{-2}}$):

$$\dot{\mathbf{Q}}'' = -k \nabla T - \sum_i h_{s,i} \rho D_i \nabla Z_i + \dot{\mathbf{Q}}''_r \tag{5.7}$$

where k is thermal conductivity ($\mathrm{W\,m^{-1}\,K^{-1}}$) and Z_i is the mixture fraction of species i. The conservation equations are solved simultaneously for velocity, temperature, pressure, and mixture fraction at a given time step using an explicit second-order predictor/corrector scheme. The pressure and momentum equations are coupled through an iterative procedure. First, the advective and baroclinic terms of the momentum equation are computed. Then, the pressure equation is solved multiple times until the normal component of velocity and background pressure converge to a specified tolerance. The velocity field is then re-computed for the next time step. This procedure is iterated until both velocity and pressure converge to a specified tolerance (McGrattan, McDermott, et al., 2019).

5.1.2 Radiation

In Eq. (5.6), the radiative portion of the net heat flux is calculated using the following equation:

$$-\nabla\cdot\dot{\mathbf{Q}}'' = \kappa[U - 4\pi I_b(\mathbf{x})] \quad ; \quad U = \int_{4\pi} I(\mathbf{x},\mathbf{s})\,d\mathbf{s} \tag{5.8}$$

where $I(\mathbf{x},\mathbf{s})$ is the total radiative intensity ($\mathrm{W\,sr^{-1}}$) at location $\mathbf{x}$ (m) in direction $\mathbf{s}$, $I_b(\mathbf{x})$ is the source term ($\mathrm{W\,m^{-2}}$), U is the integrated radiative intensity ($\mathrm{W\,m^{-2}}$), and κ is the absorption coefficient ($\mathrm{m^{-1}}$), which is calculated from the RadCal narrowband model (Grosshandler, 1993). RadCal calculates spectral properties of radiating gas species at discrete wavelength bands where the species actively absorb radiation. The total intensity is found by solving the radiative transport equation (RTE). For the pool fire scenarios investigated in the present study, it is assumed that there are no droplets or particles to absorb and scatter radiation, so the RTE is solved for a non-scattering gray gas:

$$\mathbf{s}\cdot\nabla I(\mathbf{x},\mathbf{s}) = \kappa[I_b(\mathbf{x}) - I(\mathbf{x},\mathbf{s})] \tag{5.9}$$

The contribution of soot to radiative transport is accounted for by keeping track of the soot species fraction in each cell. The RadCal model for each fuel then takes into consideration the soot concentration when calculating the absorption coefficient. The source term ($I_b(\mathbf{x})$) is given as the blackbody radiation generated from the gas. A correction factor is applied within the flame zone since the temperature of the flame sheet cannot be resolved with cells with a width of centimeters:

$$I_b(\mathbf{x}) = C\frac{\sigma T^4}{\pi} \quad ; \quad C = \min\left[100, \max\left(1, \frac{\int_{\dot{Q}'''} \chi_r \dot{Q}''' + \kappa U \, dV}{\int_{\dot{Q}'''} 4\sigma\kappa T^4 \, dV}\right)\right] \tag{5.10}$$

C is 1 outside of the flame and 1-100 inside the flaming zone.

5.1.3 Combustion

The default combustion scheme of FDS was used for all simulations. This scheme treats combustion as an irreversible single-step infinitely fast reaction:

$$Fuel + Oxidizer \longrightarrow Products \tag{5.11}$$

The products of combustion are CO_2, CO, soot, and water vapour. The volumetric heat release rate in a cell is given by the following equation:

$$\dot{Q}''' = \dot{m}'''\Delta H_c \tag{5.12}$$

where $\dot{m}'''$ is the fuel combustion rate ($\mathrm{kg\,m^{-3}\,s^{-1}}$) within the given control volume. The Eddy Dissipation Concept (EDC) model (Magnussen & Hjertager, 1977; Magnussen, 2005) is used to model turbulent combustion. For a single-step infinitely-fast chemical reaction, the fuel and oxidizer react once they are completely mixed:

$$\dot{m}''' = -\rho\frac{\min(y_f, y_a/r)}{\tau_{mix}} \tag{5.13}$$

where r is the stoichiometric air-to-fuel mass ratio, y_f and y_a are the mass fractions of fuel and air in the cell, and τ_{mix} is the mixing time scale (s), which is equal to the fastest time scale of diffusion, sub-grid scale advection, or buoyant acceleration (McDermott, McGrattan, & Floyd, 2011; McGrattan, McDermott, et al., 2019). The mixing time scale is defined as follows:

$$\tau_{mix} = \max(\tau_{chem}, \min(\tau_d, \tau_u, \tau_g, \tau_{flame})) \tag{5.14}$$

$$\tau_d = \frac{\Delta^2}{D_{fuel}} \tag{5.15}$$

$$\tau_u = \frac{C_u \Delta}{\sqrt{(2/3) k_{sgs}}} \tag{5.16}$$

$$\tau_g = \sqrt{2\Delta/g} \tag{5.17}$$

where τ_d, τ_u, and τ_g are the mixing time scales for diffusion, advection, and acceleration (s), D_{fuel} is the mass diffusivity of the fuel ($\mathrm{m^2\,s^{-1}}$), Δ is the LES filter width (m), C_u is an advective time scale constant that is set to 0.4 by default, and k_{sgs} is the sub-grid turbulent kinetic energy ($\mathrm{m^2\,s^{-2}}$). τ_{chem} and τ_{flame} are by default 10^{-4} and 1 s, respectively. The filter width is given by the following equation:

$$\Delta = V_{cell}^{1/3} \tag{5.18}$$

where V_{cell} is the volume of the computational cell ($\mathrm{m^3}$).

5.1.4 Condensed Phase Model

FDS treats liquids as thermally-thick solids. The temperature gradient of the pool is normally found by solving the one-dimensional heat conduction equation:

$$\rho c_p \frac{\partial T}{\partial t} = \frac{\partial}{\partial z}\left(k \frac{\partial T}{\partial z}\right) + \dot{Q}''' \tag{5.19}$$

where c_p is specific heat capacity ($\mathrm{J\,kg^{-1}\,K^{-1}}$). The thermal properties k and ρc_p are mass-averaged in each cell. The volumetric source term ($\dot{Q}'''$) accounts for energy generated from chemical reactions, phase change, and in-depth radiation absorption. The default evaporation model in FDS is based on Stefan-diffusion of a single species:

$$\dot{m}'' = h_m \frac{PW}{RT_g} \ln\left(\frac{y_{f,s} - 1}{y_{sat} - 1}\right); \quad h_m = \frac{Sh D_g}{L} \tag{2.20}$$

where $\dot{m}''$ is mass flux ($\mathrm{kg\,m^{-2}\,s^{-1}}$), h_m is the convective mass transfer coefficient ($\mathrm{m\,s^{-1}}$), T_g is the gas temperature (K) in the cell adjacent to the fuel surface, y_{sat} is the equilibrium fraction of fuel vapour above the pool surface, Sh is the Sherwood number, and L is the characteristic dimension (m) of the fuel base.

In the present study, the pool was treated as well-mixed. The temperature of the pool was set to the bubble-point of the mixture and the composition in each cell was updated as described in Section 4.1. The heat of gasification was used in the surface energy balance instead of the heat of vaporization to account for the required energy to heat the liquid from room temperature to the bubble-point. The energy balance at the surface reduces to Eq. (4.12), which was implemented in the following manner:

$$\dot{m} = \frac{\dot{Q}_c + \dot{Q}_r - \dot{Q}_{rr}}{\sum_{i=1}^{N} y_i \Delta H_{v_i} + \sum_{i=1}^{N} x_i c_{p_i} (T_b - T_0)} \tag{5.20}$$

where $\dot{Q}_c$, $\dot{Q}_r$, and $\dot{Q}_{rr}$ are heat transfer rates (W) to the pool surface by convection, radiation, and reradiation, ΔH_v is heat of vaporization ($\mathrm{J\,kg^{-1}}$), x_i and y_i are the equilibrium liquid and vapour mass fractions at the pool surface, T_b is the bubble-point temperature of the mixture (K), and T_0 is the initial temperature of the mixture (K), which is set to ambient temperature by default.

Since FDS treats the liquid as a thermally-thick solid, an algorithm was developed to calculate the average composition of the pool and set the composition of each cell to that value at the end of each time step. Bubble-point temperatures and equilibrium vapour compositions for each mixture were defined using polynomials that were fit to the Wilson model. The polynomials and constants are listed in Appendix A.

5.2 Thermocouple Model

The FDS thermocouple model was used to compare the calculated temperature field in FDS to experimental data that was not temperature-corrected. This enables the simulation to account for the thermal mass of the thermocouple and radiation heat losses. The thermocouple temperature (T_{TC}) is found by solving the energy balance around the thermocouple:

$$\rho c_p \frac{dT_{TC}}{dt} = \varepsilon (U/4 - \sigma T_{TC}^4) + h(T_g - T_{TC}) \tag{5.21}$$

where ε is the emissivity of the thermocouple, h is the convective heat transfer coefficient ($\mathrm{W\,m^{-2}\,K^{-1}}$), and T_g is the actual gas temperature (K). The bead diameter was set equal to the size of the thermocouples used for gas temperature measurements in experiments from the present work (Chapter 3) and of Y. Ding et al. (2014), which were all 1 mm. Since all thermocouples were K-type, density and heat capacity were set to those of nickel: $\rho = 8909\,\mathrm{kg\,m^{-3}}$ and $c_p = 0.44\,\mathrm{kJ\,kg^{-1}\,K^{-1}}$. The emissivity was set to 0.9 as in Brohez, Delvosalle, and Marlair (2004) and the FDS Validation Guide (McGrattan, Hostikka, McDermott, Floyd, & Vanella, 2019).

5.3 Flame Height

The mean flame height was measured using the same methodology as in the FDS Validation Guide (McGrattan, Hostikka, et al., 2019), where the flame height is defined as the distance above the fuel where 99% of the fuel has been burned. This definition is arbitrary, but it has been verified that between 95% and 99%, the maximum difference between the flame height and the mean flame height predicted by Heskestad's flame height correlation was ±15% when $\dot{Q}^* > 1$. The uncertainty increases to ±65% when $\dot{Q}^* = 0.1$. For pure ethanol, isopropanol, and hexane in a 0.30 m diameter pan, $\dot{Q}^*$ is approximately 0.6, 1.0, and 1.9, respectively. Since Heskestad's flame height correlation was fit to intermittency measurements of visible flame heights, the numerical definition of the flame height is expected to be similar to the visible flame height.

5.4 Case Studies

Since most pool fire scenarios are transient fires, the target objective is to apply the proposed condensed phase model in Section 5.1.4 to a transient, multicomponent pool fire scenario and verify that the fire dynamics will change accordingly with the fuel composition. This scenario requires coupling of both condensed phase and gas phase models. The gas phase models determine the flame height, flame temperature, and heat feedback to the pool surface. The condensed phase models use the heat feedback to the pool surface to predict the evaporation rate of the fuel. The models for each phase must be evaluated separately to identify the errors associated with each before implementing a full validation case.

The functionality of the condensed phase model was verified by modelling a multicomponent fuel evaporating with constant heat flux applied to the surface. The functionality of the gas phase model was evaluated for steady-state pool fires with a constant mass flux prescribed, where Heskestad's flame height and flame temperature correlations were used as benchmarks. Finally, full validation cases simulating transient pool fire experiments performed by Y. Ding et al. (2014) were run with optimized simulation settings used in the test cases. Their data set was selected over the ethanol-water pool fires described in Section 3.2 because transitions in combustion behaviour caused by distillation in their ethanol-heptane pool fires were more evident. This facilitated drawing conclusions the ability of FDS to predict changes in combustion behaviour caused by distillation.

Physical and thermal properties were set as constants. Latent heat of vaporization for each species was specified at the boiling point of the pure fuel. Unless stated otherwise, density and specific heat capacity of each fuel were specified at 25 °C. FDS default settings were used for the radiant fraction. Soot and CO yield were obtained from Tewarson (1984). These properties are listed in Table 5.1.

Table 5.1: Properties of Liquid Fuels Specified in FDS Case Studies

Fuel	ΔH_c (kJ kg^{-1})	ΔH_v (kJ kg^{-1})	c_p (kJ kg^{-1} K^{-1})	ρ (kg m^{-3})	T_b (°C)	χ_r	Y_s	Y_{CO}
Ethanol	26800	845	2.44	786	78.37	0.25	0.008	0.001
n-Heptane	44400	318	2.24	682	98.42	0.40	0.037	0.010
n-Hexane	41500	334	2.28	656	68.75	0.40	0.035	0.009
Isopropanol	33100	665	2.61	782	82.35	0.29	0.015	0.003
Water	0	2265	4.18	997	100.00	0	0	0

The dimensions of the computational domain were 0.9 × 0.9 × 2.0 m. The floor and sides of the pan were treated as adiabatic. All boundaries except the bottom were open to flow in and out of the domain. The bottom boundary was a wall with the no-slip condition applied.

The cell dimensions were chosen based on the rule of thumb that the plume resolution index, RI, should be greater than or equal to 10, meaning that the characteristic fire diameter, D^* (m), should span 10 cells or more (McGrattan, Baum, & Rehm, 1998):

$$RI = \frac{D^*}{\Delta x} \tag{5.22}$$

$$D^* = \left(\frac{\dot{Q}}{\rho_\infty c_{p\infty} T_\infty \sqrt{g}} \right)^{2/5} \tag{5.23}$$

where $\dot{Q}$ is the total HRR (W) and Δx is the cell width (m). A cell size of 20 × 20

× 20 mm satisfied this criteria for the pool fires that were simulated. Further mesh refinement was found to have an insignificant impact on predicted burning rates, flame temperatures, and flame heights.

5.4.1 Condensed Phase Model Verification

The condensed phase model was verified against a simple evaporating pool scenario that is solvable by hand using the same distillation methodology described in Section 4.1. To confirm the functionality of the condensed phase solver in FDS with the newly implemented VLE and mixing models, a 1 × 1 × 0.01 m pool of ethanol and hexane was exposed to a uniform external heat flux. The initial net heat flux was user-specified as $10\,\mathrm{kW\,m^{-2}}$. However, FDS uses this value to specify an external incident flux ($\dot{Q}''_{inc,r}$):

$$\dot{Q}''_{net} = \varepsilon_s(\dot{Q}''_{inc,r} - \sigma T_s^4) + h(T_g - T_s) \tag{5.24}$$

where ε_s is the surface emissivity, and T_s is the pool surface temperature (K). FDS uses the initial temperature of the surface and gas to calculate the incident heat flux to the surface. For $\varepsilon_s = 1$ and $T_g = T_s = 298.15\,\mathrm{K}$, the incident heat flux is $10.5\,\mathrm{kW\,m^{-2}}$. The composition of the fuel mixture was 50-50% w/w ethanol-hexane. Gas phase computations were disabled. The time step was set to 1 s. An equivalent MATLAB script that computed VLE and pool composition with the same methodology described in Section 4.1 was used to verify the predictions made by FDS. Figures 5.1-5.3 display the predictions of FDS and the MATLAB script. The instantaneous bubble-point temperatures and compositions correspond to those that would be seen on a $T - x - y$ VLE diagram for ethanol-hexane.

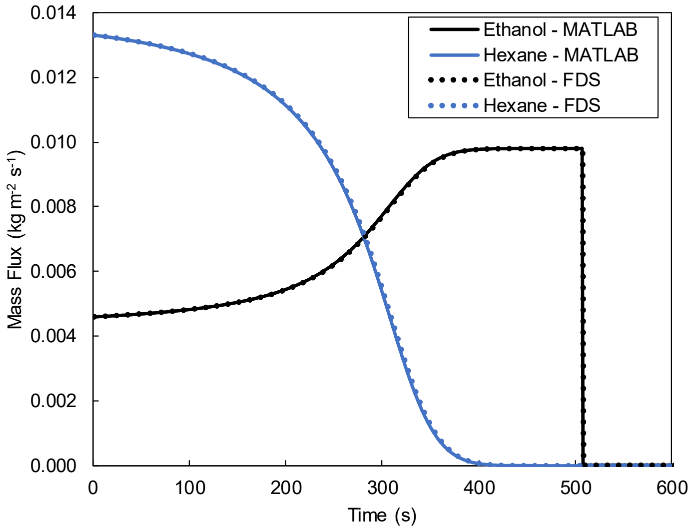

Figure 5.1: Comparison of mass flux predictions from FDS and MATLAB for an evaporating pool of ethanol and hexane with an incident heat flux of 10.5 kW m^{-2}.

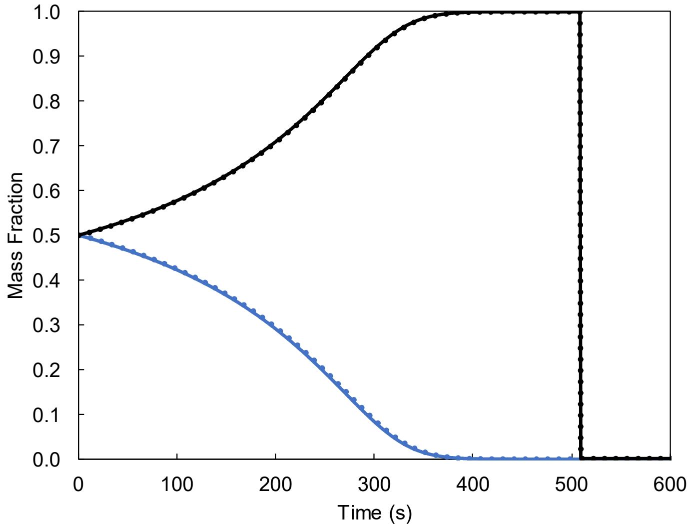

Figure 5.2: Comparison of liquid composition predictions from FDS and MATLAB for an evaporating pool of ethanol and hexane with an incident heat flux of 10.5 kW m^{-2}.

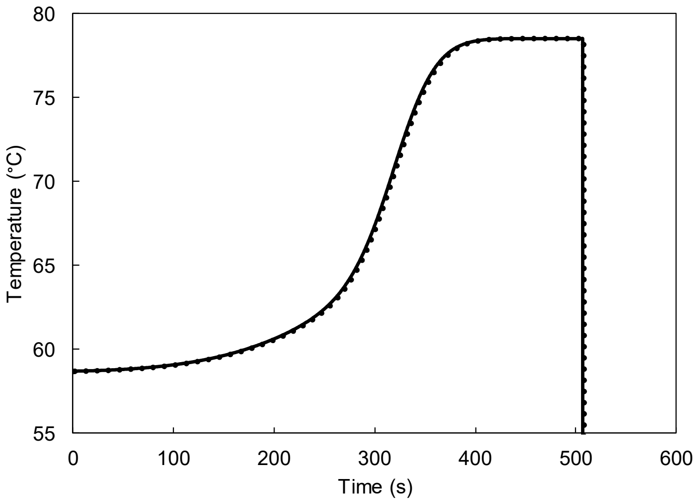

Figure 5.3: Comparison of liquid temperature predictions from FDS and MATLAB for an evaporating pool of ethanol and hexane with an incident heat flux of $10.5\,\mathrm{kW\,m^{-2}}$.

5.4.2 Gas-Phase Model Evaluation

To evaluate the predicted flame heights and flame temperatures in the absence of a pyrolysis model, the mass flux for each component was set to a constant value. The specified vapour composition and mass fluxes are given in Table 5.2. Mass fluxes for ethanol-water mixtures were set to those from the experimental results in Section 4.4.2, and mass fluxes for ethanol-isopropanol and ethanol-hexane mixtures were chosen using Ditch et al.'s (2013) correlation (Eq. (2.6)). A circular pan that was 0.30 m in diameter and 40 mm tall was centered at the bottom of the domain. The sides of the pan were treated as adiabatic.

Figure 5.4 demonstrates that FDS flame temperature predictions are significantly larger than experimental measurements. The time-averaged temperature fields in Figure 5.5 show that there is a cold zone that persists for about 0.2 m above the pool surface. The large height of the fuel-rich core above the pool surface is caused by underpredicting turbulent kinetic energy near the pool surface as shown in Figure 5.6. This increases the mixing time scale required for combustion and results in the vapours combusting at a higher location than in a real pool fire.

Overprediction of the flame heights shown in Figure 5.7 can be attributed to the same reasons mentioned for the temperature overestimations. Predicted flame heights

Table 5.2: Vapour Compositions, Mass Fluxes, and Maximum HRR for FDS Gas Phase Validation Cases

y_1	$\dot{m}_1''$ ($\mathrm{kg\,m^{-2}\,s^{-1}}$)	$\dot{m}_2''$ ($\mathrm{kg\,m^{-2}\,s^{-1}}$)	HRR (kW)
Ethanol (1) - Water (2)			
0.69	0.0056	0.0025	10.6
0.75	0.0069	0.0023	13.1
0.81	0.0082	0.0019	15.6
0.88	0.0101	0.0014	19.1
1.00	0.0129	0.0000	24.4
Ethanol (1) - Isopropanol (2)			
0.00	0.0000	0.0216	50.5
0.15	0.0034	0.0177	47.9
0.40	0.0086	0.0115	43.2
0.60	0.0123	0.0071	39.9
0.85	0.0161	0.0023	35.9
Ethanol (1) - Hexane (2)			
0.00	0.0000	0.0330	96.8
0.20	0.0057	0.0227	77.4
0.40	0.0097	0.0147	61.5
0.60	0.0133	0.0081	49.0
0.85	0.0164	0.0026	38.7

were still linearly proportional to $\dot{Q}^{*2/5}$ though and appear to be higher by a constant value. This supports the observation that the flame is lifted from the base due to lack of combustion near the pool surface. Therefore, while the predicted flame heights in the batch pool fire simulations are expected to be overpredicted, they should follow the same trends with respect to a change in HRR.

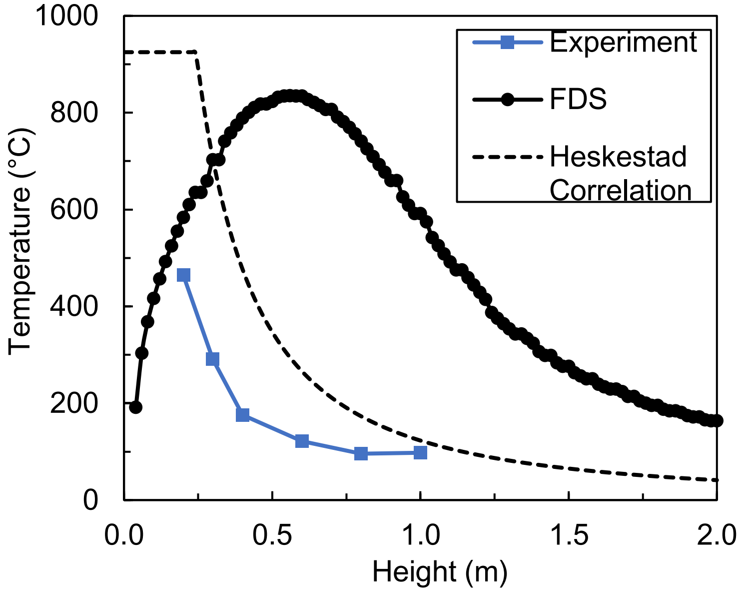

Figure 5.4: Centerline flame temperature for a steady-state, 50-50% w/w ethanol-water pool fire predicted by FDS. Experimental temperatures displayed are temperature-corrected for radiation.

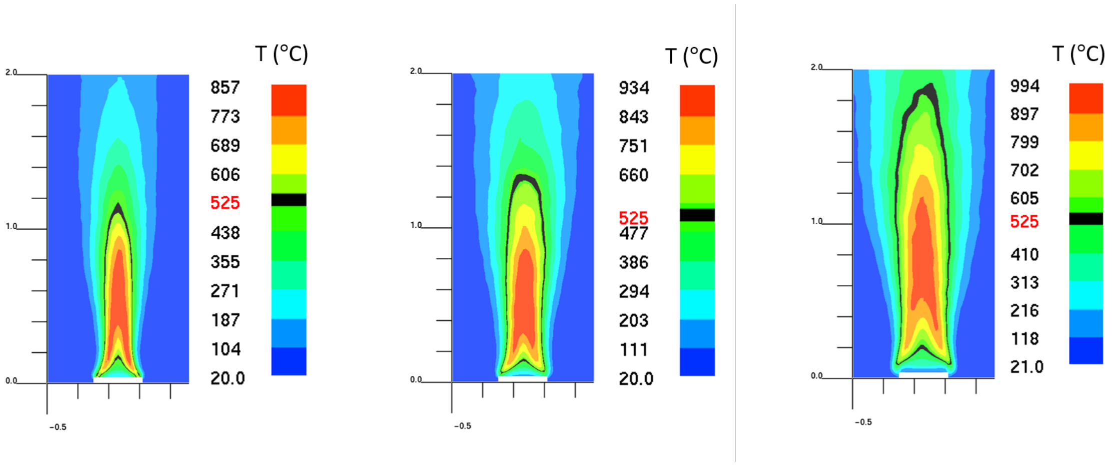

(a) Ethanol (b) Isopropanol (c) Hexane

Figure 5.5: Time-averaged (30-90 s) temperature slice for pure fuels burning in a 0.30 m diameter pan. The temperature contour at the Draper point (525 °C) is highlighted in black.

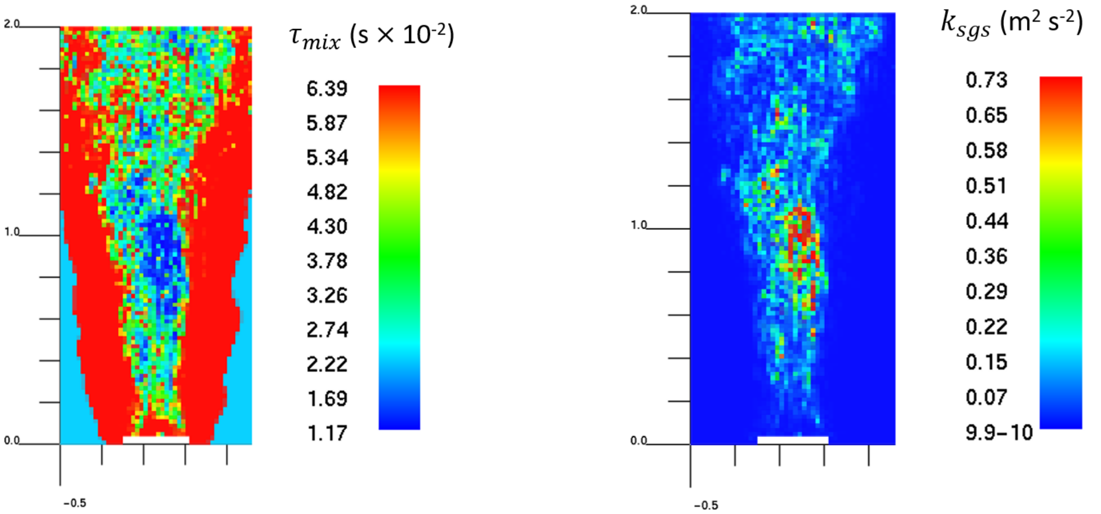

(a) Mixing Time

(b) Subgrid Turbulent Kinetic Energy

Figure 5.6: Instantaneous slice profiles at 90 s for (a) mixing time and (b) subgrid turbulent kinetic energy of a 50-50 %w/w ethanol-water pool fire.

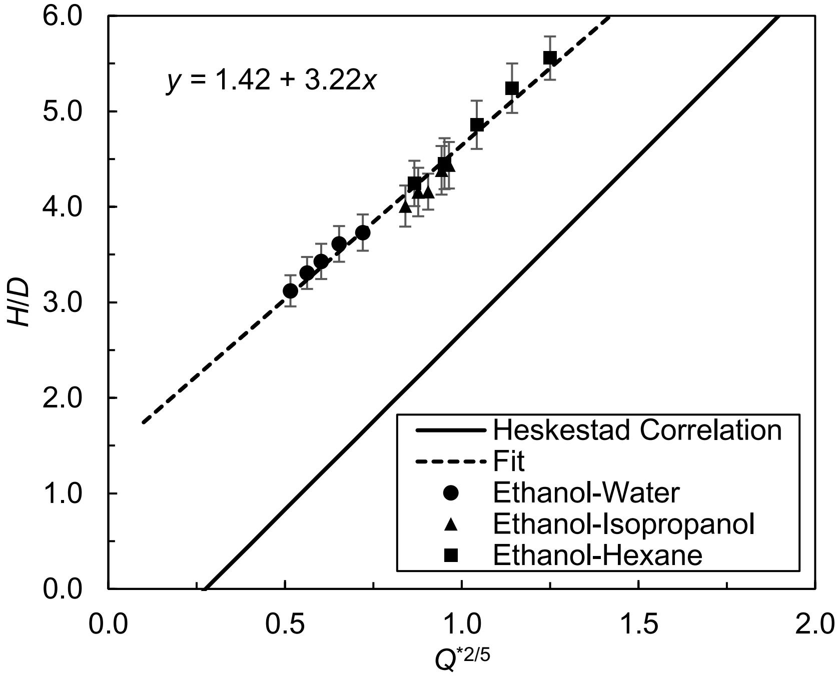

Figure 5.7: Mean flame height predictions from FDS for ethanol-water, ethanol-isopropanol, and ethanol-hexane blends with user-specified mass flux. Error bars indicate one standard deviation.

5.4.3 Transient Pool Fire Validation Study

Experiments of Y. Ding et al. (2014) were selected as validation cases to evaluate the overall performance of FDS with the multicomponent liquid pyrolysis model. The pan was square and had dimensions of $0.30 \times 0.30 \times 0.04$ m. The pan was centered at the bottom of the domain and the sides were treated as adiabatic. Ambient temperature was set to 14 °C. Results for mass flux, flame height, flame temperatures, and liquid composition are presented in Figures 5.8 to 5.10.

FDS was able to reproduce similar mass fluxes to the experiments for the 80-20% v/v and 50-50% v/v ethanol-heptane mixtures. The peak mass flux for the 20-80% v/v ethanol-heptane mixture was also reproduced. Initial mass fluxes were not reproduced because the pyrolysis model does not account for the growth period of the fire. Implementing a mass transfer based multicomponent evaporation model and an energy balance model for the condensed phase would resolve this issue.

Distillation effects on combustion behaviour are most notable in the mass flux and flame height predictions. In the 50-50% v/v ethanol-heptane mixture, a smooth decline in flame height occurred in both the simulation and the experiment when the ethanol composition reached around 80% w/w, which is when the vapour phase transitions to being predominantly ethanol. In the 20-80% v/v ethanol-heptane mixture, a quick rise in mass flux occurred 100 s after ignition, which is when most of the ethanol was depleted and the pool transitioned into a pure heptane fire. This same transition to single-component burning occurred after a longer period of time in the experiment due to sensible heating of the pool and also because the mass flux was lower.

Interestingly, for the 80-20% v/v mixture, FDS predicted a smooth reduction in flame height throughout the duration of the fire, while the experiment showed only two distinct average flame heights. This contrast may be due to imperfect mixing in the experiment, causing the less volatile component (heptane) to have a higher concentration at the pool surface compared to a well-mixed scenario. Regardless of this discrepancy in combustion behaviour, FDS correctly predicted that the flame height would approach that of pure ethanol.

Flame temperatures from FDS were overestimated in comparison to those of

Y. Ding et al. (2014). However, predicted temperatures outside of the flaming region tend to follow a similar trend. As mentioned in Section 5.4.2, this is likely caused by underpredicting turbulent mixing near the pool surface.

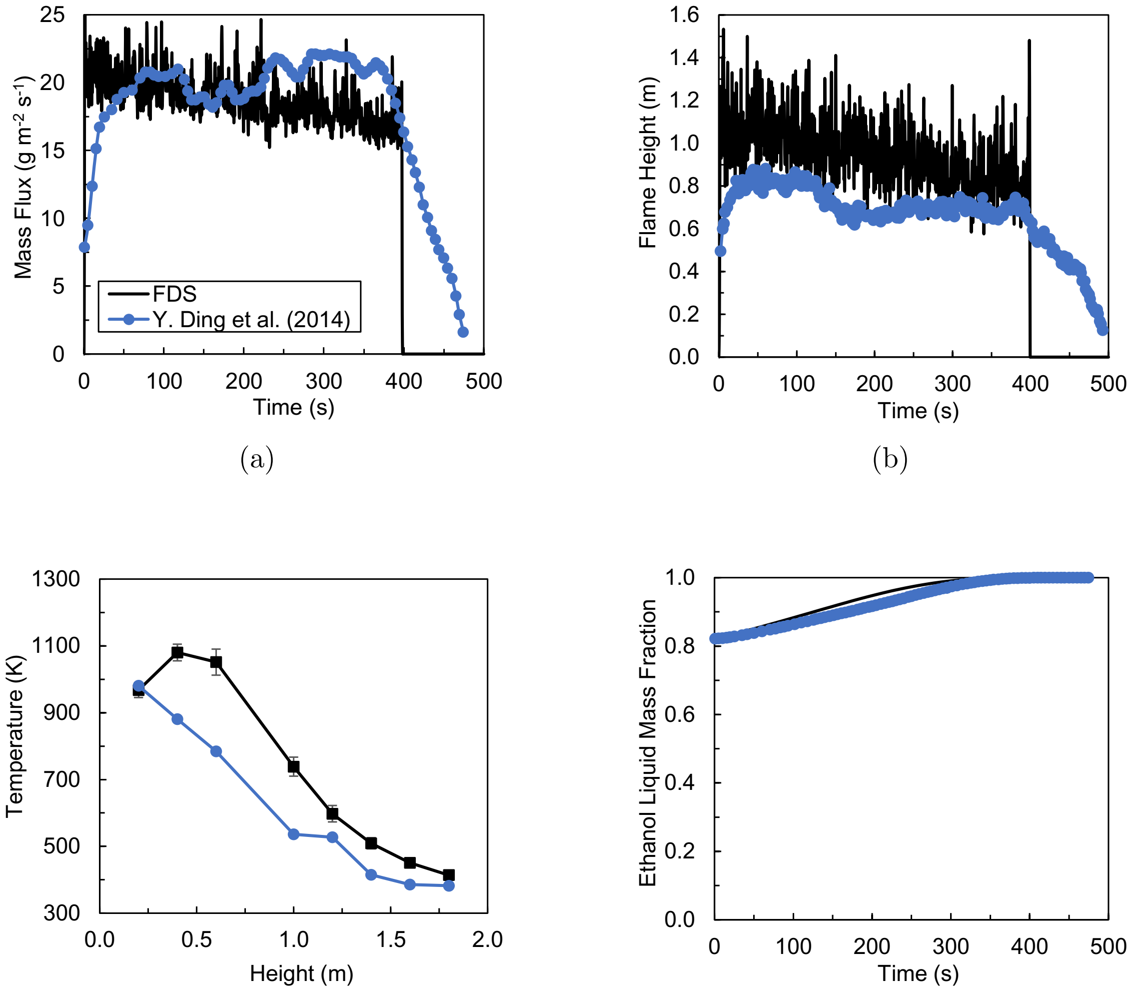

(a)

(b)

(c)

(d)

Figure 5.8: (a) Burning rate, (b) flame height, (c) time-averaged flame temperature (50-100 s), and (d) predicted liquid composition for the 80-20% v/v ethanol-heptane pool fire of Y. Ding et al. (2014).

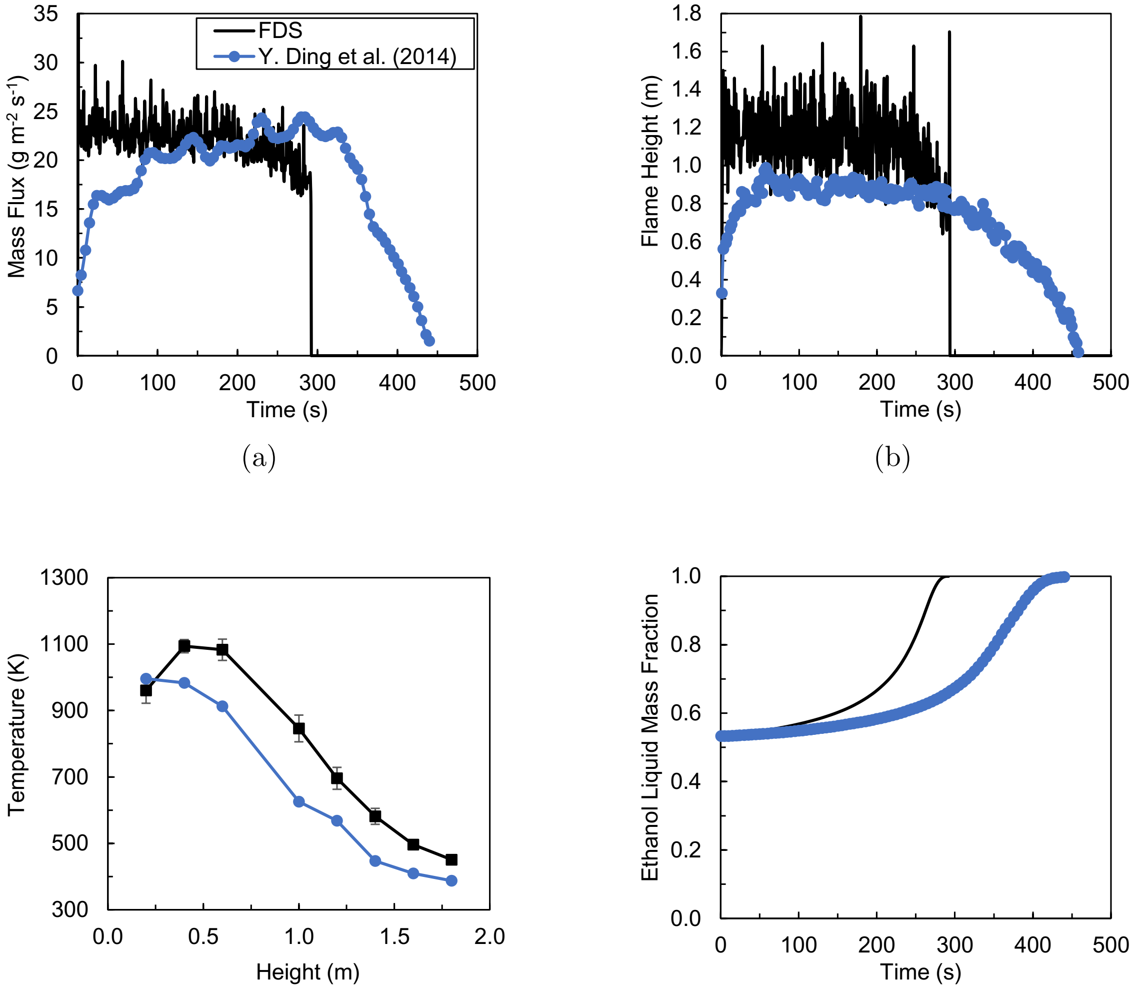

(a) (b) (c) (d)

Figure 5.9: (a) Burning rate, (b) flame height, (c) time-averaged flame temperature (50-100 s), and (d) predicted liquid composition for the 50-50% v/v ethanol-heptane pool fire of Y. Ding et al. (2014).

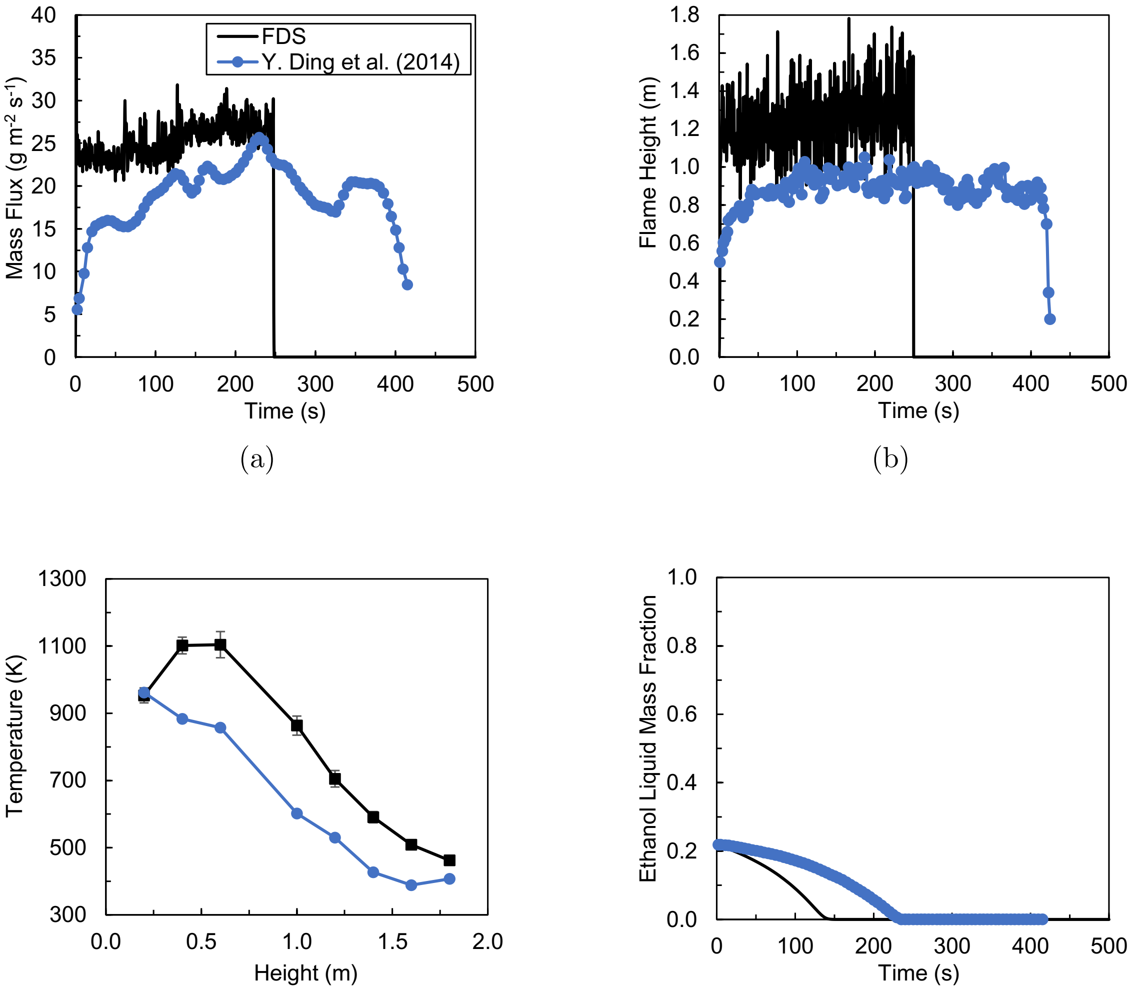

(a) (b)

(c) (d)

Figure 5.10: (a) Burning rate, (b) flame height, (c) time-averaged flame temperature (50-100 s), and (d) predicted liquid composition for the 20-80% v/v ethanol-heptane pool fire of Y. Ding et al. (2014).

5.5 General Discussion

Validation simulations for the gas phase model showed that flame temperatures and flame heights were consistently overestimated with the simulation settings that were used. Simulation conditions should be modified to obtain better mixing, which will result in more combustion near the pool surface and produce more realistic flame temperature and flame heights. It is recommended to use a two-step reaction to enable the fuel to partially combust near the fuel surface. Modification of the domain length and width may also enhance turbulence caused by air entrainment near the base of the pool.

The presented evaporation model is limited by the assumptions that evaporation is heat transfer-dependent and that the liquid is always at the bubble-point temperature. This approach results in the pool is always at its maximum burning stage. Thus, the model is most useful for modelling pool fires that will burn for a long period of time. For modelling time-sensitive scenarios, a basic fire growth rate and decay rate model like a t^2 model (Ingason et al., 2015, Chapter 6) can be used with the present modelling approach to approximate the initial and final periods of the fire.

It was shown that inclusion of a VLE model and mixing model for the liquid enabled FDS to predict changes in combustion behaviour caused by distillation. Based on the transient pool fire validation study in Section 5.4.3, the present modelling approach seems to give reasonable predictions of the maximum evaporation rate in binary-component pool fires. Although the predicted flame heights were overestimated, they generally followed the same trends as in the experiments of Y. Ding et al. (2014). Some discrepancy in the transition between multicomponent and single-component burning exists (*e.g.* Figure 5.8b) because the pool is assumed to be well-mixed. Thus, it is likely that the model will not be able to predict exact burning rate trends in mixtures with a high relative volatility, which tend to have sharp transitions in burning behaviour caused by distillation (Y. Ding et al., 2014; X. Wang, He, et al., 2018).

In practical fire scenarios, the computational domain is typically much larger than the actual pool, so the computational mesh may be too coarse to accurately predict heat feedback to the pool surface. The recommended methodology for using CFD to model multicomponent pool fire scenarios is visually demonstrated in Figure 5.11. In

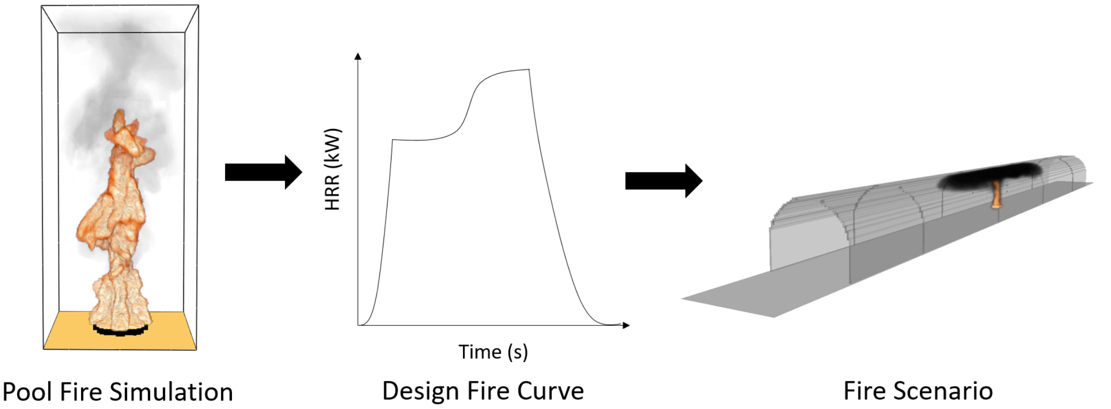

Pool Fire Simulation

Design Fire Curve

Fire Scenario

Figure 5.11: Suggested approach for applying the proposed multicomponent pool fire model to a CFD simulation of a fire scenario.

fire scenario simulations, it is recommended to input a pre-defined HRR curve that is constructed in a separate simulation on the pool fire alone. Alternatively, the batch pool fire simulation methodology presented in Chapter 4 may also be used to create the HRR curve. The downside to supplying a HRR curve is that soot generation and CO concentrations cannot be accurately predicted if the correct fuel composition is not given. If more detailed estimates of soot production and CO concentrations are required, then the estimated mass flux of each component over time needs to be supplied to FDS instead of the HRR.

Chapter 6

Conclusions and Recommendations

Combustion behaviour in binary-component pool fires was investigated experimentally in batch and continuously fed scenarios. Predictive capabilities of common engineering tools for estimating mass burning rates, flame temperatures, and flame heights in pool fires were evaluated against data obtained in the present study and in literature. Tools included empirical correlations, a global energy balance model, and computational fluid dynamics (CFD) software. Several modifications to some of the tools were implemented to enable their application to multicomponent fuels.

This work made several advances in predicting combustion behaviour of multicomponent pool fires. First, a distillation model was developed and validated against batch and continuously fed pool fire experiments. The distillation model was then implemented into Fire Dynamics Simulator (FDS) and validated against a batch pool fire scenario. This contribution enables tracking the pool composition over the course of burning and yields more accurate predictions of liquid and vapour phase properties, which are necessary for making predictions of general combustion behaviour. Then, recommendations on burning rate model selection were formulated based on the relative volatility of components in a mixture. This will facilitate making more informed and practical decisions on what model best describes the relationship between burning rate and fuel composition. Finally, Heskestad's flame height and flame temperature correlations were verified against steady-state experiments, which increases confidence in using these established tools in multicomponent pool fire scenarios.

Fuel composition measurements from batch pool fire experiments showed that assuming the liquid phase as well-mixed gives reasonable estimates on how distillation will progress over the duration of a pool fire. However, there were instances where evaporation of the more volatile components was overestimated, which signifies that the mixing regime in a pool fire falls somewhere between well-mixed and diffusion limited. This finding is in agreement with studies from literature. Accurate predictions of the local liquid composition require detailed mixing models. It is recommended to develop a mixing model that falls somewhere between well-mixed and diffusion-limited. This can be done by dividing the pool into an upper and lower layer that are well-mixed and diffusion-limited, respectively.

Dependency of combustion behaviour on the composition of a liquid fuel was dictated by vapour-liquid-equilibrium (VLE). The relationship between burning rate and vapour composition for ethanol-water and ethanol-isopropanol solutions was linear. The relationship was nonlinear for ethanol-hexane mixtures. Linear variation in burning rate with vapour composition is expected to be applicable to aqueous flammable mixtures and multicomponent fuels with a low relative volatility in general. The correlation of Babrauskas (1983) and the global model are recommended for these scenarios. Deviation from linearity is expected to increase with relative volatility. For scenarios involving a fuel mixture with a high relative volatility containing only flammable components, the model of Ditch et al. (2013) and the global model are recommended. Factors that contribute to nonlinear behaviour could be the reduction in sooting propensity by blending oxygenates with hydrocarbons, which influences other combustion properties (combustion efficiency, radiant fraction, soot yield) that affect heat feedback to the pool surface. Further investigation is recommended for quantifying how combustion properties are related to fuel composition in hydrocarbon-oxygenate blends.

The global modelling approach was able to estimate the limiting fuel concentration required for sustained burning in an aqueous fuel. Other empirical models do not have this capability, so the global modelling approach is recommended for cases where aqueous flammable mixtures are present. FDS could also be used to model extinction in aqueous flammable mixtures, but this requires further validation against batch pool fire experiments.

Agreement between Heskestad's flame height and flame temperature correlations and the experimental data obtained from steady-state pool fires supports the usage of these correlations with multicomponent fuels. Correct usage of these correlations requires the steady-state vapour composition of the fuel. However, predicting steady-state composition is not always simple. The extent to which distillation occurs in a continuously fed pool fire is dependent on the relative volatility of the mixture and the feed rate. For mixtures with a low relative volatility, there is little error in assuming that distillation has no effect on the composition of the pool. The error from making this assumption will increase with the relative volatility of the mixture.

The default gas phase model in FDS overestimated flame heights and flame temperatures in steady-state binary pool fires where no pyrolysis model was used. This was attributed to underestimating turbulent mixing at the pool base. Improved modelling of near-surface phenomena is required to resolve this issue.

A pyrolysis model suitable for predicting multicomponent evaporation was implemented into FDS and validated against batch ethanol-heptane pool fire experiments performed by Y. Ding et al. (2014). The new pyrolysis model gave adequate estimates of the maximum burning rates. Changes in burning rate and flame height caused by distillation were reproduced in FDS. The pyrolysis model was unable to predict rapid transitions between multicomponent burning and single-component burning. This is attributed to the assumption of having a well-mixed liquid phase. Currently, the pyrolysis model is only suitable for predicting fire dynamics for fully grown fires. Basic fire growth and decay models need to be used in conjunction with the pyrolysis model for time-sensitive cases involving multicomponent fuels.

References

Ahrens, M. (2019). *Home cooking fires* (Tech. Rep.). National Fire Protection Association. https://www.nfpa.org//-/media/Files/News-and-Research/Fire-statistics-and-reports/US-Fire-Problem/Fire-causes/oscooking.pdf.

Alston, J. J., & Dembsey, N. A. (2003). Evaluation of dimensionless flame height parameters to account for fuel source effects. *Fire Safety Science*, *7*, 569-580.

ANSYS. (2009). *ANSYS FLUENT 12.0 theory guide.* https://www.afs.enea.it/project/neptunius/docs/fluent/html/th/main_pre.htm. (Accessed: 2019-12-21)

Apte, V. (1998). Effect of scale and fuel type on the characteristics of pool fires for fire fighting training. *Fire Safety Journal*, *31*(4), 283-298.

Armas, O., Gómez, M. A., Barrientos, E. J., & Boehman, A. L. (2011). Estimation of opacity tendency of ethanol–and biodiesel–diesel blends by means of the smoke point technique. *Energy & Fuels*, *25*(7), 3283-3288. doi: 10.1021/ef2005817

Assael, M. J., & Kakosimos, K. E. (2010). *Fires, explosions, and toxic gas dispersions.* Boca Raton, FL: CRC Press.

ASTM D1322-18. (2018). *Standard test method for smoke point of kerosene and aviation turbine fuel* (Standard). West Conshohocken, PA: ASTM International.

Babrauskas, V. (1983). Estimating large pool fire burning rates. *Fire Technology*, *19*(4), 251–261.

Babrauskas, V. (2016). Heat release rates. In M. Hurley et al. (Eds.), *SFPE handbook of fire protection engineering* (5th ed., p. 865-866). New York: Society of Fire Protection Engineers.

Ballard, L. H., & Winkle, M. V. (1952). Vapor-liquid equilibria at 760 Mm. pressure. 2-propanol-methanol, 2-propanol-ethyl alcohol, 2-propanol-propanol, and 2-propanol-2-butyl alcohol systems. *Industrial & Engineering Chemistry*, *44*(10), 2450-2453.

Bhattacharya, P., Ghosal, S., & Som, S. (1996). Evaporation of multicomponent liquid fuel droplets. *International Journal of Energy Research*, *20*(5), 385-398.

Blinov, V. I., & Khudyakov, G. N. (1957). Certain laws governing the diffusive burning of liquids. *Academiia Nauk, SSR Doklady*, *113*, 1094-1098.

Blinov, V. I., & Khudyakov, G. N. (1961). *Diffusion burning of liquids* (Tech. Rep. No. NTIS AD296762).

Brohez, S., Delvosalle, C., & Marlair, G. (2004). A two-thermocouples probe for radiation corrections of measured temperatures in compartment fires. *Fire Safety Journal*, *39*(5), 399-411.

Brooks, M. R., & Crowl, D. A. (2007). Vapor flammability above aqueous solutions of flammable liquids. *Journal of Loss Prevention in the Process Industries*, *20*(4-6), 477-485.

Brosmer, M. A., & Tien, C. L. (1987). Radiative energy blockage in pool fires. *Combustion Science and Technology*, *51*, 21-37.

Burgess, D., Strasser, A., & Grumer, J. (1961). Diffusive burning of liquid fuels in open trays. *Fire Research Abstracts and Reviews*, *3*(3).

Chatris, J., Quintela, J., Folch, J., Planas, E., Arnaldos, J., & Casal, J. (2001). Experimental study of burning rate in hydrocarbon pool fires. *Combustion and flame*, *126*(1-2), 1373-1383.

Chaudhary, A., Gupta, A., Kumar, S., & Kumar, R. (2019). Pool fires of jatropha biodiesel and their blends with petroleum diesel. *Experimental Thermal and Fluid Science*, *101*, 175-185.

Chen, B., Lu, S., Li, C., Kang, Q., & Yuan, M. (2012). Unsteady burning of thin-layer pool fires. *Journal of Fire Sciences*, *30*(1), 3-15. doi: 10.1177/0734904111415807

Chen, B., Lu, S.-X., Li, C.-H., Kang, Q.-S., & Lecoustre, V. (2011). Initial fuel temperature effects on burning rate of pool fire. *Journal of Hazardous Materials*, *188*(1-3), 369-374.

Corlett, R., & Fu, T. (1966). Some recent experiments with pool fires. *Pyrodynamics*, *1*, 253-269.

Cozzani, V., Gubinelli, G., Antonioni, G., Spadoni, G., & Zanelli, S. (2005). The assessment of risk caused by domino effect in quantitative area risk analysis. *Journal of Hazardous Materials*, *127*(1), 14-30. doi: https://doi.org/10.1016/j.jhazmat.2005.07.003

da Cunha, S. B. (2016). A review of quantitative risk assessment of onshore pipelines. *Journal of Loss Prevention in the Process Industries*, *44*, 282-298. doi: https://doi.org/10.1016/j.jlp.2016.09.016

Daniels, G. E. (1968). Measurement of gas temperature and the radiation compensating thermocouple. *Journal of Applied Meteorology*, *7*(6), 1026-1035.

Deardorff, J. W. (1980). Stratocumulus-capped mixed layers derived from a three-dimensional model. *Boundary-Layer Meteorology*, *18*(4), 495-527.

De Falco, G., Moggia, G., Sirignano, M., Commodo, M., Minutolo, P., & D'Anna, A. (2017). Exploring soot particle concentration and emissivity by transient thermocouples measurements in laminar partially premixed coflow flames. *Energies*, *10*(2), 232.

Delichatsios, M. A. (1987). Air entrainment into buoyant jet flames and pool fires. *Combustion and Flame*, *70*(1), 33-46.

Dillon, S., Carpenter, A., & Ogle, R. (2009). Comparative fire risk of motor vehicle fuels: Gasoline versus ethanol. *Process Safety Progress*, *28*(2), 171-178.

Ding, C., Xu, B., Wang, W., Wang, X., & Wang, J. (2019). Combustion characteristics of lithium-ion electrolyte with a focus on the role of lipf6 salt and liquid-vapor equilibrium. *Acta Microscopica*, *28*(6), 1556-1567.

Ding, Y., Lin, F., Lu, S., He, Q., Wang, C., & Zhou, R. (2017). The effect of azeotropic blended fuel on combustion characteristics in a ceiling vented compartment. *Fuel*, *189*, 1-7.

Ding, Y., Wang, C., & Lu, S. (2014). The effect of azeotropism on combustion characteristics of blended fuel pool fire. *Journal of Hazardous Materials*, *271*, 82-88.

Ditch, B. D., de Ris, J. L., Blanchat, T. K., Chaos, M., Bill Jr, R. G., & Dorofeev, S. B. (2013). Pool fires - an empirical correlation. *Combustion and Flame*, *160*(12), 2964-2974.

Dlugogorski, B., & Wilson, M. (2000). Effect of ullage on properties of small-scale pool fires. *Developments in Chemical Engineering and Mineral Processing*, *8*(1-2), 149-166.

Drysdale, D. (1998). *An introduction to fire dynamics* (2nd ed.). John Wiley & Sons.

Eddings, E. G., Yan, S., Ciro, W., & Sarofim, A. F. (2005). Formulation of a surrogate for the simulation of jet fuel pool fires. *Combustion Science and Technology*, *177*, 715-739.

Esarte, C., Millera, A., Bilbao, R., & Alzueta, M. U. (2009). Gas and soot products formed in the pyrolysis of acetylene–ethanol blends under flow reactor conditions. *Fuel Processing Technology*, *90*(4), 496-503. doi: https://doi.org/10.1016/j.fuproc.2009.01.011

Eshetu, G. G., Bertrand, J.-P., Lecocq, A., Grugeon, S., Laruelle, S., Armand, M., & Marlair, G. (2014). Fire behavior of carbonates-based electrolytes used in li-ion rechargeable batteries with a focus on the role of the LiPF6 and LiFSI salts. *Journal of Power Sources*, *269*, 804-811.

Feitosa, F. X., Caetano, A. C. R., Cidade, T. B., & de Sant'Ana, H. B. (2009). Viscosity and density of binary mixtures of ethyl alcohol with n-alkanes (C6, C8, and C10). *Journal of Chemical & Engineering Data*, *54*(10), 2957-2963.

Fu, Y., Lu, S., Shi, L., Cheng, X., & Zhang, H. (2016). Combustion characteristics of electrolyte pool fires for lithium ion batteries. *Journal of The Electrochemical Society*, *163*(9), A2022-A2028.

Germano, M., Piomelli, U., Moin, P., & Cabot, W. H. (1991). A dynamic subgrid-scale eddy viscosity model. *Physics of Fluids A: Fluid Dynamics*, *3*(7), 1760-1765.

Gill, R. J., & Olson, D. B. (1984). Estimation of soot thresholds for fuel mixtures. *Combustion Science and Technology*, *40*(5-6), 307-315. doi: 10.1080/00102208408923814

Gottuk, D., & White, D. (2016). Liquid fuel fires. In M. Hurley et al. (Eds.), *SFPE handbook of fire protection engineering* (5th ed., p. 2573-2574). New York: Society of Fire Protection Engineers.

Green, D. W., & Perry, R. H. (2007). *Perry's chemical engineers' handbook* (8th ed.). New York: McGraw-Hill Education.

Grosshandler, W. L. (1993). *RADCAL: a narrow-band model for radiation calculations in a combustion environment* (Tech. Rep. No. 1402). National Institute of Standards and Technology.

Grumer, J., Strasser, A., Kubala, T. A., & Burgess, D. (1961). Uncontrolled diffusive burning of some new liquid propellants. *American Chemical Society Division of Fuel Chemistry*, *1*.

Hägglund, B., & Persson, L. E. (1976). *Heat radiation from petroleum fires* (Tech. Rep. No. FOA-C-20126-D6(A3)). Försvarets Forskningsanstalt, Stockholm.

Hamins, A. P., Fischer, S., Kashiwagi, T., Klassen, M., & Gore, J. (1994). Heat feedback to the fuel surface in pool fires. *Combustion Science and Technology*, *97*(1-3), 37–62.

Hamins, A. P., Kashiwagi, T., & Buch, R. R. (1996). Characteristics of pool fire burning. In *Fire resistance of industrial fluids.* ASTM International.

Hamins, A. P., & Lock, A. (2016). *The structure of a moderate-scale methanol pool fire* (Tech. Rep. No. 1928). National Institute of Standards and Technology. doi: https://doi.org/10.6028/NIST.TN.1928

Hamins, A. P., Yang, J. C., & Kashiwagi, T. (1999). *Global model for predicting the burning rates of liquid pool fires* (Tech. Rep. No. 6381). National Institute of Standards and Technology.

Hayasaka, H. (1997). Unsteady burning rates of small pool fires. *Fire Safety Science*, *5*, 499-510.

Heskestad, G. (1983). Luminous heights of turbulent diffusion flames. *Fire Safety Journal*, *5*(2), 103–108.

Heskestad, G. (1984). Engineering relations for fire plumes. *Fire Safety Journal*, *7*(1), 25-32.

Heskestad, G. (2016). Fire plumes, flame height, and air entrainment. In M. Hurley et al. (Eds.), *SFPE handbook of fire protection engineering* (5th ed., p. 396-428). New York: Society of Fire Protection Engineers.

Hiroshi, K., & Taro, Y. (1988). Air entrainment and thermal radiation from heptane pool fires. *Fire Technology*, *24*(1), 33-47.

Hostikka, S., McGrattan, K. B., & Hamins, A. P. (2003). Numerical modeling of pool fires using LES and finite volume method for radiation. *Fire Safety Science*, *7*, 383–394.

Hottel, H. C. (1959). Certain laws governing the diffusive burning of liquids-A review. *Fire Research Abstracts and Reviews*, *1*, 41-44.

Hu, L., Fong, N., Yang, L., Chow, W., Li, Y., & Huo, R. (2007). Modeling fire-induced smoke spread and carbon monoxide transportation in a long channel: fire dynamics simulator comparisons with measured data. *Journal of Hazardous Materials*, *140*(1-2), 293–298.

Hu, L., Liu, S., & Wu, L. (2013). Flame radiation feedback to fuel surface in medium ethanol and heptane pool fires with cross air flow. *Combustion and Flame*, *160*(2), 295-306.

Ingason, H., Li, Y. Z., & Lönnermark, A. (2015). *Tunnel fire dynamics.* Springer.

Institut de Radioprotection et de Sûreté Nucléaire. (2019). *ISIS.* https://gforge.irsn.fr/gf/project/isis. (Accessed: 2019-12-18)

Johnston, R. (2013, September 11). *Railway investigation R13D0054 – Railway safety advisory letter - Determination of petroleum crude oil properties for safe transportation.* http://www.tsb.gc.ca/eng/medias-media/sur-safe/letter/rail/2013/r13d0054/r13d0054-617-12-13.html. (Accessed: 2019-07-15)

Joulain, P. (1998). The behavior of pool fires: State of the art and new insights. *Symposium (International) on Combustion*, *27*(2), 2691-2706.

Kamihama, N., Matsuda, H., Kurihara, K., Tochigi, K., & Oba, S. (2012). Isobaric vapor-liquid equilibria for ethanol + water + ethylene glycol and its constituent three binary systems. *Journal of Chemical & Engineering Data*, *57*(2), 339-344.

Kinoshita, C. M., & Lee, M. Y. (1994). Flame luminosity of methanol & additive fuel mixtures. *Combustion Science and Technology*, *96*(1-3), 103-119.

Kojima, K., Ochi, K., & Nakazawa, Y. (1969). Relationship between liquid activity coefficient and composition for ternary systems. *International Chemical Engineering*, *9*(2), 342.

Kong, D., Zhang, Z., Ping, P., He, X., & Yang, H. (2018). Effects of the initial fuel temperature on burning behavior of crude oil pool fire in ice cavities. *Experimental Heat Transfer*, *31*(5), 436-449.

Krishna, R., & Standart, G. L. (1979). Mass and energy transfer in multicomponent systems. *Chemical Engineering Communications*, *3*(4-5), 201-275. doi: 10.1080/00986447908935865

Kudryavtseva, L., & Susarev, M. (1963). Liquid-vapor equilibriums in the systems acetone-hexane and hexane-ethyl alcohol at 35, 45, and 55 and 760mmHg. *Zhurnal Pikladnoi Khimii*, *36*, 1471-1477.

Kung, H. C., & Stavrianidis, P. (1982). Buoyant plumes of large-scale pool fires. *Symposium (International) on Combustion*, *19*(1), 905-912.

Lai, H.-S., Lin, Y.-F., & Tu, C.-H. (2014). Isobaric (vapor + liquid) equilibria for the ternary system of (ethanol + water + 1, 3-propanediol) and three constituent binary systems at P = 101.3 kPa. *The Journal of Chemical Thermodynamics*, *68*, 13-19.

Law, C. (1976). Multicomponent droplet combustion with rapid internal mixing. *Combustion and Flame*, *26*, 219-233.

Law, C. (1978). Internal boiling and superheating in vaporizing multicomponent droplets. *AIChE Journal*, *24*(4), 626–632.

Law, C. (1982). Recent advances in droplet vaporization and combustion. *Progress in Energy and Combustion Science*, *8*(3), 171–201.

Leckner, B. (1972). Spectral and total emissivity of water vapor and carbon dioxide. *Combustion and Flame*, *19*(1), 33–48.

Lemaire, R., & Menanteau, S. (2017). Assessment of radiation correction methods for bare bead thermocouples in a combustion environment. *International Journal of Thermal Sciences*, *122*, 186-200.

Li, J., Chen, C., & Wang, J. (2000). Vapor-liquid equilibrium data and their correlation for binary systems consisting of ethanol, 2-propanol, 1,2-ethanediol and methyl benzoate. *Fluid phase equilibria*, *169*(1), 75-84.

Liu, H., Wang, C., Zhang, J., Luo, Q., Sun, H., Xu, M., & Yang, S. (2018). The effect of mixture ratio on combustion characteristics of n-propyl alcohol-water binary mixture. *Journal of Thermal Analysis and Calorimetry*. doi: 10.1007/s10973-018-7281-0

Lloyd, J., & Moran, W. (1974). Natural convection adjacent to horizontal surface of various planforms. *Journal of Heat Transfer*, *96*(4), 443–447.

Magnussen, B. F. (2005). The eddy dissipation concept—A bridge between science and technology. In *ECCOMAS thematic conference on computational combustion* (pp. 21–24).

Magnussen, B. F., & Hjertager, B. H. (1977). On mathematical modeling of turbulent combustion with special emphasis on soot formation and combustion. *Symposium (International) on Combustion*, *16*(1), 719–729.

McCaffrey, B. (1995). Flame height. In *SFPE handbook of fire protection engineering* (2nd ed.). Quincy, MA: Society of Fire Protection Engineers and National Fire Protection Association.

McDermott, R., McGrattan, K. B., & Floyd, J. (2011). A simple reaction time scale for under-resolved fire dynamics. *Fire Safety Science*, *10*, 809-820.

McGrattan, K. B., Baum, H. R., & Rehm, R. G. (1998). Large eddy simulations of smoke movement. *Fire Safety Journal*, *30*(2), 161-178.

McGrattan, K. B., Hostikka, S., McDermott, R., Floyd, J., & Vanella, M. (2019). Fire Dynamics Simulator, Technical Reference Guide Volume 3: Validation. *NIST special publication*, *1018-3*(6).

McGrattan, K. B., McDermott, R., Hostikka, S., Floyd, J., & Vanella, M. (2019). Fire Dynamics Simulator, Technical Reference Guide Volume 1: Mathematical Model. *NIST special publication*, *1018-1*(6).

Miao, Z., Wenhua, S., Ji, W., & Zhen, C. (2014). Accident consequence simulation analysis of pool fire in fire dike. *Procedia Engineering*, *84*, 565–577.

Mishra, K. B., & Wehrstedt, K.-D. (2013). Diffusive burning characteristics of peroxy-fuels. *Fuel*, *113*, 158-164. doi: https://doi.org/10.1016/j.fuel.2013.05.031

Mishra, K. B., & Wehrstedt, K.-D. (2015). Diffusive burning of blended peroxy-fuels: Some experimental results. *Fuel Processing Technology*, *140*, 324–330.

Mudan, K. S. (1987). Geometric view factors for thermal radiation hazard assessment. *Fire Safety Journal*, *12*(2), 89-96. doi: https://doi.org/10.1016/0379-7112(87)90024-5

Novozhilov, V., & Koseki, H. (2004). Cfd prediction of pool fire burning rates and flame feedback. *Combustion Science and Technology*, *176*(8), 1283–1307.

OpenFOAM Foundation. (2019). *C++ source code guide.* https://cpp.openfoam.org/v7/.

Orloff, L., & de Ris, J. (1982). Froude modeling of pool fires. *Symposium (International) on Combustion*, *19*(1), 885-895.

Ortega, J., & Espiau, F. (2003). A new correlation method for vapor- liquid equilibria and excess enthalpies for nonideal solutions using a genetic algorithm. Application to ethanol + an n-alkane mixtures. *Industrial & engineering chemistry research*, *42*(20), 4978-4992.

Palazzi, E., Caviglione, C., Reverberi, A. P., & Fabiano, B. (2017). A short-cut analytical model of hydrocarbon pool fire of different geometries, with enhanced view factor evaluation. *Process Safety and Environmental Protection*, *110*, 89-101.

Prakash, S., & Sirignano, W. (1978). Liquid fuel droplet heating with internal circulation. *International Journal of Heat and Mass Transfer*, *21*(7), 885-895. doi: https://doi.org/10.1016/0017-9310(78)90180-1

Prasad, K., Li, C., Kailasanath, K., Ndubizu, C., Ananth, R., & Tatem, P. (1999). Numerical modelling of methanol liquid pool fires. *Combustion Theory and Modelling*, *3*(4), 743-768.

Pula, R., Khan, F. I., Veitch, B., & Amyotte, P. R. (2005). Revised fire consequence models for offshore quantitative risk assessment. *Journal of Loss Prevention in the Process Industries*, *18*(4), 443-454. (Selected Papers Presented at the International Conference on Bhopal Gas Tragedy and its Effects on Process Safety) doi: https://doi.org/10.1016/j.jlp.2005.07.014

Quintiere, J. G. (2006). Burning rate. In *Fundamentals of fire phenomena* (p. 227-256). Chichester: John Wiley & Sons.

Rasbash, D., Rogowski, Z., & Stark, G. (1956). Properties of fires of liquids. *Fuel*, *31*, 94-107.

Rehm, R. G., & Baum, H. R. (1978). The equations of motion for thermally driven, buoyant flows. *Journal of Research of the NBS*, *83*(297-308), 2.

Rieder, R. M., & Thompson, A. R. (1949). Vapor-liquid equilibria measured by a Gillespie still-ethyl alcohol-water system. *Industrial & Engineering Chemistry*, *41*(12), 2905-2908.

Sahu, D., Kumar, S., Jain, S., & Gupta, A. (2016). Experimental and numerical simulation studies on diesel pool fire. *Fire and Materials*, *40*(8), 1016–1035.

Sandia National Laboratories. (2017). *SIERRA low mach module: Fuego theory manual - version 4.46* (Tech. Rep. No. SAND2017-10407). Sandia National Laboratories.

Schälike, S., Chun, H., Mishra, K. B., Wehrstedt, K.-D., & Schönbucher, A. (2013). Mass burning rates of di-tert-butyl peroxide pool fires—experimental study and modeling. *Combustion Science and Technology*, *185*(3), 408-419. doi: 10.1080/00102202.2012.726664

Segovia, J. F. P., Beji, T., & Merci, B. (2018). Assessment of an evaporation model in CFD simulations of a free liquid pool fire using the mass transfer number approach. *Flow, Turbulence and Combustion*, *101*(4), 1059-1072.

Sikanen, T., & Hostikka, S. (2016). Modeling and simulation of liquid pool fires with in-depth radiation absorption and heat transfer. *Fire Safety Journal*, *80*, 95-109.

Sikanen, T., & Hostikka, S. (2017). Predicting the heat release rates of liquid pool fires in mechanically ventilated compartments. *Fire Safety Journal*, *91*, 266-275. doi: https://doi.org/10.1016/j.firesaf.2017.03.060

Sinor, J., & Weber, J. H. (1960). Vapor-liquid equilibria at atmospheric pressure. systems containing ethyl alcohol, n-hexane, benzene, and methylcyclopentane. *Journal of Chemical and Engineering Data*, *5*(3), 243-247.

Smagorinsky, J. (1963). General circulation experiments with the primitive equations: I. The basic experiment. *Monthly Weather Review*, *91*(3), 99-164.

Smith, J. M., Van Ness, H. C., & Abbott, M. M. (2005). *Introduction to chemical engineering thermodynamics* (5th ed.). New York, NY: McGraw Hill.

Snegirev, A. Y. (2004). Statistical modeling of thermal radiation transfer in buoyant turbulent diffusion flames. *Combustion and Flame*, *136*(1-2), 51–71.

Spalding, D. B. (1953). The combustion of liquid fuels. *Symposium (International) on Combustion*, *4*(1), 847–864.

Statistics Canada. (2017). *Fire statistics in Canada, selected observations from the national fire information database 2005 to 2014* (Tech. Rep.). Canadian Centre for Justice Statistics.

Sugawa, O., Kawagoe, K., & Oka, Y. (1991). Burning behavior in a poor-ventilation compartment fire — ghosting fire —. *Nuclear Engineering and Design*, *125*(3), 347-352.

Tavelli, S., Derudi, M., Cuoci, A., & Frassoldati, A. (2013). Numerical analysis of pool fire consequences in confined environments. *Chemical Engineering Transactions*, 127–132.

Taylor, R., & Krishna, R. (1993). *Multicomponent mass transfer.* Canada: John Wiley & Sons.

Tewarson, A. (1984). *Smoke point height and fire properties of materials* (Tech. Rep. No. NIST-GCR-88-555). National Institute of Standards and Technology.

Thomas, P. (1963). The size of flame from natural fires. *Symposium (International) on Combustion*, *9*(1), 844-859.

Tian, X., Zhong, M., Shi, C., Zhang, P., & Liu, C. (2018). Experimental study of the combustion characteristics of methanol-gasoline blends pool fires in a full-scale tunnel. *Fire and Materials*, *42*(4), 386-393.

Tien, C., & Lee, S. (1982). Flame radiation. *Progress in Energy and Combustion Science*, *8*(1), 41–59.

Vali, A., Nobes, D. S., & Kostiuk, L. W. (2015). Fluid motion and energy transfer within burning liquid fuel pools of various thicknesses. *Combustion and Flame*, *162*(4), 1477-1488.

Van Ness, H. C., Soczek, C., Peloquin, G., & Machado, R. (1967). Thermodynamic excess properties of three alcohol-hydrocarbon systems. *Journal of Chemical and Engineering Data*, *12*(2), 217-224.

Vienneau, H. (1964). *Mixing controlled flame heights from circular jets* (BSc Thesis). Department of Chemical Engineering, University of New Brunswick, Fredericton, NB.

Vipin, Pandey, S. K., Tauseef, S. M., Abbasi, T., & Abbasi, S. A. (2018). Pool fires in chemical process industries: Occurrence, mechanism, management. *Journal of Failure Analysis and Prevention*, *18*(5), 1224-1261. doi: 10.1007/s11668-018-0517-2

Walker, J., & Stocks, B. (1968). Thermocouple errors in forest fire research. *Fire Technology*, *4*(1), 59-62.

Wang, C., Ding, Y., & Lu, S. (2014). Large eddy simulation of ethanol-gasoline fire. *Procedia Engineering*, *71*, 421–426.

Wang, Q., Chen, G., & Han, S.-J. (1990). Vapor-liquid equilibria under pressure for binary systems. *Ranliao Huaxue Xuebao*, *18*(2), 185-92.

Wang, X., Chen, Q., Zhou, T., Li, H., Ding, C., & Wang, J. (2019). In-depth analysis of burning process of binary blended fuel pool fires based on liquid–vapor equilibria. *Fuel*, *256*, 115918. doi: https://doi.org/10.1016/j.fuel.2019.115918

Wang, X., He, Y., Zhou, T., Chen, Q., Ding, C., & Wang, J. (2018). Experimental study on fire behaviors of kerosene/additive blends. *Fire Technology*, *54*(6), 1841–1869. doi: 10.1007/s10694-018-0776-1

Wang, X., Zhou, T., Chen, Q., He, J., Zhang, Z., & Wang, J. (2019). Experimental study on combustion characteristics of blended fuel pool fires. *Journal of Fire Sciences*, 236-256.

Wang, X., Zhou, T. N., Chen, Q., Zhao, J. F., Ding, C., & Wang, J. (2018). Burning characteristics of azeotropic binary blended fuel pool fire. *Key Engineering Materials*, *775*, 365-370.

Waterland, L. R., Venkatesh, S., & Unnasch, S. (2003). *Safety and performance assessment of ethanol/diesel blends (E-diesel)* (Tech. Rep.). National Renewable Energy Lab., Golden, CO.(US). https://www.nrel.gov/docs/fy03osti/34817.pdf.

Wijayasinghe, M. S., & Makey, T. B. (1997). Cooking oil: A home fire hazard in Alberta, Canada. *Fire Technology*, *33*(2), 140–166.

Williams, A. (1973). Combustion of droplets of liquid fuels: A review. *Combustion and Flame*, *21*(1), 1-31. doi: https://doi.org/10.1016/0010-2180(73)90002-3

Wilson, G. M. (1964). Vapor-liquid equilibrium. XI. A new expression for the excess free energy of mixing. *Journal of the American Chemical Society*, *86*(2), 127-130.

Wood, B. D., Blackshear JR, P. L., & Eckert, E. (1971). Mass fire model: An experimental study of the heat transfer to liquid fuel burning from a sand-filled pan burner. *Combustion Science and Technology*, *4*(1), 113–129.

Yamamoto, H., Seki, N., & Fukusako, S. (1979). Forced convection heat transfer on heated bottom surface of a cavity. *Journal of Heat Transfer*, *101*, 475-479.

Yao, W., Yin, J., Hu, X., Wang, J., & Zhang, H. (2013). Numerical modeling of liquid n-heptane pool fires based on heat feedback equilibrium. *Procedia Engineering*, *62*, 377-388.

Yaws, C. (2009). *Yaws handbook of thermodynamic properties of hydrocarbons and chemicals*. New York: Knovel.

Yokoi, S. (1963). On the heights of flames from burning cribs. *Bulletin of Japan Association for Fire Science and Engineering*, *13*(1), 22-27.

Zhao, J., Huang, H., Li, Y., Jomaas, G., Wang, H., & Zhong, M. (2017). Quantitative risk assessment of continuous liquid spill fires based on spread and burning behaviours. *Applied Thermal Engineering*, *126*, 500-506. doi: https://doi.org/10.1016/j.applthermaleng.2017.07.187

Zhu, P., Tao, Z., Li, C., Liu, Q., Shao, Q., Yang, R., & Zhang, H. (2019). Experimental study on the burning rates of ethanol-gasoline blends pool fires under low ambient pressure. *Fuel*, *252*, 304-315. doi: https://doi.org/10.1016/j.fuel.2019.04.118

Zukoski, E., Cetegen, B., & Kubota, T. (1985). Visible structure of buoyant diffusion flames. *Symposium (International) on Combustion*, *20*(1), 361-366. doi: https://doi.org/10.1016/S0082-0784(85)80522-1

Zukoski, E., Kubota, T., & Cetegen, B. (1981). Entrainment in fire plumes. *Fire Safety Journal*, *3*(2), 107-121. doi: https://doi.org/10.1016/0379-7112(81)90037-0

Appendix A

Vapour-Liquid Equilibrium Data

The following equilibrium data was obtained at 101.325 kPa using the Wilson model. Binary interaction coefficients were obtained from Aspen HYSYS V10. Experimental data points shown in Figure A.1 were obtained from the NIST ThermoData Engine in Aspen Properties.

In the FDS simulations, bubble point temperature and vapour compositions were defined by fitting polynomials to the Wilson model.

$$T_b = C_1 + C_2 x_1 + C_3 x_1^2 + C_4 x_1^3 + C_5 x_1^4 + C_6 x_1^5 + C_7 x_1^6 \tag{A.1}$$

$$y_1 = \frac{\alpha x_1}{(\alpha - 1)x_1 + 1} \tag{A.2}$$

$$\alpha = C_1 + C_2 x_1 + C_3 x_1^2 + C_4 x_1^3 \tag{A.3}$$

T_b is in units of Kelvin, α is the relative volatility of the mixture, and x_1 is the mass fraction of ethanol in the liquid phase. Ethanol forms a highly nonideal liquid mixture with hexane and heptane, so for these mixtures the relative volatility was defined as:

$$\alpha = \frac{C_1}{C_2 + C_3 x_1 + C_4 x_1^2} \tag{A.4}$$

Coefficients used in Eqs. (A.1) through (A.4) are listed in Tables A.1 and A.2.

Table A.1: Polynomial Coefficients Used in FDS for Bubble-Point Temperature (K)

Mixture	C_1	C_2	C_3	C_4	C_5	C_6	C_7
Ethanol-Water	373.1	-112.9	384.7	-856.528	1141.4	-828.1	249.7
Ethanol-Isopropanol	354.8	-2.00	-1.95	0.565	0.143	-0.064	0.0085
Ethanol-Hexane	339.2	-153.0	1094.7	-3661.6	6230.5	-5223.7	1725.5
Ethanol-Heptane ($x_1 \leq 0.0212$)	371.5	-2287	1.27×10^5	-4.29×10^6	6.26×10^7	0	0
Ethanol-Heptane ($x_1 \leq 0.1298$)	364.5	-985.6	2.4937×10^4	-3.6634×10^5	3.1192×10^6	-1.4232×10^7	2.6864×10^7
Ethanol-Heptane ($x_1 > 0.1298$)	347.3	-31.43	154.6	-422.6	645.3	-514.1	172.2

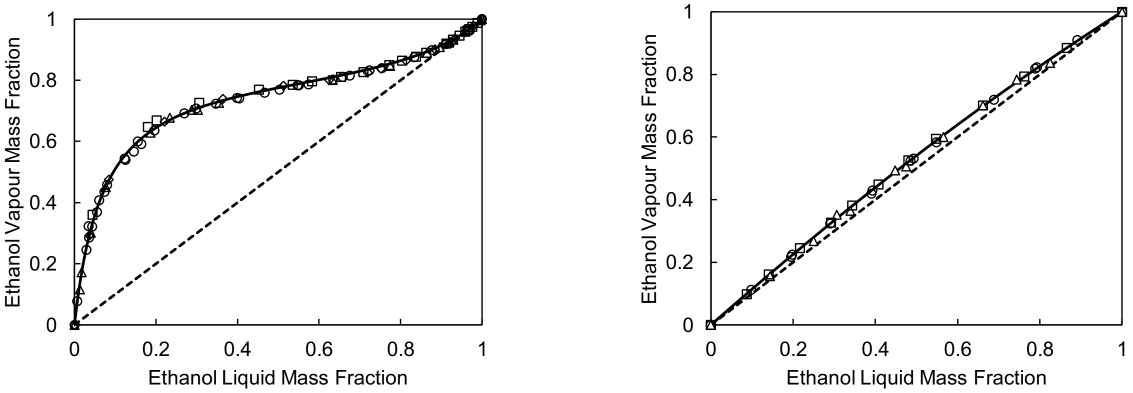

(a) Data for ethanol-water mixtures. Rieder and Thompson (1949) [○], Kojima et al. (1969) [△], Kamihama et al. (2012), [□], Lai et al. (2014), [◇].

(b) Data for ethanol-isopropanol mixtures. Ballard and Winkle (1952) [○], Kojima et al. (1969) [△], Li et al. (2000), [□].

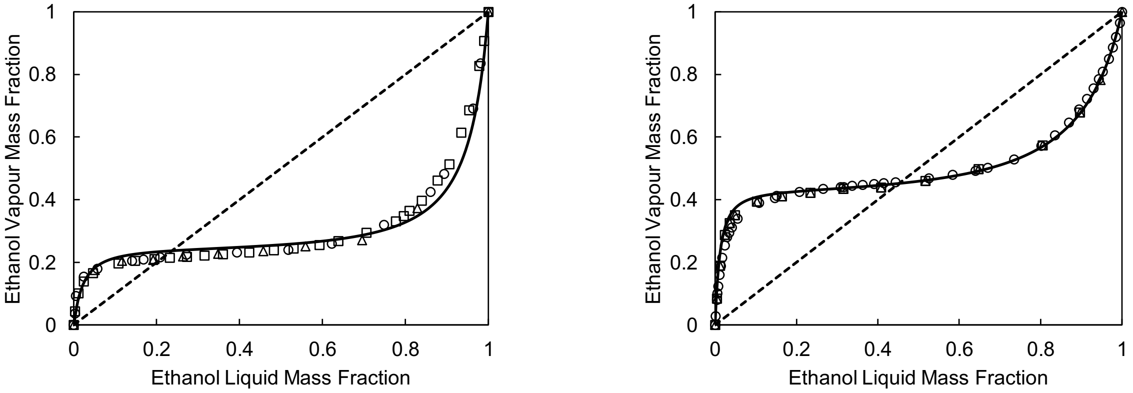

(c) Data for ethanol-hexane mixtures. Sinor and Weber (1960) [○], Kudryavtseva and Susarev (1963) [△], Ortega and Espiau (2003), [□].

(d) Data for ethanol-heptane mixtures. Ortega and Espiau (2003) [○], Van Ness et al. (1967) [△], Q. Wang et al. (1990), [□].

Figure A.1: x-y diagrams for ethanol-water, ethanol-isopropanol, ethanol-hexane, and ethanol-heptane mixtures at 101.325 kPa using the Wilson model.

Table A.2: Polynomial Coefficients Used in FDS Simulations for Relative Volatility of Binary Mixtures

Mixture	C_1	C_2	C_3	C_4
Ethanol-Water	11.647	-27.739	27.632	-10.849
Ethanol-Isopropanol	1.565	0.0471	-0.0105	0.0043
Ethanol-Hexane	0.1820	0.0175	0.5448	1.1283
Ethanol-Heptane	0.1505	0.0042	0.1625	0.3749

Appendix B

Steady-State Concentration Estimation

The concentration of fuel inside the pan is predicted through a mass balance around the system, which is shown in Figure B.1. It is assumed that the pool is well-mixed.

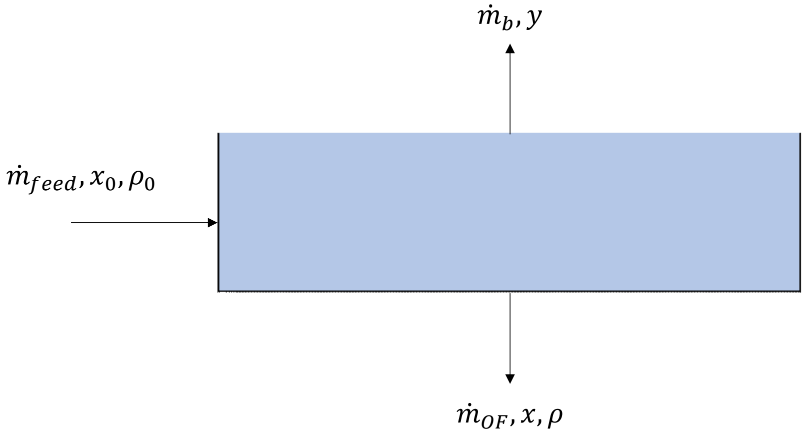

Figure B.1: Mass balance for a continuously fed pool fire with an overflow outlet.

The burning rate was computed using the correlation of Babrauskas (1983) (see Eqs. (2.3) and (4.7)). The change in mass over time of the pool and individual species are given by the following equations:

$$\frac{dm}{dt} = \dot{m}_{feed} - \dot{m}_b \tag{B.1}$$

$$\frac{dm_i}{dt} = \dot{m}_{feed} x_{0,i} - \dot{m}_b y_i \tag{B.2}$$

An explicit Euler's method was used to track the mass of the fuel in the pan. Here, j will be used to indicate the value at the current time step. For this part of the calculation, it is assumed that the liquid accumulates in the pan, which yields an intermediate new mass of each species ($m_{i,new}$):

$$m_{new} = m_j + (\dot{m}_{feed} - \dot{m}_b)\Delta t \tag{B.3}$$

$$m_{i,new} = m_{i,j} + (\dot{m}_{feed} x_{0,i} - \dot{m}_b y_{i,j})\Delta t \tag{B.4}$$

$$x_{i,j+1} = \frac{m_{i,new}}{m_{new}} \tag{B.5}$$

The density and volume of the new mixture is then calculated using the mass and composition of the pool:

$$\rho = \frac{1}{\sum_{i=1}^{N} x_{i,j+1}/\rho_i} \tag{B.6}$$

$$V = \frac{m_{new}}{\rho} \tag{B.7}$$

The final volume and mass are updated after the overflow is subtracted from the mass of the pool:

$$m_{j+1} = m_{new} - \rho(V - V_{pan}) \tag{B.8}$$

$$m_{i,j+1} = m_{i,new} - \rho(V - V_{pan}) x_{i,j+1} \tag{B.9}$$

A steady-state pool fire experiment was conducted with an ethanol-water mixture that was initially 35.5% ethanol by mass. The feed rate was set to $1.2\,\mathrm{g\,s^{-1}}$ and had the same initial concentration as the pool. The tip of the overflow tube was 2 cm above the bottom of the pan ($V_{pan} = 1.4\,\mathrm{L}$). Overflow samples were taken every 180 seconds. The results in Figure B.2 demonstrate that the model gives an appropriate estimate of the composition of the pool over time. In this specific case, the pool reaches a steady-state concentration around 1500-1800 seconds (25-30 min) after ignition. The model slightly underpredicts the final concentration observed in the experiment. This is because the burning rate model overpredicts the burning rate. Additionally, the pool in the experiment is not perfectly mixed, so the model will tend to overestimate the concentration of ethanol at the pool surface.

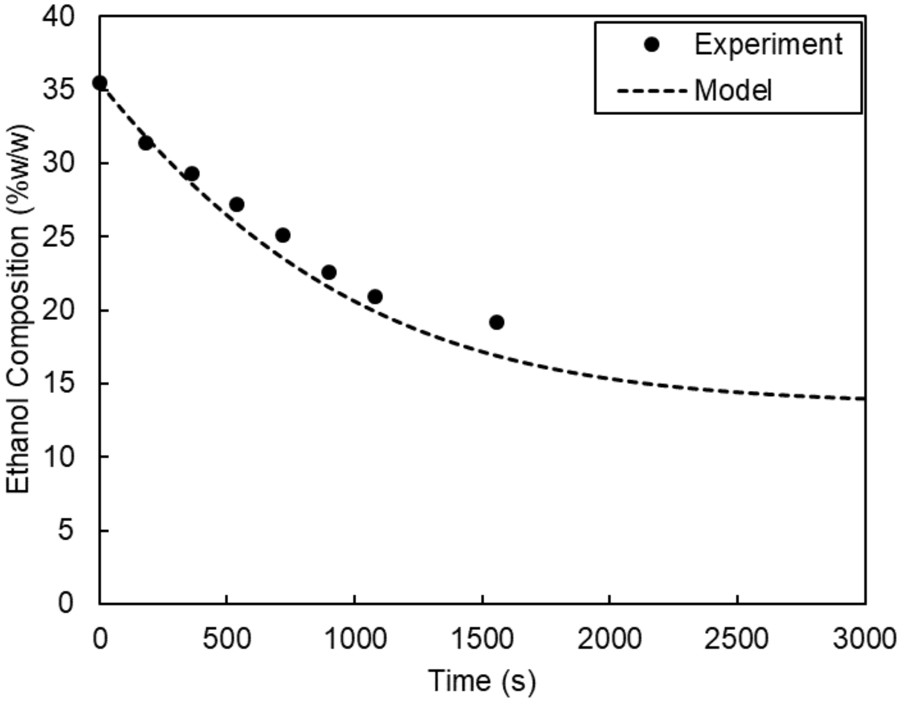

Figure B.2: Change in ethanol composition over time in a continuously fed 35% w/w ethanol-water pool fire.

Appendix C

Flame Height

The general procedure involves converting a video into several frames and measuring the flame height in each individual frame. To automate the process, the flame is contoured and the height between the lowest and highest part of the contour is taken as the flame height. The thresholding algorithm was manually tuned to contour the flames using the HSV (hue, saturation, value) scheme. Each parameter was bounded to contain pixels within the yellow to red colour spectrum with high intensity and low saturation. Colour thresholding parameters are listed in Table C.1. A visual example for a single frame is demonstrated in Figure C.1.

Table C.1: Colour Thresholding Parameters for Flame Height Image Processing

Parameter	Minimum	Maximum
Hue	0.697	0.176
Saturation	0.000	0.493
Value	0.918	1.000

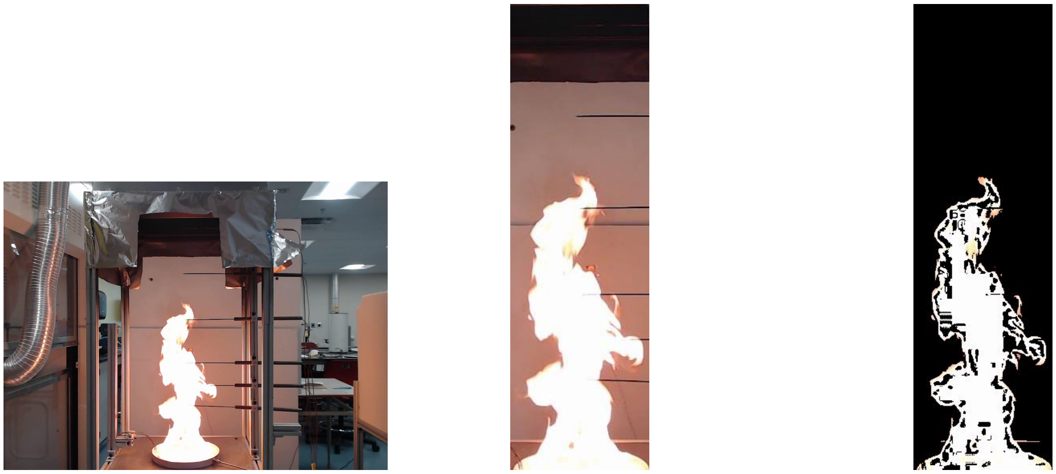
(a) Video frame (b) Cropped frame (c) Thresholded contour

Figure C.1: Image processing sequence for measuring flame heights.

The image processing procedure is as follows:

1. Input the pixel-to-distance ratio using the pan diameter as a reference
2. Convert the video to individual frames
3. Crop every 15th frame to contain the region where only the pan and flame are present
4. For all cropped frames, apply the thresholding algorithm to contour the flame
5. Record the distance between the lowest and highest part of the contour

All flame height measurements were then grouped into "bins" at 2.5 cm intervals. A flame height intermittency plot was created from these bins, and the mean flame height was taken as the height where the flame was 50% intermittent. An example of this plot is given in Figure C.2.

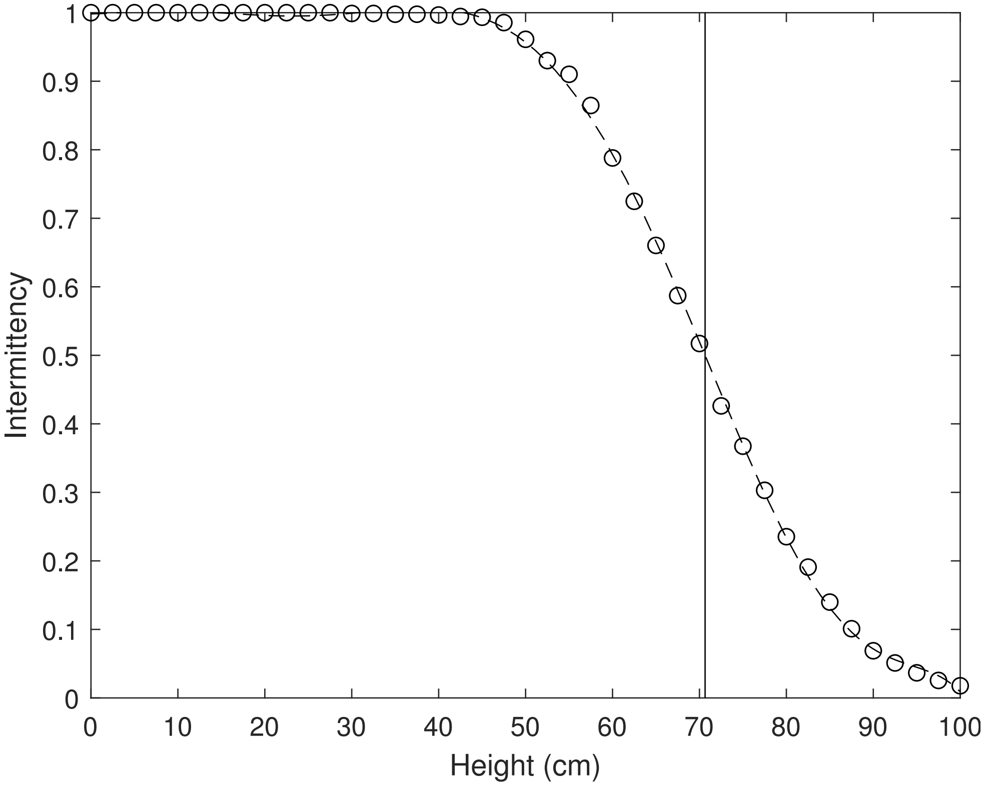

Figure C.2: Flame height intermittency plot for a continuously fed isopropanol pool fire.

Appendix D

Experimental Data

D.1 Instantaneous Gas Temperatures

The following gas temperatures are not corrected for radiation losses.

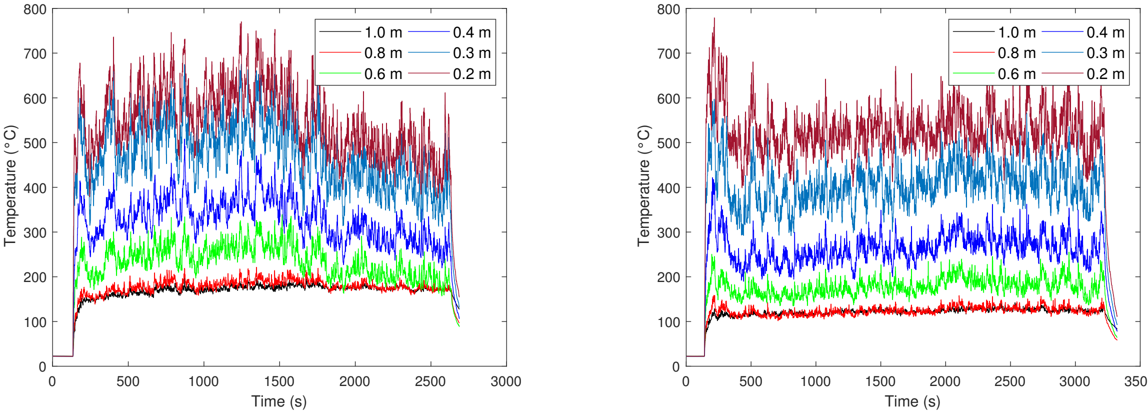

(a) 100 %w/w Ethanol (Dalhousie)

(b) 85-15 %w/w Ethanol-Water

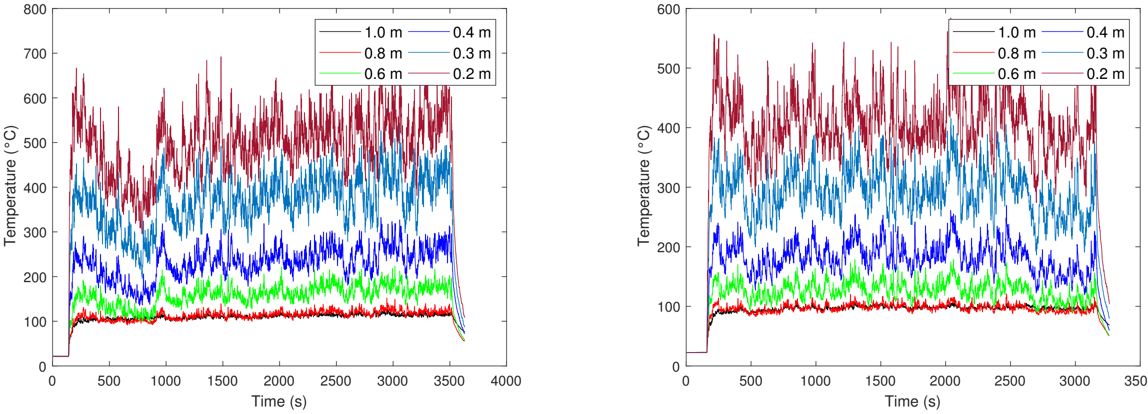

(c) 70-30% w/w Ethanol-Water

(d) 50-50% w/w Ethanol-Water

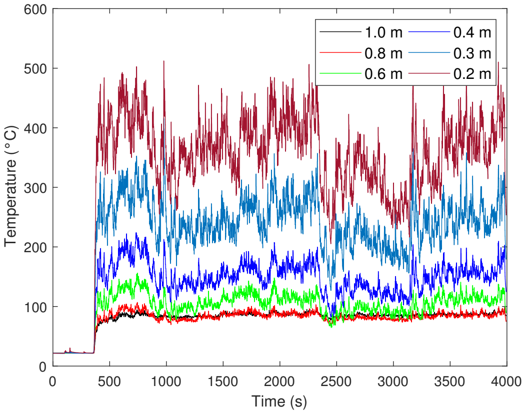

(e) 35-65% w/w Ethanol-Water

Figure D.1: Instantaneous gas temperatures for continuously fed ethanol-water pool fires.

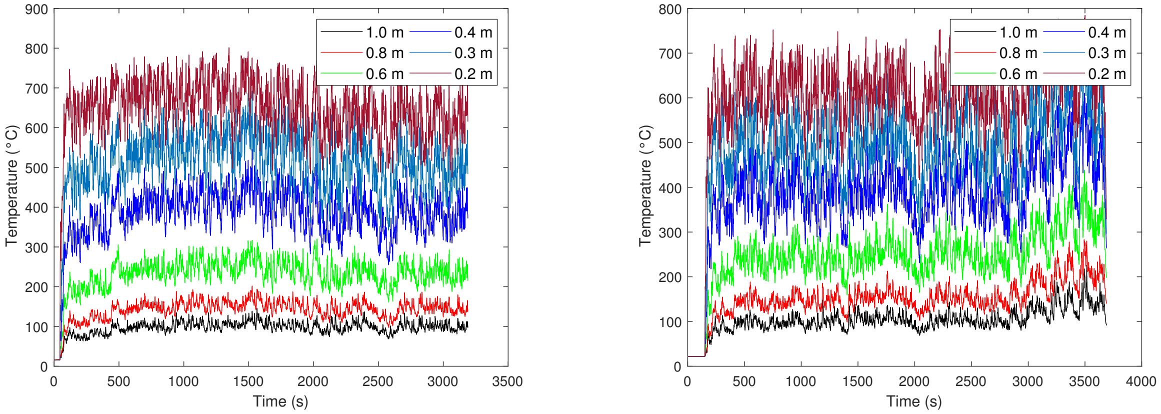

(a) 85-15% w/w Ethanol-Isopropanol (b) 70-30% w/w Ethanol-Isopropanol

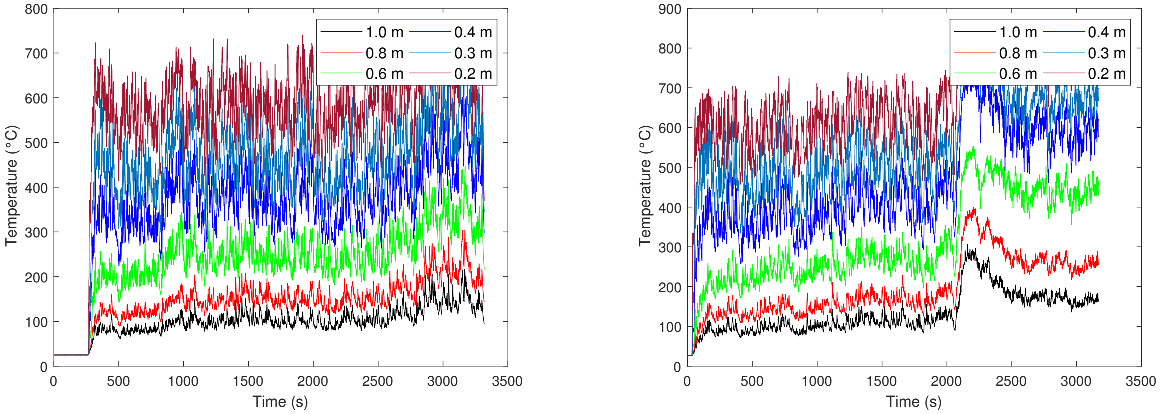

(c) 50-50% w/w Ethanol-Isopropanol (d) 30-70% w/w Ethanol-Isopropanol

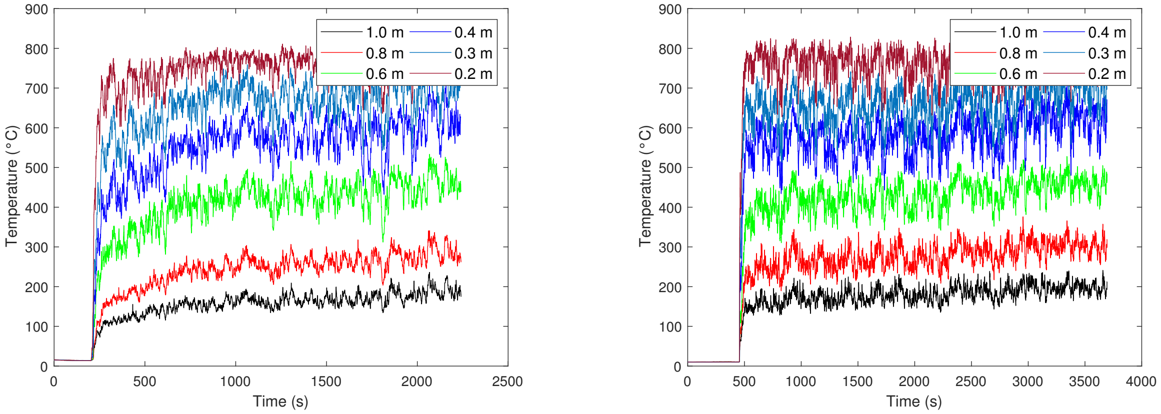

(e) 15-85% w/w Ethanol-Isopropanol (f) 100% w/w Isopropanol

Figure D.2: Instantaneous gas temperatures for continuously fed ethanol-isopropanol pool fires.

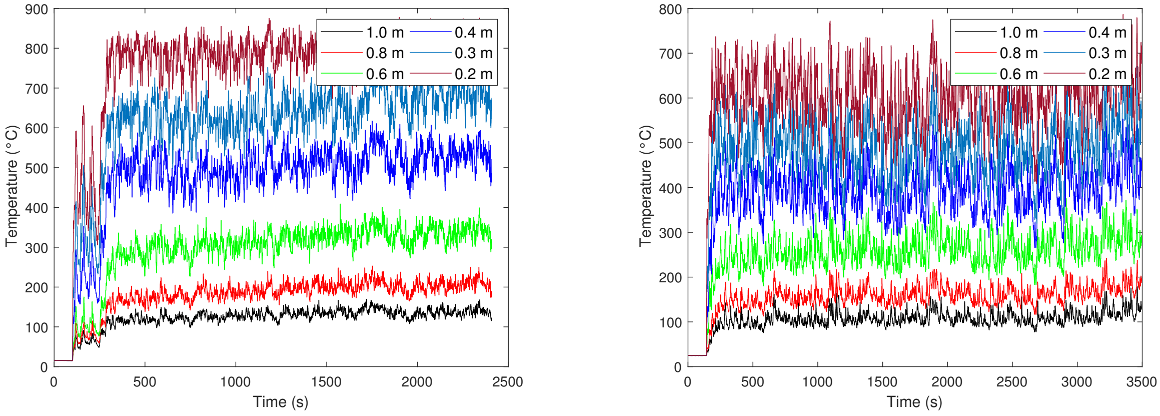

(a) 100 %w/w Ethanol (Damage Control School)

(b) 90-10% w/w Ethanol-Hexane

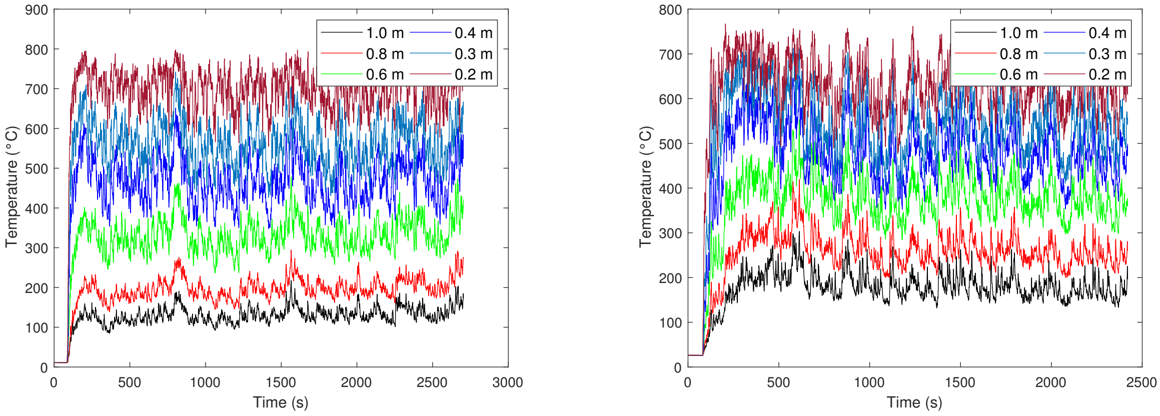

(c) 80-20% w/w Ethanol-Hexane

(d) 70-30% w/w Ethanol-Hexane

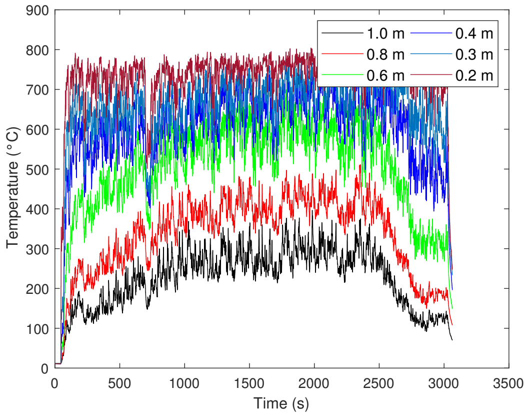

(e) 50-50% w/w Ethanol-Hexane

Figure D.3: Instantaneous gas temperatures for continuously fed ethanol-hexane pool fires.

D.2 Time-Averaged Gas Temperatures

The following gas temperatures are not corrected for radiation losses.

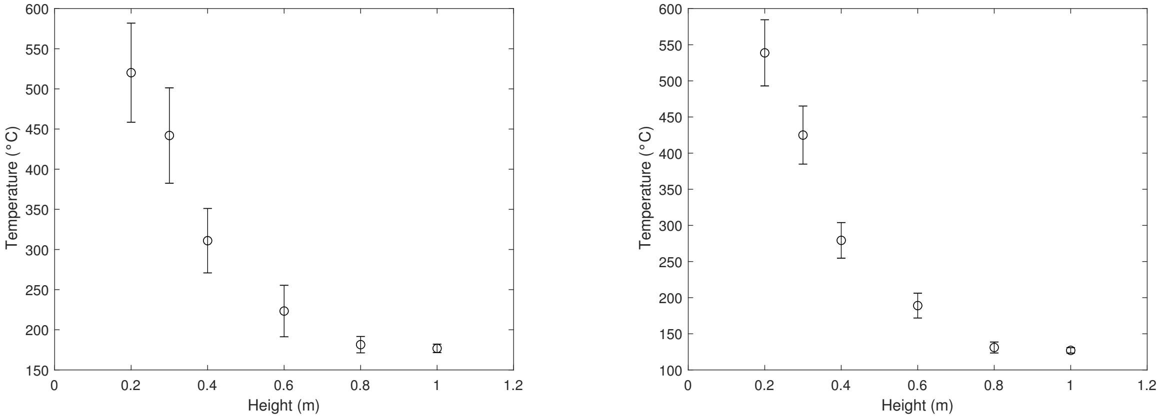

(a) 100 %w/w Ethanol (Dalhousie) (b) 85-15 %w/w Ethanol-Water

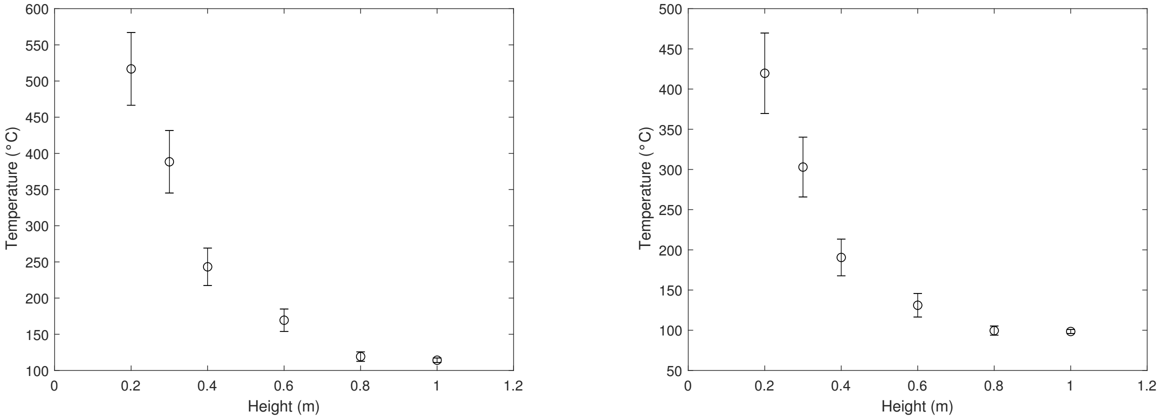

(c) 70-30% w/w Ethanol-Water (d) 50-50% w/w Ethanol-Water

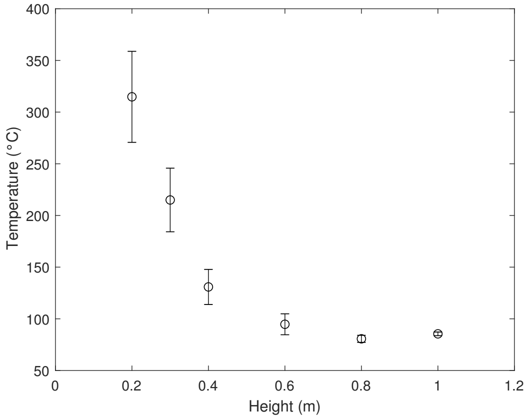

(e) 35-65% w/w Ethanol-Water

Figure D.4: Time-averaged gas temperatures for continuously fed ethanol-water pool fires. Error bars indicate one standard deviation over the time-averaging interval.

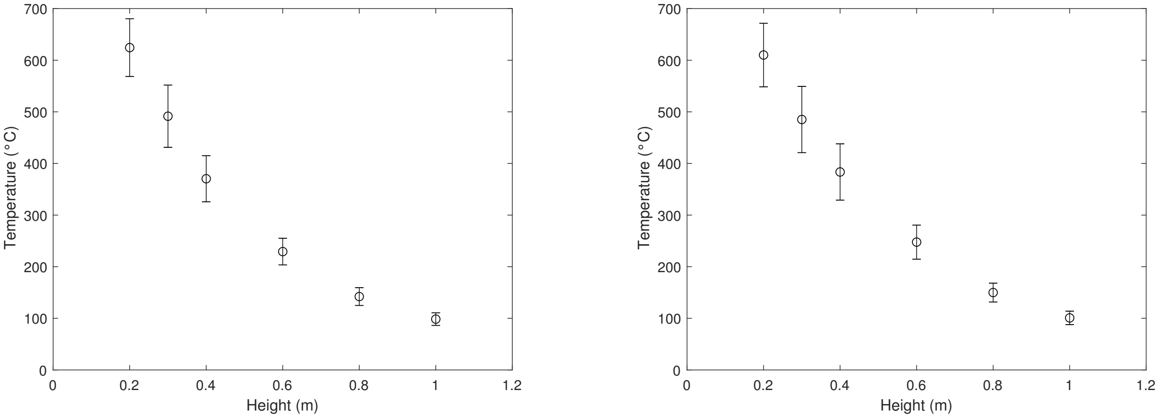

(a) 85-15% w/w Ethanol-Isopropanol

(b) 70-30% w/w Ethanol-Isopropanol

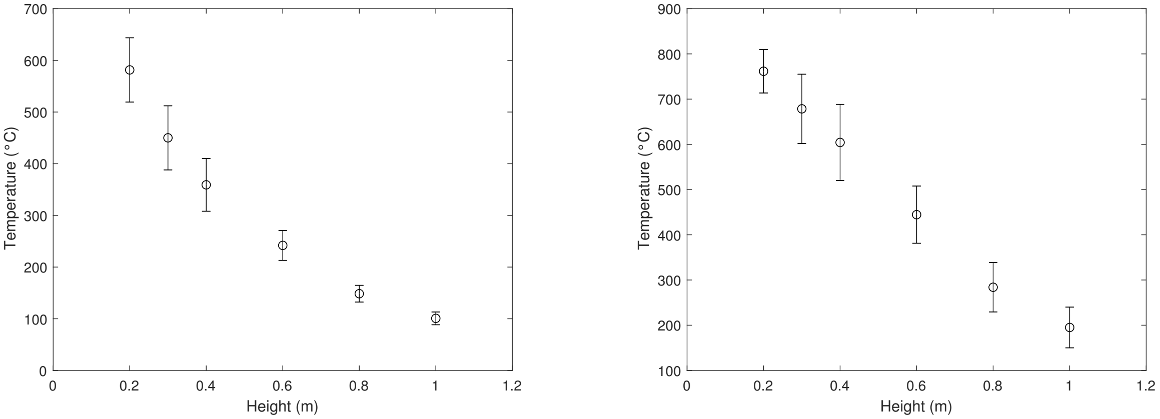

(c) 50-50% w/w Ethanol-Isopropanol

(d) 30-70% w/w Ethanol-Isopropanol

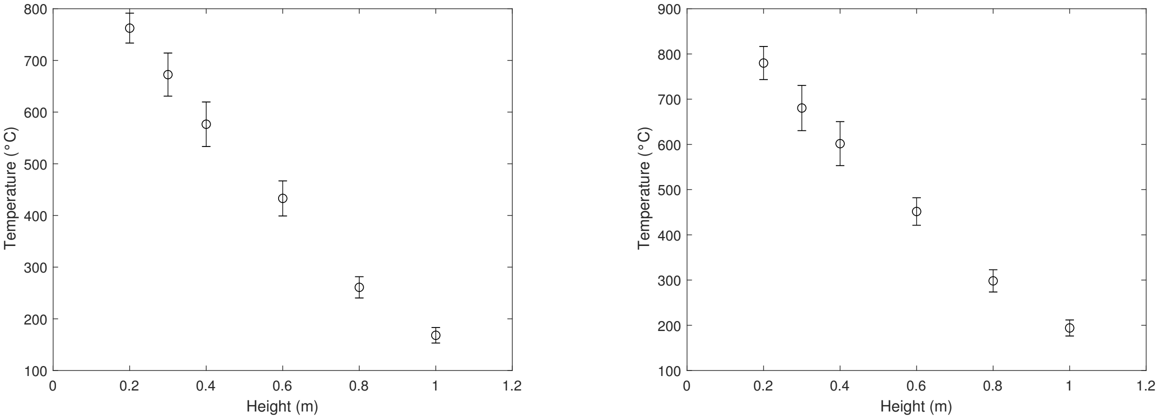

(e) 15-85% w/w Ethanol-Isopropanol

(f) 100% w/w Isopropanol

Figure D.5: Time-averaged gas temperatures for continuously fed ethanol-isopropanol pool fires. Error bars indicate one standard deviation over the time-averaging interval.

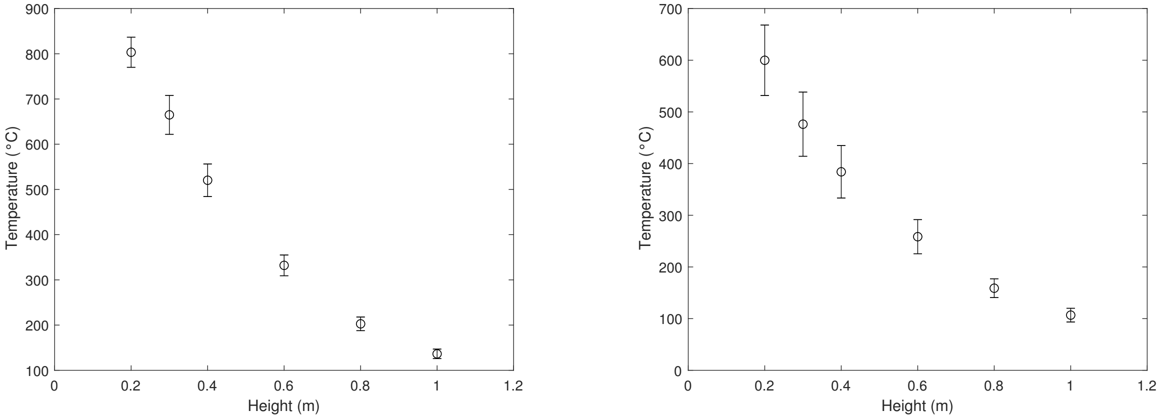

(a) 100 %w/w Ethanol (Damage Control School)

(b) 90-10% w/w Ethanol-Hexane

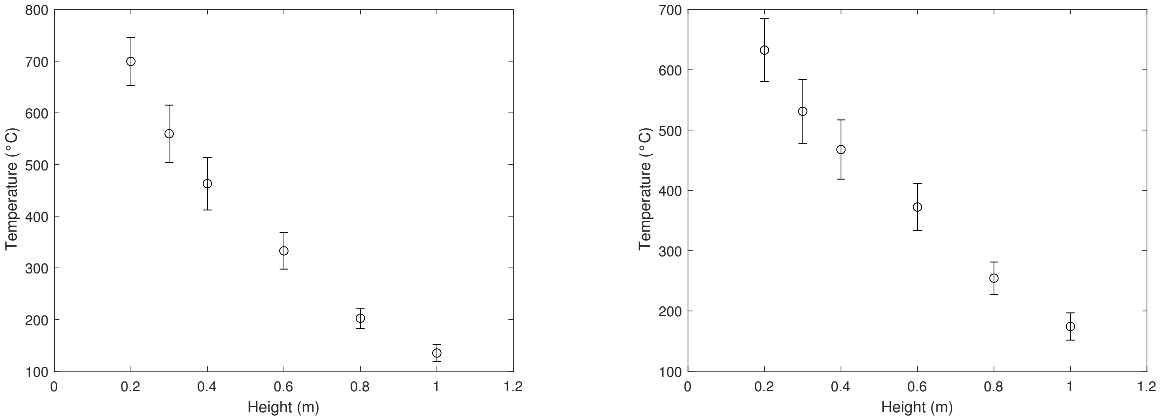

(c) 80-20% w/w Ethanol-Hexane

(d) 70-30% w/w Ethanol-Hexane

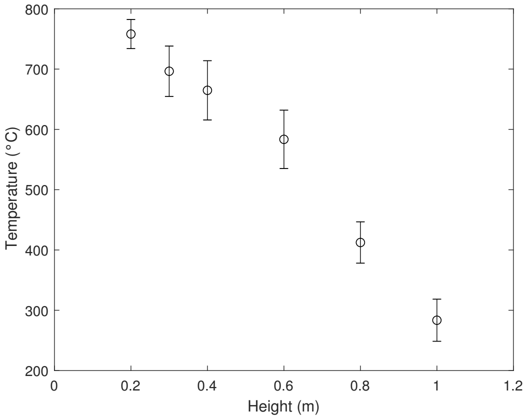

(e) 50-50% w/w Ethanol-Hexane

Figure D.6: Time-averaged gas temperatures for continuously fed ethanol-hexane pool fires. Error bars indicate one standard deviation over the time-averaging interval.

D.3 Liquid Temperatures

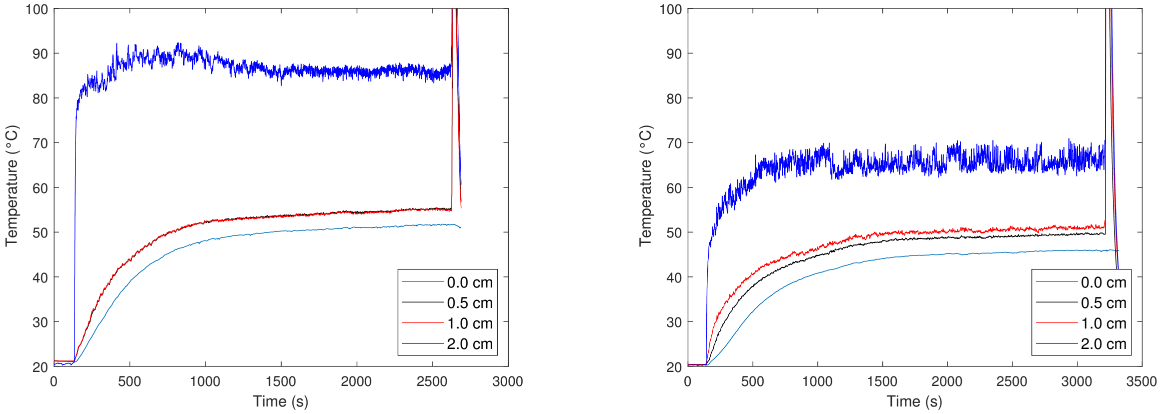

(a) 100-0% w/w Ethanol-Water

(b) 85-15% w/w Ethanol-Water

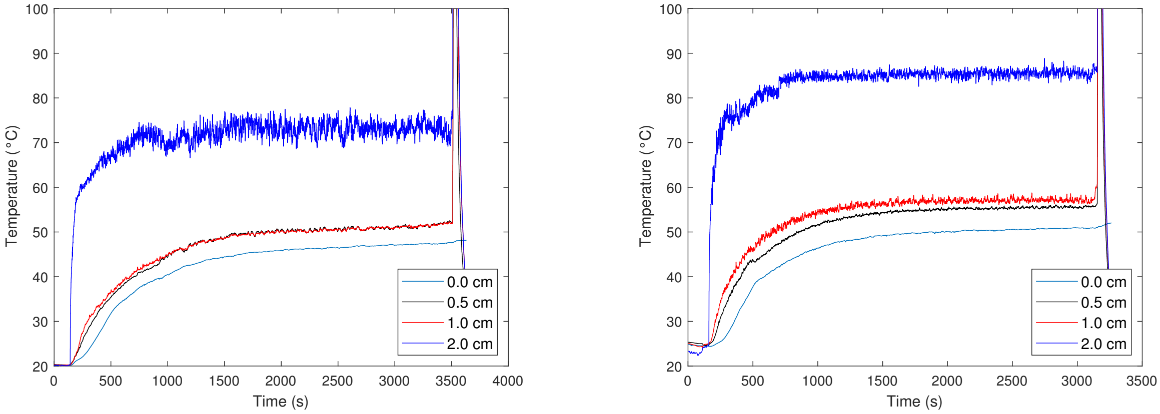

(c) 70-30% w/w Ethanol-Water

(d) 50-50% w/w Ethanol-Water

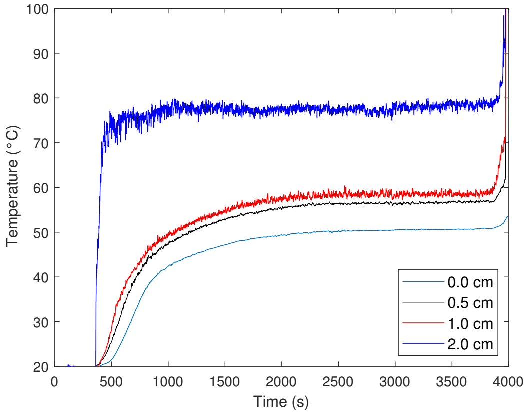

(e) 35-65% w/w Ethanol-Water

Figure D.7: Liquid temperatures for continuously fed ethanol-water pool fires.

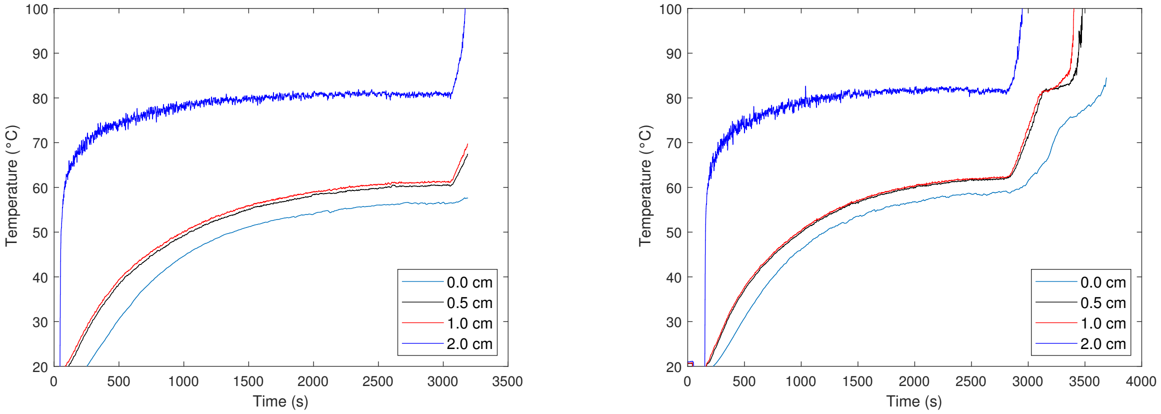

(a) 85-15% w/w Ethanol-Isopropanol

(b) 70-30% w/w Ethanol-Isopropanol

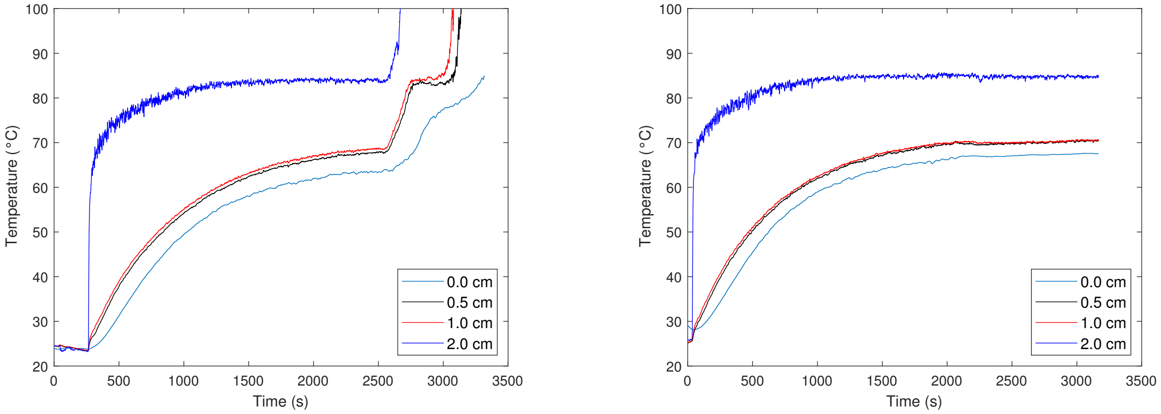

(c) 50-50% w/w Ethanol-Isopropanol

(d) 30-70% w/w Ethanol-Isopropanol

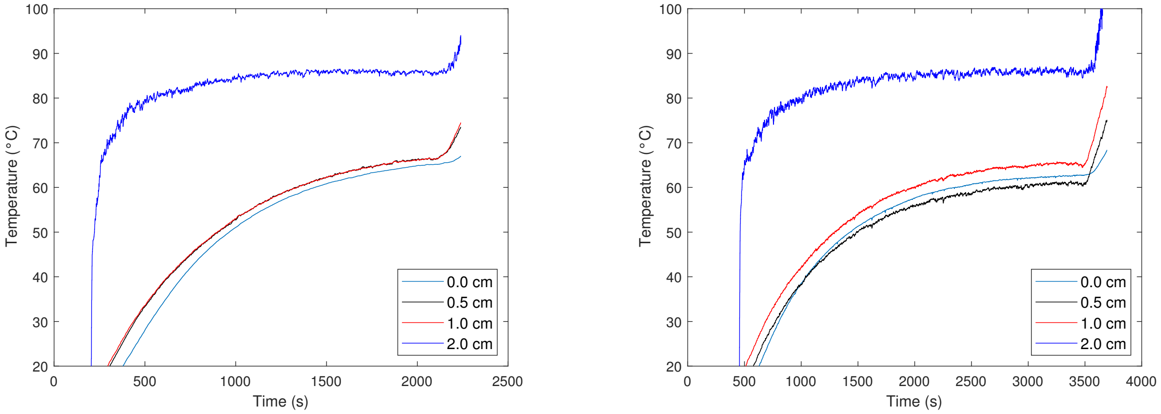

(e) 15-85% w/w Ethanol-Isopropanol

(f) 100% w/w Isopropanol

Figure D.8: Liquid temperatures for continuously fed ethanol-isopropanol pool fires.

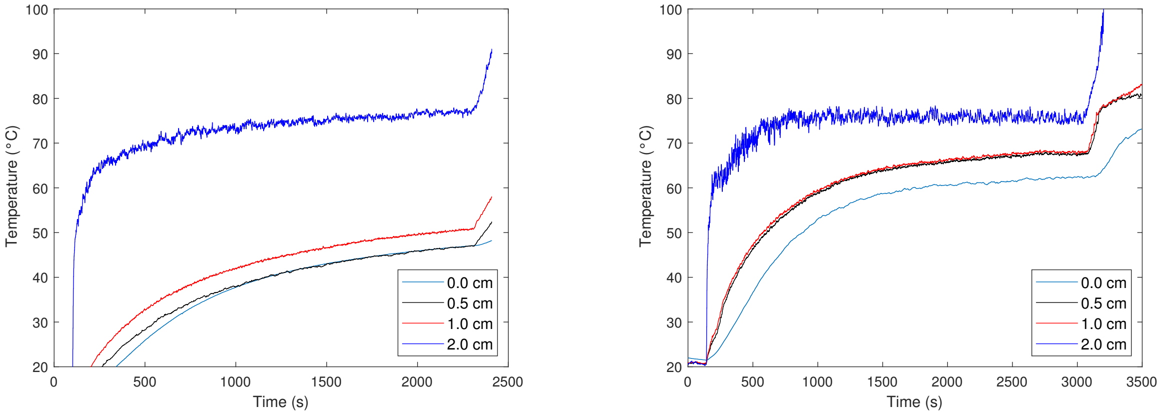

(a) 100% w/w Ethanol (Damage Control School)

(b) 90-10% w/w Ethanol-Hexane

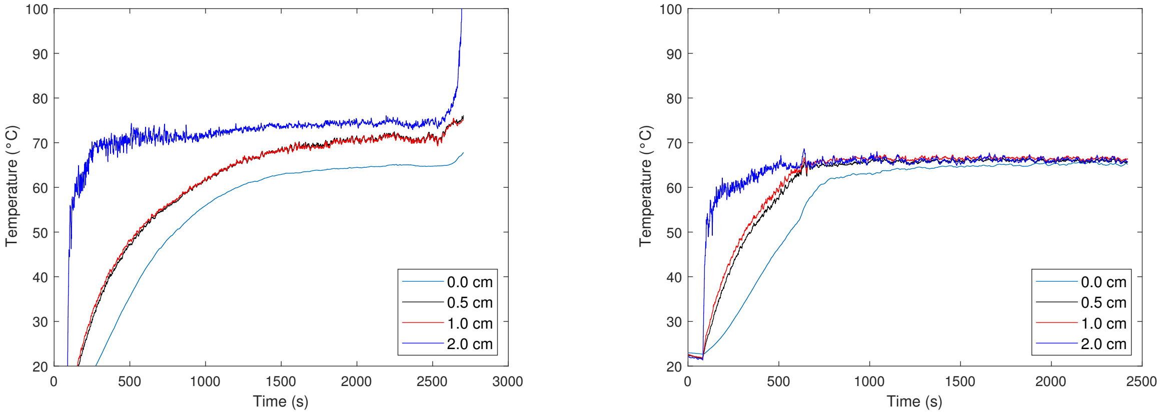

(c) 80-20% w/w Ethanol-Hexane

(d) 70-30% w/w Ethanol-Hexane

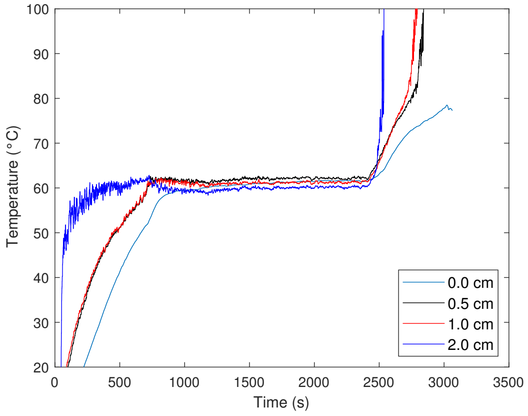

(e) 50-50% w/w Ethanol-Hexane

Figure D.9: Liquid temperatures for continuously fed ethanol-hexane pool fires.

D.4 Burning Rates

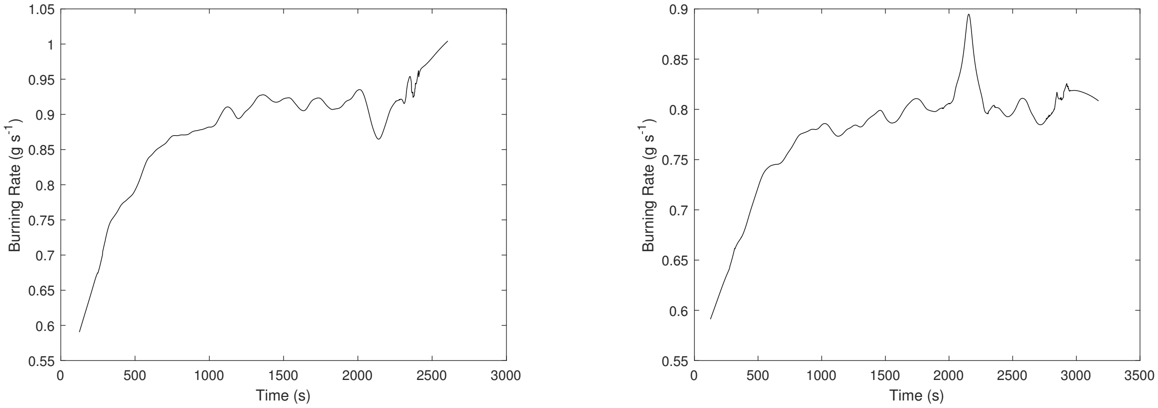

(a) 100-0% w/w Ethanol-Water (Dalhousie)

(b) 85-15% w/w Ethanol-Water

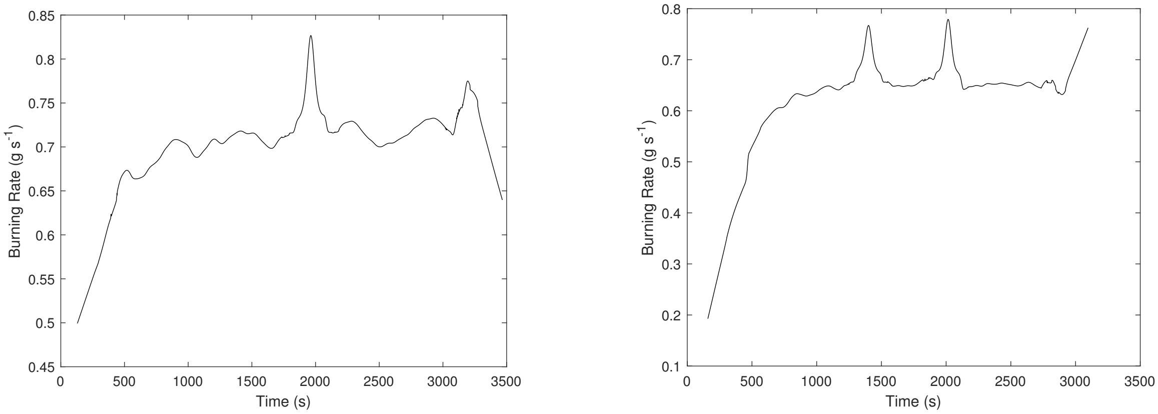

(c) 70-30% w/w Ethanol-Water

(d) 50-50% w/w Ethanol-Water

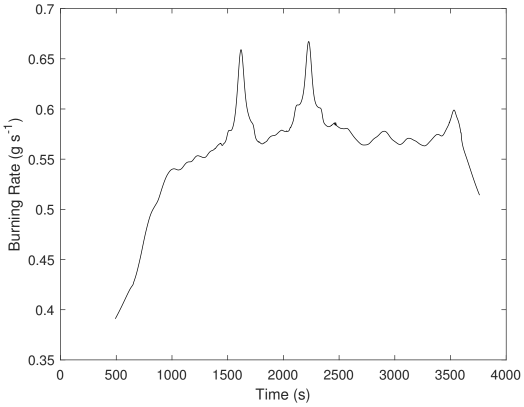

(e) 35-65% w/w Ethanol-Water

Figure D.10: Burning rates for continuously fed ethanol-water pool fires.

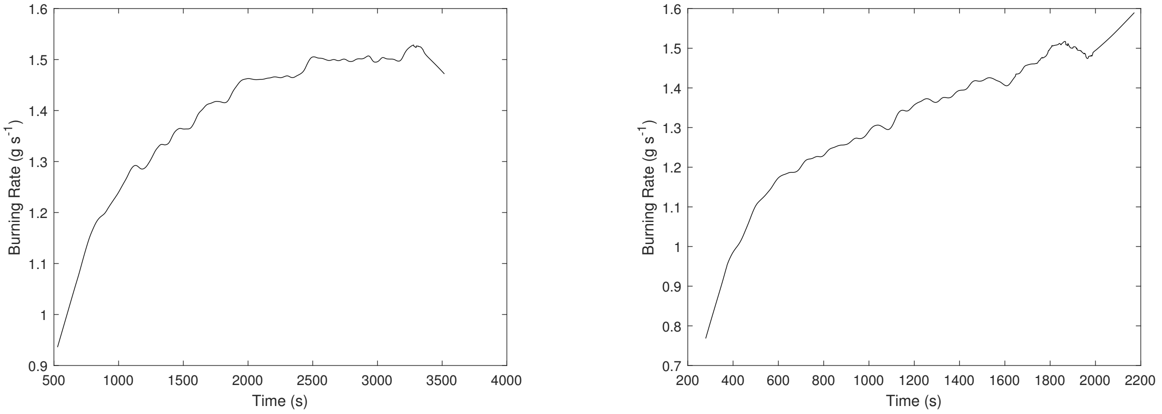

(a) 100% w/w Isopropanol

(b) 15-85% w/w Ethanol-Isopropanol

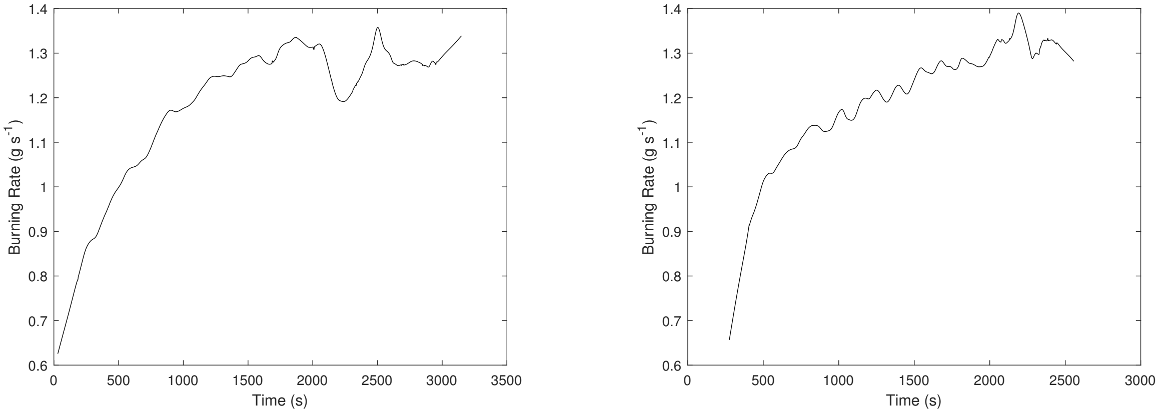

(c) 30-70% w/w Ethanol-Isopropanol

(d) 50-50% w/w Ethanol-Isopropanol

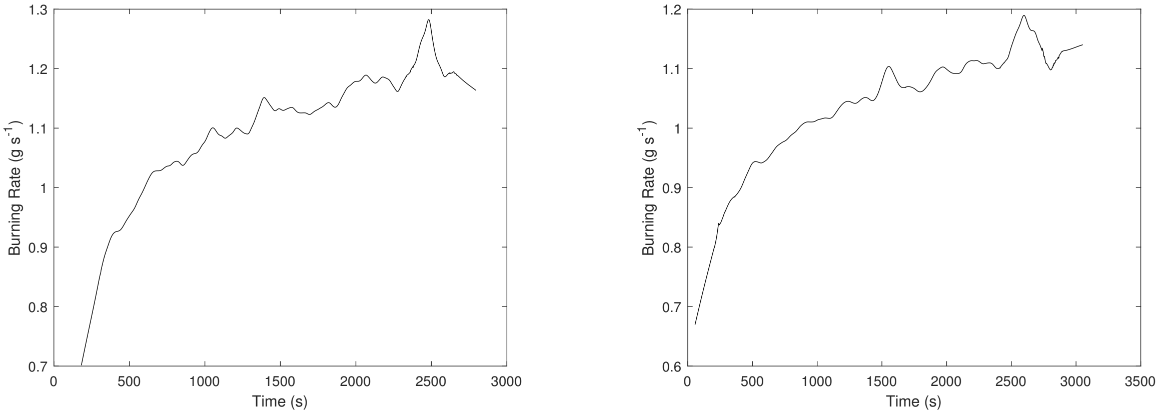

(e) 70-30% w/w Ethanol-Isopropanol

(f) 85-15% w/w Ethanol-Isopropanol

Figure D.11: Burning rates for continuously fed ethanol-isopropanol pool fires.

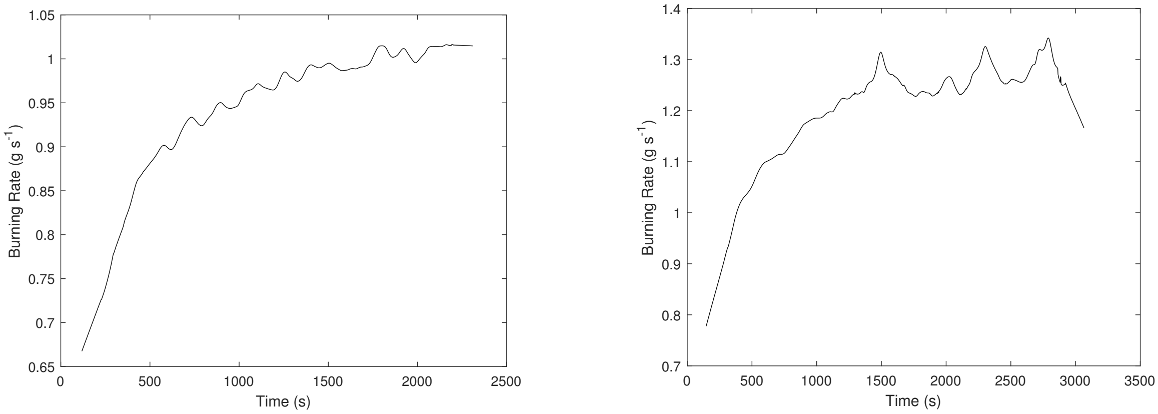

(a) 100-0% w/w Ethanol (Damage Control School)

(b) 90-10% w/w Ethanol-Hexane

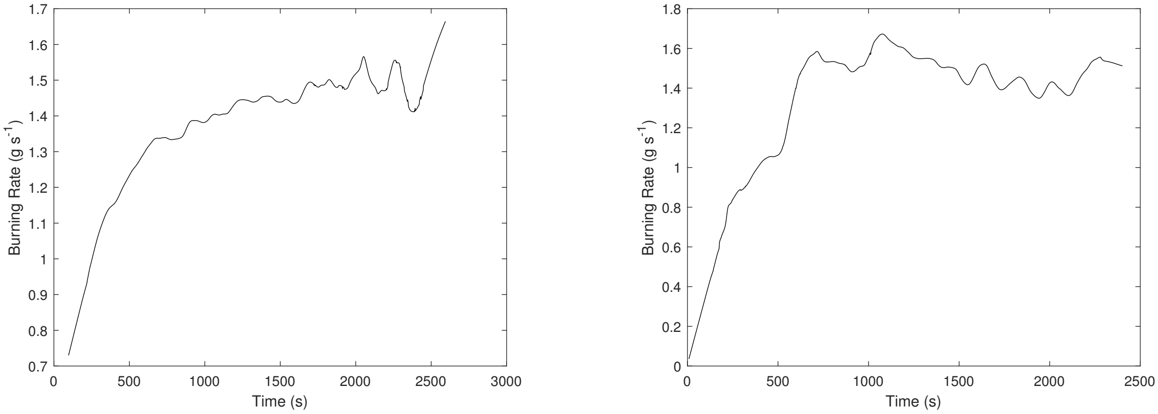

(c) 80-20% w/w Ethanol-Hexane

(d) 70-30% w/w Ethanol-Hexane

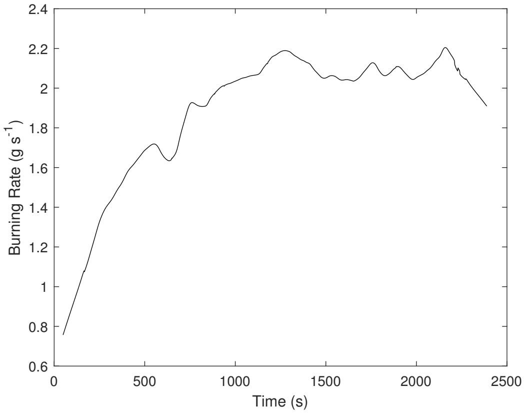

(e) 50-50% w/w Ethanol-Hexane

Figure D.12: Burning rates for continuously fed ethanol-hexane pool fires.

D.5 Flame Heights

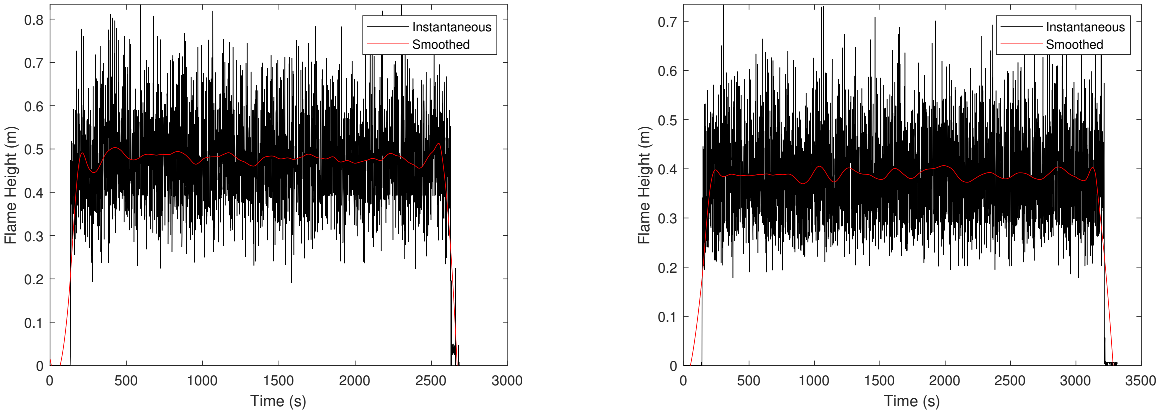

(a) 100-0% w/w Ethanol-Water (Dalhousie)

(b) 85-15% w/w Ethanol-Water

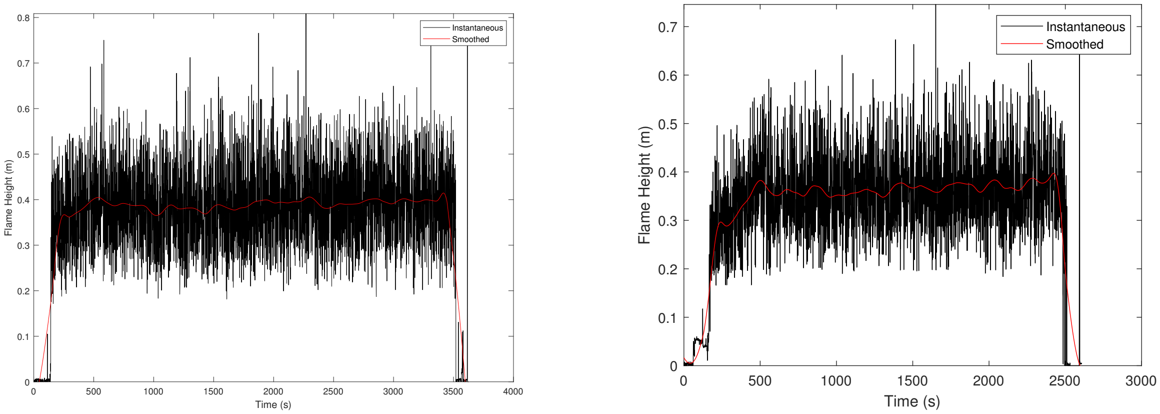

(c) 70-30% w/w Ethanol-Water

(d) 50-50% w/w Ethanol-Water

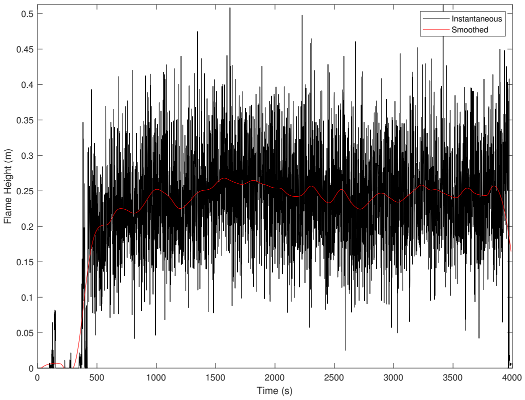

(e) 35-65% w/w Ethanol-Water

Figure D.13: Flame heights for continuously fed ethanol-water pool fires.

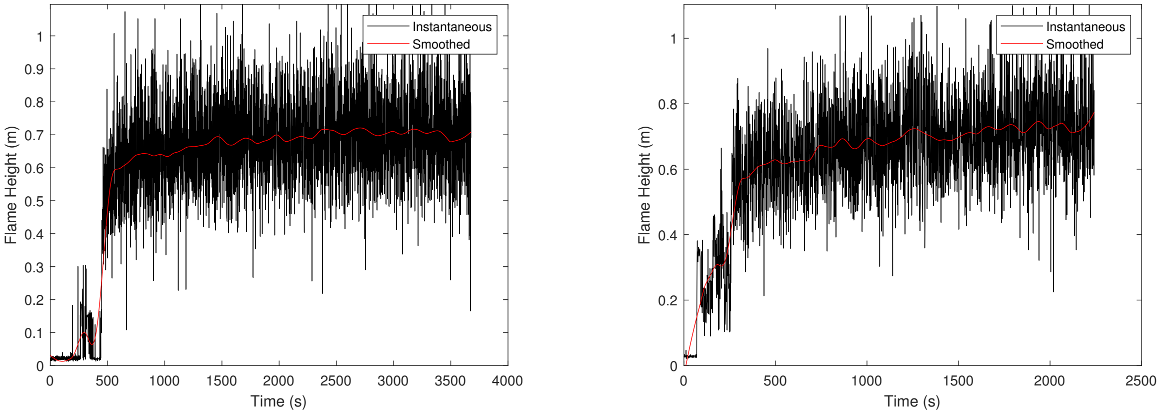

(a) 100% w/w Isopropanol

(b) 15-85% w/w Ethanol-Isopropanol

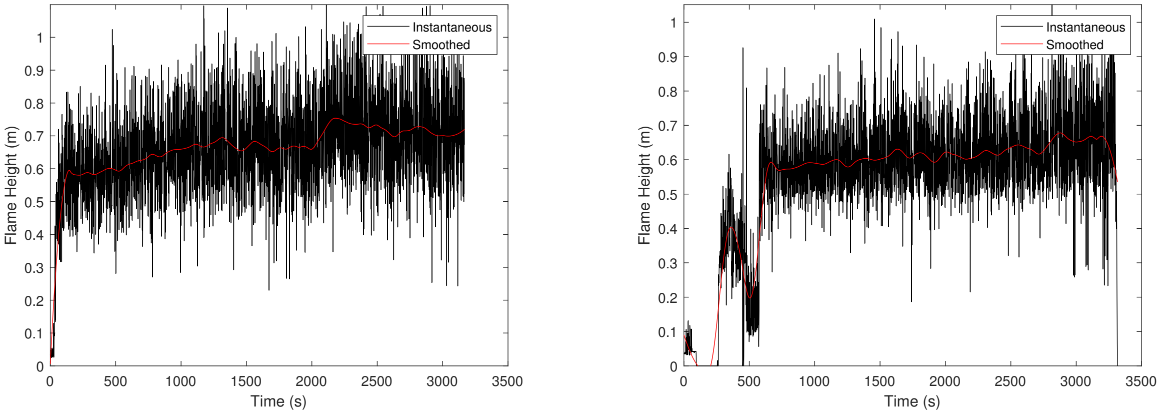

(c) 30-70% w/w Ethanol-Isopropanol

(d) 50-50% w/w Ethanol-Isopropanol

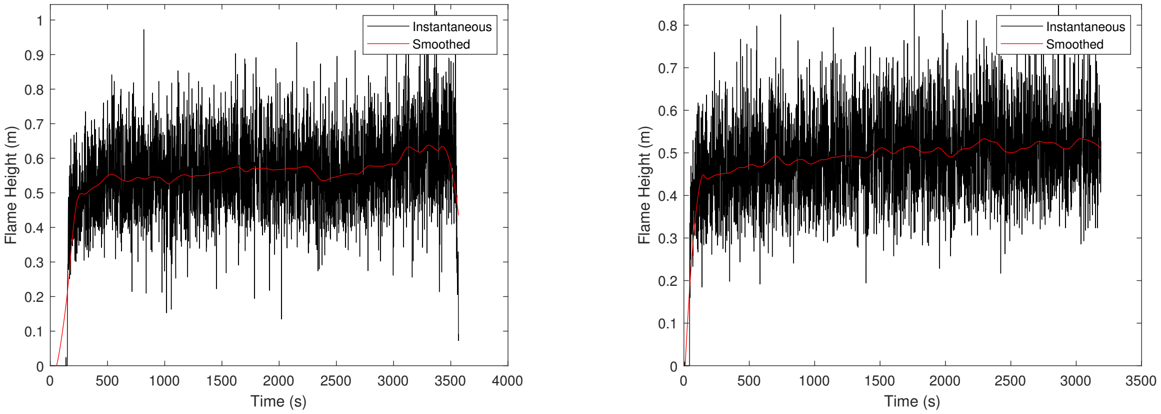

(e) 70-30% w/w Ethanol-Isopropanol

(f) 85-15% w/w Ethanol-Isopropanol

Figure D.14: Flame heights for continuously fed ethanol-isopropanol pool fires.

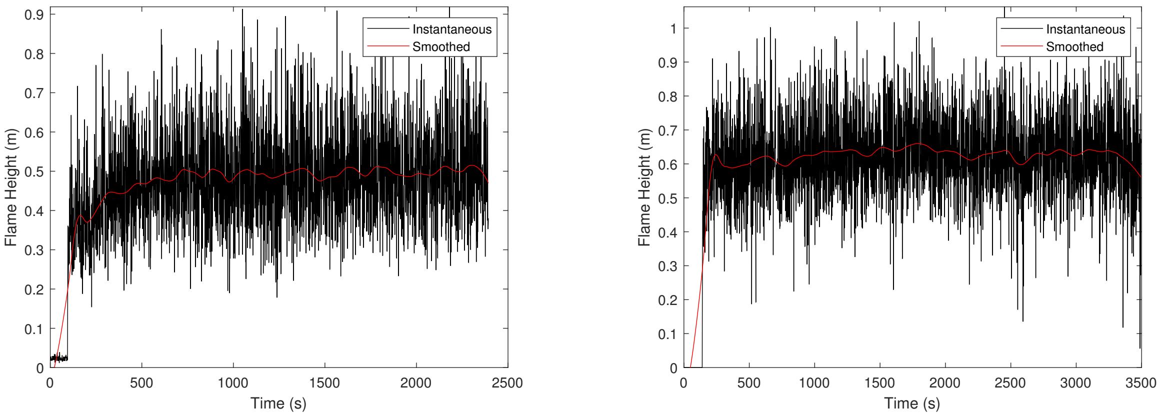

(a) 100-0% w/w Ethanol (Damage Control School)

(b) 90-10% w/w Ethanol-Hexane

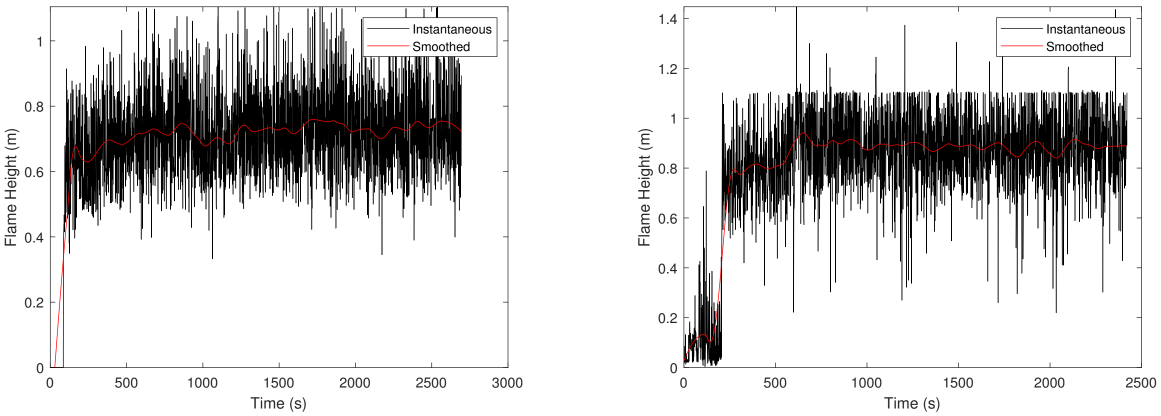

(c) 80-20% w/w Ethanol-Hexane

(d) 70-30% w/w Ethanol-Hexane

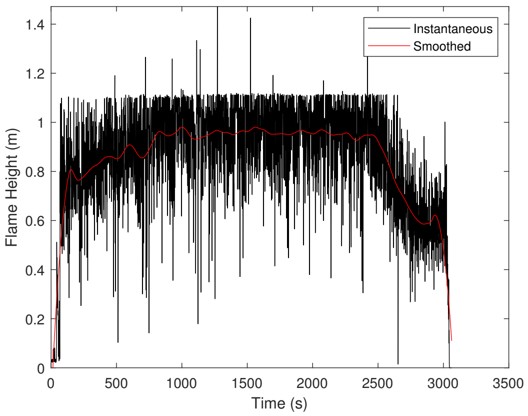

(e) 50-50% w/w Ethanol-Hexane

Figure D.15: Flame heights for continuously fed ethanol-hexane pool fires.

Appendix E

Thermo-Physical Properties

Vapour pressures were calculated using the extended Antoine equation, denoted by:

$$\ln P^{sat} = C_1 + C_2/T + C_3 \ln T + C_4 T^{C_5} \tag{E.1}$$

where P^{sat} is vapour pressure in Pa and T is temperature in K. Constants were obtained from Perry's Chemical Engineers' Handbook (Green & Perry, 2007) and are summarized in Table E.1.

Liquid densities were calculated using the following equation for all species except water:

$$\rho = C_1 / C_2^{[1+(1-T/C_3)^{C_4}]} \tag{E.2}$$

The following equation was used to estimate the density of liquid water:

$$\rho = C_1 + C_2 T + C_3 T^2 + C_4 T^3 \tag{E.3}$$

where ρ is in mol/dm^3 and T is in K. Constants were taken from Perry's Chemical Engineers' Handbook (Green & Perry, 2007) and are summarized in Table E.2.

Liquid heat capacities for all species except heptane were calculated from the following equations:

Table E.1: Constants for the Extended Antoine Equation for Vapour Pressures of Pure Species

Species	C_1	C_2	C_3	C_4	C_5
Ethanol	73.304	-7122.3	-7.1424	2.8853×10^{-6}	2
Heptane	87.829	-6996.4	-9.8802	7.2099×10^{-6}	2
Hexane	104.65	-6995.5	-12.702	1.2381×10^{-5}	2
Isopropanol	96.094	-8575.4	-10.292	1.6665×10^{-17}	6
Water	73.649	-7258.2	-7.3037	4.1653×10^{-6}	2

Table E.2: Constants for the Density Correlations of Pure Species in Liquid Phase

Species	C_1	C_2	C_3	C_4
Ethanol	1.6288	0.27468	514	0.23178
Heptane	0.61259	0.26211	540.2	0.28141
Hexane	0.70824	0.26411	507.6	0.27537
Isopropanol	1.1799	0.2644	508.3	0.24653
Water	-13.851	0.64038	-0.00191	1.8211×10^{-6}

Table E.3: Constants for the Correlation for Specific Heat Capacities of Pure Species in Liquid Phase

Species	C_1	C_2	C_3	C_4	C_5
Ethanol	102640	-139.63	-0.030341	0.0020386	0
Heptane	61.26	314410	1824.6	-2547.9	0
Hexane	172120	-183.78	0.88734	0	0
Isopropanol	471710	-4172.1	14.745	-0.0144	0
Water	276370	-2090.1	8.125	-0.014116	9.3701×10^{-6}

$$c_p = C_1 + C_2T + C_3T^2 + C_4T^3 + C_5T^4 \tag{E.4}$$

The following equation was used to estimate the heat capacity of heptane:

$$c_p = \frac{C_1^2}{t} + C_2 - 2C_1C_3t - C_1C_4t^2 - \frac{C_3^2t^3}{3} - \frac{C_3C_4t^4}{2} - \frac{C_4^2t^5}{5} \tag{E.5}$$

where $t = 1 - T_r$, c_p is in $\mathrm{J\,kmol^{-1}\,K^{-1}}$ and T is in K. Constants were taken from Perry's Chemical Engineers' Handbook (Green & Perry, 2007) and are summarized in Table E.3.

Latent heats of vaporization were calculated using the following equation:

$$\Delta H_v = C_1(1 - T_r)^{C_2 + C_3T_r + C_4T_r^2} \tag{E.6}$$

$$T_r = T/T_c \tag{E.7}$$

where ΔH_v is in $\mathrm{J\,kmol^{-1}}$, T is temperature in K, and T_c is the critical temperature of the pure substance. Constants were taken from Perry's Chemical Engineers' Handbook (Green & Perry, 2007) and are summarized in Table E.4.

Gas heat capacities were calculated from the following equation:

Table E.4: Constants for the Correlation of Latent Heat of Vaporization for Pure Species in Liquid Phase

Species	$C_1 \times 10^{-7}$	C_2	C_3	C_4
Ethanol	5.5789	0.31245	0	0
Heptane	5.001	0.38795	0	0
Hexane	4.4544	0.39002	0	0
Isopropanol	7.2542	0.79137	-0.66092	0.34223
Water	5.2053	0.3199	-0.212	0.25795

Table E.5: Constants for the Correlation of Specific Heat Capacities for Pure Species in Vapour Phase

Species	C_1	C_2	C_3	$C_4 \times 10^{-6}$	$C_5 \times 10^{-9}$	$C_6 \times 10^{-12}$	$C_7 \times 10^{-16}$
Air	28.9422	0.0038	-2.9924×10^{-5}	0.0920	-11.9935	0.0056	-0.0644
Carbon Dioxide	23.5061	0.0381	7.4023×10^{-5}	-0.2227	0.2344	-0.1146	0.2168
Ethanol	53.7770	-0.2073	0.001422	-2.6298	2.3965	-1.0891	1.9639
Hexane	86.8460	-0.2553	0.002612	-4.9851	4.6341	-2.1683	4.0724
Isopropanol	48.7561	-0.0961	0.0014	-2.8580	2.6889	-1.2410	2.2561
Nitrogen	28.7168	0.0073	-4.54759×10^{-5}	0.1164	-0.1225	0.0059	-0.1087
Oxygen	29.7902	-0.0095	2.85799×10^{-5}	0.0001	-56.6511	0.0043	0.1022
Water	33.1744	-0.0032	1.7436×10^{-5}	-5.9796×10^{-3}	0	0	0

$$c_p = C_1 + C_2T + C_3T^2 + C_4T^3 + C_5T^4 + C_6T^5 + C_7T^6 \tag{E.8}$$

where c_p is in $\mathrm{J\,mol^{-1}}$ and T is in K. Constants were taken from Yaws (2009) and are summarized in Table E.5. Constants for air were calculated by taking the molar average of the constants for oxygen and nitrogen.

Appendix F

Emissivity of Water and Carbon Dioxide Gas

The algorithm of Leckner (1972) was used to calculate the total emissivities of water and carbon dioxide gas in the global model:

$$\ln \varepsilon_0 = a_0 + \sum_{i=1}^{M} a_i \lambda^i \tag{F.1}$$

$$a_i = c_{0i} + \sum_{j=1}^{N} c_{ji} \tau^j \tag{F.2}$$

$$\lambda = \log_{10}(pL_m) \tag{F.3}$$

$$\tau = T/1000 \tag{F.4}$$

where ε_0 is the total emissivity at atmospheric pressure, p is the partial pressure of water or carbon dioxide gas (bar) present in the flame control volume, L_m is the mean beam length (cm), and T is the gas temperature (K). Partial pressures were calculated from the mass flow rates of products given in Eq. (4.28) as follows:

$$p_j = P \frac{\dot{m}_{products,j}/M_j}{\sum \dot{m}_{products,j}/M_j} \tag{F.5}$$

where P is atmospheric pressure (Pa), $\dot{m}_{products,j}$ is the production rate of species j ($\mathrm{kg\,s^{-1}}$), and M is molecular weight ($\mathrm{kg\,mol^{-1}}$). Coefficients used in Eq. (F.2) are listed in Tables F.1 and F.2.

Table F.1: Coefficients Used for Calculating Total Emissivity of Water, $T > 400$ K, $M = 2$, $N = 2$

i	c_{0i}	c_{1i}	c_{2i}
0	-2.2118	-1.1987	0.034496
1	0.85667	0.93048	-0.14391
2	-0.10838	-0.17156	0.045915

Table F.2: Coefficients Used for Calculating Total Emissivity of Carbon Dioxide, $T > 400$ K, $M = 3$, $N = 4$

i	c_{0i}	c_{1i}	c_{2i}	c_{3i}	c_{4i}
0	-3.9781	2.7353	-1.9882	0.31054	0.015719
1	1.9326	-3.5932	3.7247	-1.4535	0.20132
2	-0.35366	0.61766	-0.84207	0.39859	-0.063356
3	-0.080181	0.31466	-0.19973	0.046532	-0.0033086

Appendix G

Air Entrainment Model Tuning for Global Model

The empirical constant in the air entrainment model in Eq. (4.26) was fit to burning rate models from Hamins et al. (1999) and Babrauskas (1983). Ambient temperature was held constant at 293.15 K. From Figure G.1 and Table G.1, it was found that an air entrainment equal to $1.55r$ gave satisfactory burning rate and flame temperature predictions over a range of pool diameters.

Flame temperatures in actual pool fires vary with height and radius. In the global model, the flame is treated as homogeneous and isothermal, so a realistic comparison between the prediction and experimental data is not possible.

Table G.1: Flame Temperatures (K) at Various Air Entrainment Rates Predicted with the Global Model

Species	$\dot{m}_a = 1.50r$	$\dot{m}_a = 1.55r$	$\dot{m}_a = 1.60r$	Experiment
Ethanol	1340	1315	1291	1490 (Babrauskas, 1983)
Hexane	1258	1233	1209	1300 (Babrauskas, 1983)
Heptane	1331	1305	1280	1200-1300 (Hiroshi & Taro, 1988)

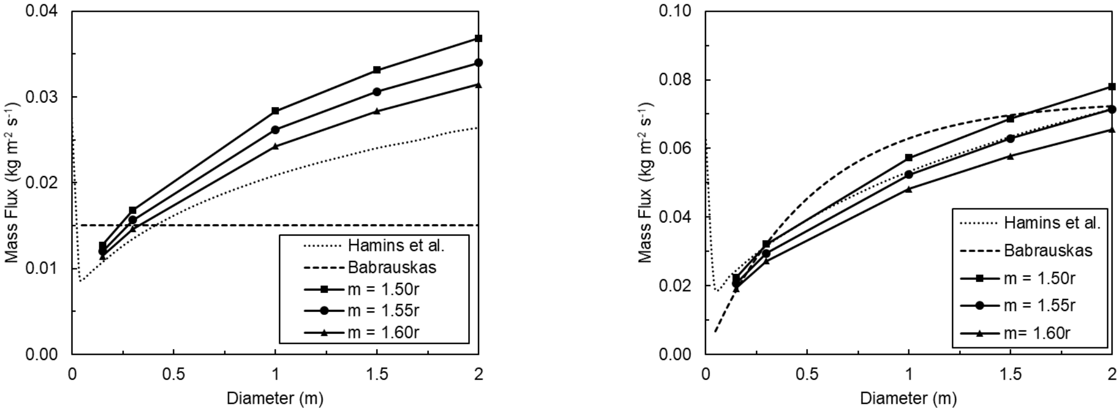

(a) Ethanol

(b) Hexane

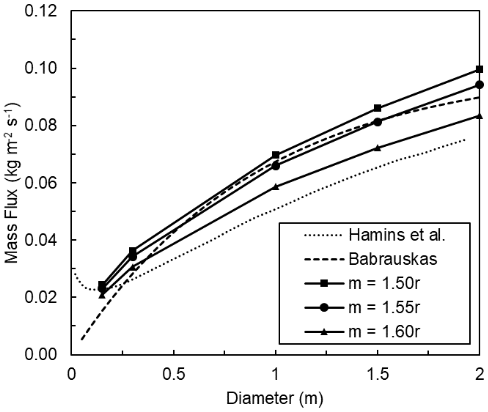

(c) Heptane

Figure G.1: Predicted mass flux at several pool diameters using the global model.

Appendix H

Heskestad's Flame Height Correlation

The data (Blinov & Khudyakov, 1957; Hägglund & Persson, 1976; Vienneau, 1964; Wood, Blackshear JR, & Eckert, 1971; Zukoski, Kubota, & Cetegen, 1981) used to fit Heskestad's original flame height correlation (Heskestad, 1983) was replotted against the dimensionless heat release rate (HRR), $\dot{Q}^*$. The data was originally plotted against a dimensionless parameter N, which is given as follows:

$$N = \left[\frac{c_{p\infty} T_\infty}{g\rho_\infty (\Delta H_c/r)^3}\right]\frac{\dot{Q}^2}{D^2} \tag{H.1}$$

where $c_{p\infty}$ is the specific heat capacity ($\mathrm{J\,kg^{-1}\,K^{-1}}$) at ambient temperature T_∞ (K), g is gravitational acceleration ($\mathrm{m\,s^{-2}}$), ΔH_c is the heat of combustion of the fuel ($\mathrm{J\,kg^{-1}}$), r is the stoichiometric air-to-fuel mass ratio, $\dot{Q}$ is the maximum HRR ($\mathrm{J\,kg^{-1}}$), and D is the diameter of the heat source (m). N was converted to $\dot{Q}^*$ using the following relationship (Alston & Dembsey, 2003):

$$N = \left[\frac{c_{p\infty} T_\infty}{(\Delta H_c/r)^3}\right]\dot{Q}^{*2} \tag{H.2}$$

Heskestad's flame height correlation in the form given by McCaffrey (1995) is given by the following equation:

$$\frac{H}{D} = -1.02 + 3.7\dot{Q}^{*2/5} \tag{2.10}$$

where H is the mean flame height (m). The results are plotted alongside Eq. (2.10) in Figure H.1. The R^2 value of Eq. (2.10) was 0.91.

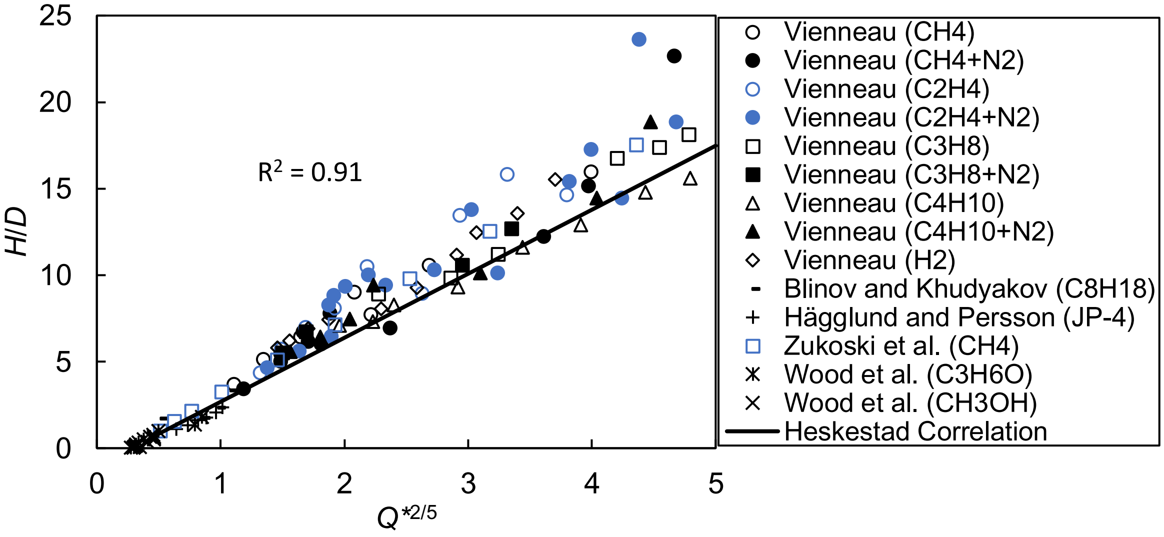

Figure H.1: Data used to fit Heskestad's original flame height correlation plotted against $\dot{Q}^{*2/5}$.